

**Effect of Electron Bombardment on the Size Distribution of Negatively Charged
Droplets Produced by Electrospray**

by

Xiaochuan (Lydia) Shi

A Dissertation

Submitted to the Faculty

of the

WORCESTER POLYTECHNIC INSTITUTE

In partial fulfillment of the requirements for the

Degree of Doctor of Philosophy

in

Mechanical Engineering

by

December 2011

APPROVED:

Dr. John Blandino, Advisor

Dr. Mark Richman, Committee Member

Mr. Tom Roy, Committee Member

Dr. Simon Evans, Committee Member

Dr. Cosme Furlong, Graduate Committee Representative

ABSTRACT

This study explores an innovative approach to control the droplet size distribution produced by an electrospray with the intention of eventually being able to deliver precisely controlled quantities of precursor materials for nanofabrication. The technique uses a thermionic cathode to charge the droplets in excess of the Rayleigh limit, leading to droplet breakup or fission. The objective of these experiments was to assess whether the proposed technique could be used to produce a new droplet size distribution with a smaller mean droplet diameter without excessively broadening the distribution.

An electrospray was produced in a vacuum chamber using a dilute mixture of ionic liquid. During their transit from the capillary source to a diagnostic instrument, the resulting droplets were exposed to an electron stream with controlled flux and kinetic energy. The droplets were sampled in an inductive charge detector to characterize changes in the size distribution. A positively biased anode electrode was used to collect electron current during droplet exposure. This collected current was used as the primary control variable and used as a measure of the electron flux. The anode bias voltage was a secondary control variable and used as a measure of the electron energy.

In a series of seven tests, two sets showed evidence of fission having occurred resulting in the formation of two droplet populations after electron bombardment. Three sets of results showed evidence of a single droplet population after electron bombardment, but shifted to a smaller mean diameter, and one set of results was inconclusive. Because of the large standard deviation in the droplet diameter distributions, the two cases in

which a second population was evident were the strongest indication that droplet fission had occurred.

ACKNOWLEDGEMENTS

I would like to express my sincerest gratitude to my advisor Professor John Blandino for his guidance, support, and encouragement during my PhD studies. Since the first day he led me into the “droplet fission” world with all his patience and encouragement, I have learned from him an attitude that is practical, rigorous, insistent and respectful as a great researcher and scientist. I will keep treasuring that attitude in the future and become a researcher like him.

I would like to thank Professor Mark Richman, Mr. Tom Roy, Professor Simon Evans and Professor Cosme Furlong for serving on my dissertation committee. I am very appreciative for the valuable time and advice they offered.

Special thanks to Mr. Sia Najafi for his continuous support and encouragement during the years and also to Professor Gretar Tryggvason for his support and guidance during my first few years at WPI, although he has now moved on to University of Notre Dame.

I am also very thankful to Barbara Edilberti, Barbara Furhman, Pam St. Louis, Adriana Hera and Randy Robinson for their generous help and their support as always.

This dissertation is dedicated to my parents and my sister. They are always there supporting me, full of love, no matter what decision I’ve made and what situation I’ve been in. Without their understanding and support, I would not have made it.

Many thanks to my friends at WPI and also to those back in China for their support at all time.

Contents

List of Figures	viii
List of Tables	xiii
Nomenclature	xiv
Executive Summary	xviii
Chapter	
1 Background and Motivation	1
1.1 Introduction	1
1.2 Use of Droplets for Nanomanufacturing	3
1.3 Electrospray	4
1.4 Droplet Fission	7
1.5 Inductive Charge Detectors	9
2 Model for Droplet Charging and Breakup	27
2.1 Introduction	27
2.2 Electron Flux	27
2.3 Droplet Charging and Breakup	35
2.4 Results from Simple Charging Model Analysis	42
3 Experimental Setup and Methodology	46
3.1 Introduction	46
3.2 Vacuum Chamber and Electrospray Source	47
3.3 Charge Detection Mass Spectrometer (CDMS)	52

3.3.1	Introduction	52
3.3.2	Model Used for Inductive Charge Detector Design	52
3.3.3	Mechanical Construction	62
3.3.4	Amplifier and Data Acquisition	64
3.3.5	Retarding Potential Measurement Methodology	66
3.4	Droplet Charging Apparatus	74
4	Results	76
4.1	Introduction	76
4.2	Results	81
4.3	Discussion of results	111
4.4	Measurement Sensitivity and Uncertainty Analysis	119
5	Conclusions and Recommendations for Future Work	129
5.1	Conclusions	129
5.2	Recommendation for Future Work	131
	Appendices	110
A.1	Operating and Calibrating Procedures for TCAC Control	133
A.2	Operating Procedure for CDMS Capture	137
B.1	MATLAB Code for Droplet Charge, Specific Charge and Size Analysis	140
B.2	MATLAB Code for Accelerating Potential Determination	146
C.1	Uncertainties of droplet specific charge measurements	156
C.2	Uncertainties of droplet charge measurements	157
C.3	Uncertainties of droplet size measurements	159

References Cited	160
Bibliography	165

List of Figures

1.1	Conceptual diagram of droplet fission setup	2
1.2	Diagram of colloidal electrospray source	5
1.3	Shelton's single sensing tube detector [Ref. 16]	10
1.4	Shelton's charge-velocity-position detector [Ref. 16]	10
1.5	Experimental setup used by Shelton to accelerate iron powder particles [Ref. 16]	12
1.6	Schematic of experimental set up for Hendricks' tests [Ref. 18]	13
1.7	Schematic diagram of experimental setup used to generate and measure charge and velocity of liquid droplets in Hogan and Hendricks' tests [Ref. 19]	14
1.8	Schematic diagram of Faraday cage detector used to measure individual particle charge and velocity in Hogan & Hendricks tests [Ref. 19]	15
1.9	General scheme for producing and detecting electrostatically charged microparticles with high velocity in Keaton's tests [Ref. 20]	16
1.10	Experimental setup in Fuerstenau's test [Ref. 17]	17
1.11	Charge detector and amplifier set up in Fuerstenau's test [Ref. 17]	18
1.12	Electrospray source and vacuum facility in Gamero-Castaño's tests [Ref. 21]	21
1.13	Typical stopping potential curve for electrospray in Gamero-Castaño's tests [Ref. 21]	22
1.14	Schematic of capacitive detector used by Gamero-Castaño to measure charge and specific charge of electrospray droplets [Ref. 21]	23
1.15	ICD with multiple stages by Gamero-Castaño [Ref. 22]	24

1.16	Signal induced by a charged droplet passed through the multiple stage ICD detector in Gamero-Castaño's tests [Ref. 22]	25
2.1	Conceptual diagram for electron energy balance	29
2.2	Exposure length and residence time (to reach Rayleigh limit) as a function of droplet radius	35
2.3	Conceptual diagram of charging process with and without electron drift velocity	37
2.4	Conceptual diagram showing electrons collected by negatively charged droplet	38
2.5	Negatively charged droplet charges up with $V_{an}=1V$ (q vs. t)	42
2.6	Negatively charged droplet charges up with $V_{an}=1V$ (v_{min} vs. t)	43
2.7	Negatively charged droplet charges up with $V_{an}=20$ volts (q vs. t)	43
2.8	Negatively charged droplet charges up with $V_{an}=20$ volts (v_{min} vs. t)	44
3.1	Facility used for electrospray including the vacuum chamber, Pyrex bottle containing fluid and digital camera to monitor the Taylor cone and jet	47
3.2	Interface of TCAC vi for Spellman & Glassman power supplies	50
3.3	Photograph of electrospray operating at $V_n=1688$ V, $I_n=52$ nA and $P_c = 7.1 \times 10^{-5}$ Torr	51
3.4	Schematic of the induced charge sensor	53
3.5	Schematic of droplet location in the sensor tube	54
3.6	Induced charge and current for droplet travelling parallel to the tube axis, with an (trajectory) axis ratio of 0.99, 0.8, 0.6 and 0	56
3.7	Induced charge and current for droplets travelling un-parallel to the axis of tube, droplet enters with $\frac{r_0}{a} = -1$ and exits with $\frac{r_0}{a} = +1$	57

3.8	Effect of the measuring electronics on induced charge and current	60
3.9	Cutaway drawing showing CDMS mechanical layout	63
3.10	Simplified schematic of amplifier circuit [Ref. 32]	65
3.11	Interface of CDMS vi	65
3.12	Diagram of induced voltage trace on the sensor tube indicating the time-of-flight (TOF) as the distance between pulse peaks	67
3.13	Acceleration Potential Mechanism Scheme	68
3.14	Stopping (retarding) potential curve	70
3.15	Diagram of thermionic cathode with accelerating anode plate	74
3.16	CAD drawing of CDMS/Thermionic cathode with anode plate	75
3.17	Picture of CDMS/Thermionic cathode without anode plate	75
4.1	Measured anode current I_{an} as a function of anode voltage V_{an} , with no electrospray	78
4.2	Typical wave captured by CDMS	82
4.3	Criterion for Preliminary selection of “good” waves	83
4.4	Typical baseline Droplet Stopping potential curve with a sweep range of 0 to -2000 V, with $\Delta V = -100$ V, $\Delta t = 30$ sec	84
4.5	Baseline Droplet Stopping potential curve with a sweep range of -400~ -2000 V, $\Delta V = -50$ V, $\Delta t = 600$ S	85
4.6	Typical waves captured by CDMS, with droplets subjected to electron flux	86
4.7	Typical stopping potential for droplets subjected to electron flux, with a sweep range of 0 to -2800 V, with $\Delta V = -100$ V, $\Delta t = 90$ sec. (Test 1 of Case 4)	87
4.8	Results of Case 1, Test 1 (Charge)	88

4.9	Results of Case 1, Test 1 (Time-of-flight, specific charge, size)	89
4.10	Baseline stopping potential curve for Case 1(Test 1), $V_{acc} = -1300$ V	90
4.11	Results of Case 2, Test 1 (Charge, time-of-flight)	92
4.12	Results of Case 2, Test 1 (Specific charge, size)	93
4.13	Baseline Stopping potential curve for Case 2 (Test 1), $V_{acc} = -1700$ V	94
4.14	Stopping potential curve with “Cathode on” for Case 2 (Test 1) of (0 ~ -2500V), $V_{acc\ 1} = -400$ V; $V_{acc\ 2} = -1850$ V	95
4.15	Results of Case 2, Test 2 (Charge, time-of-flight, specific charge)	96
4.16	Results of Case 2, Test 2 (Size)	97
4.17	Baseline Stopping potential curve for Case 2 (Test 2), $V_{acc} = -1820$ V	97
4.18	Stopping potential curve with “Cathode on” for Case 2 (Test 2) of (0 to -2800V), $V_{acc\ 1} = -500$ V; $V_{acc\ 2} = -2000$ V	98
4.19	Results of Case 2, Test 3 (Charge, time-of-flight, specific charge)	99
4.20	Results of Case 2, Test 3 (Size)	100
4.21	Baseline Stopping potential curve for Case 2 (Test 3), $V_{acc} = -1622$ V	100
4.22	Stopping potential curve with “Cathode on” for Case 2 (Test 3) of (0 to -2800V), $V_{acc\ 1} = -450$ V; $V_{acc\ 2} = -1900$ V	101
4.23	Results of Case 3, Test 1 (Charge, time-of-flight, specific charge)	102
4.24	Results of Case 3, Test 1 (Size)	103
4.25	Baseline Stopping potential curve for Case 3 (Test 1), $V_{acc} = -1723$ V	103
4.26	Stopping potential curve with “Cathode on” for Case 3 (Test 1) of (0 to -2800V), $V_{acc1} = -450$ V; $V_{acc2} = -2100$ V	104

4.27	Results of Case 4, Test 1 (Charge, time-of-flight and specific charge)	105
4.28	Results of Case 4, Test 1 (Size)	106
4.29	Baseline Stopping potential curve for Case 4 (Test 1), $V_{acc} = -1700$ V	106
4.30	Stopping potential curve with “Cathode on” for Case 4 (Test 1) of (0 to -2800V), $V_{acc1} = -500$ V; $V_{acc2} = -2050$ V	107
4.31	Droplet wave peak V_{peak} vs. droplet charge q for each half wave	108
4.32	Results of Case 5 (Test 1)	109
4.33	Time-of-flight vs. droplet charge for “Cathode on” cases, Case 2	112
4.34	Small drops observed accidentally	116
4.35	Droplet diameter changes before and after electron bombardment for all test cases (Test 1 of Case 5 not included)	117
4.36	Determination of U_{V_1} and \bar{V}_p	124
4.37	Determination of $U_{V_{acc}}$	126
A.1	Front panel of TCAC control	133
A.2	Control panel of CDMS	137

List of Tables

2.1	Parameters used in droplet charging model	41
4.1	Test cases for droplet fission tests	79
4.2	Fixed test parameters	80
4.3	Test Results – Droplet Size Before & After Electron Bombardment	81
4.4	Summary of Test Results for Charge, Specific Charge, TOF, V_{acc} and Diameter Before and After Electron Bombardment	110
4.5	Errors for droplet charge, specific charge and diameter	127
C.1	Uncertainties of droplet specific charge measurements	156
C.2	Uncertainties of droplet charge measurements	157
C.3	Uncertainties of droplet size measurements	159

Nomenclature

a	Radius of sensor tube
A	Combination of physical constants used in emission current density calculation
A_d	Cross sectional area of droplet (frontal area)
A_f	Surface area of filament
A_s	Area of anode plate
σ	Standard deviation of distribution
ϕ	Electronic work function
ϕ_d	Potential difference of droplet and electron
$\phi(y)_e$	Local potential relative to filament
λ_{De}	Debye length
λ_{res}	Residence time required for droplet to reach Rayleigh limit
c	Half length of sensor tube
C	Equivalent capacitor in CDMS circuit
C_d	Capacitance of droplet in electrons
d	Droplet diameter
D_d	Diameter of droplet produced by electrospray
ε	Fluid permittivity
ε_0	Vacuum permittivity
$-e$	Electron
erf	Error function
E_{mech}	Mechanical energy of an electron

$E_{thermal}$	Thermal energy of electron
E_{total}	Total energy for a collisionless electron
$f(x, \bar{v}, t)$	Velocity distribution of electrons
$f(v_e)$	Electron Drifting Maxwellian distribution of electrons
G	Gain of CDMS
H	Distance between filament and anode plate
I	Current of electrospray
I_{an}	Electron current collected on the anode plate
I_e	Electron current
I_n	Needle current
J_0	0 th order Bessel function
J_1	1 st order Bessel function
J_e	Electron current density
$J_{e_{anode}}$	Current density of electrons at location of anode plate
k_B	Boltzmann constant
K	Fluid conductivity
L	Length of CDMS sensor tube
L_{fil}	Filament (droplet exposure) length
m_d	Mass of droplet
m_e	Mass of electron
n_e	Number density of electrons
$n_{e_{anode}}$	Number density of electrons at location of anode plate

ρ	Fluid density
P_c	Chamber pressure
q	Droplet charge
q'	Induced charge on sensing tube
q_c	Charge on the equivalent capacitor of CDMS
q_0	Initial charge of droplet
$\frac{q}{m}$	Droplet specific charge
Q	Fluid flow rate
$Q_{rayleigh}$	Rayleigh limit charge of droplet
γ	Surface tension of fluid
r	Reflection coefficient for thermionic emission
r_d	Droplet radius
r_0	Droplet's radial location inside sensor tube
R_1	Sensing resistor in CDMS circuit
τ	Droplet time-of-flight
τ_e	Electrical relaxation time
T_e	Temperature of electron
U	Uncertainty
v_d	Drift velocity of electrons
v_e	Velocity of electrons
v_{min}	Minimum velocity required for electron to overcome potential barrier of droplet
V_{acc}	Droplet accelerating potential

V_{an}	Potential applied to anode plate
V_{max}	Positive peak of droplet induced voltage trace
V_{min}	Negative peak of droplet induced voltage trace
V_n	Needle voltage
V_{trig}	Potential of trigger level of oscilloscope
\bar{V}_p	Average of two peaks in droplet induced voltage trace
V_H	Potential applied to filament
$V_1(t)$	Droplet induced voltage trace
ΔV_L	Droplet irreversible potential loss in the process of jet formation prior to breakup
x_n	n th zero of 0 th order Bessel function J_0
z_0	Droplet's axial location inside sensor tube
$\langle \rangle$	Mean value

Executive Summary

Electrospray is a technique capable of producing nearly monodisperse jets of micron and sub-micron diameter droplets. These droplets have found wide-ranging applications in mass spectroscopy of biological molecules, material coatings, spacecraft propulsion, fuel and chemical delivery as well as material processing. A promising application is the use of micron-sized droplets to deliver controlled amounts of precursor materials to a substrate in the form of a solute dissolved in the droplets. If the size distribution of these droplets can be controlled, so can the mass distribution of the precursor material delivered to the substrate. This capability results in numerous potential applications in nanofabrication.

One technique of controlling the droplet size distribution involves controlling the breakup of the droplets. The goal of the controlled breakup is to create a smaller mean droplet diameter. This technique is accomplished with the use of electron bombardment, which induces droplet breakup or fission. This fission occurs as a result of the negatively charged droplet collecting sufficient charge from exposure to an electron source until its charges exceed the droplet's Rayleigh limit. This limit establishes the limiting, stable ratio of charge-to-mass for which the droplet's surface tension forces balance the repulsive electrostatic force.

This dissertation presents the results of a study into the use of electron bombardment as a means of inducing droplet breakup and thereby shifting the size distribution to a smaller mean value as would be desirable for nanofabrication. To accomplish this objective, an experiment was designed in which an electrospray was

produced and the resulting droplets exposed to an electron flux until charged beyond the Rayleigh limit. An instrument was built to measure the charge, specific charge, and droplet diameter distributions both with and without electron bombardment.

The fluid used was a mixture of an ionic liquid “EMI-Im” (1-ethyl-3-methylimidazolium bis(trifluoromethylsulfonyl) imide) in tributyl phosphate (TBP). EMI-Im has been used in electric propulsion because of its very low evaporation rate in vacuum. Electrosprays generated with mixtures of EMI-Im and TBP have been investigated and reported in the literature. A metallic capillary used to generate the electrospray was biased negatively in order to produce negatively charged droplets. These droplets form a spray (or plume) which is directed through a stream of electrons produced by a thermionic cathode and accelerated by an anode plate. The electrons incident on the negatively charged droplets increase the droplet’s electric charge beyond the Rayleigh stability limit resulting in fission. Droplets in the plume, with and without exposure to the electron source, were sampled by a Charge Detection Mass Spectrometer (CDMS). The CDMS, which was designed on the basis of inductive charge detector theory, was used to measure the charge, time-of-flight and specific charge of the droplet. These data, along with an independent measurement of the droplet mean energy, provided enough information to calculate the droplet size distributions before and after electron bombardment and to determine the impact of the electron bombardment to droplet size distribution.

A simplified charging model was used to guide cathode construction. The length of the cathode, for example, determines the electron exposure (residence) time for a given droplet velocity. This charging model allows one to estimate whether the electron flux

and energy are sufficient to charge the droplets to the Rayleigh limit for a given initial droplet charge, droplet velocity, and set of cathode design and operating conditions. This model is also used as a guide in the selection of cathode operating conditions such as filament heater current and anode voltage. Increasing the electron flux reaching the droplets increases the rate of charging and hence results in a droplet reaching the Rayleigh limit in a shorter period of time. The results from this simple model show that the experimental setup used for droplet electron bombardment was sufficient to reach the Rayleigh limit.

A charge detection mass spectrometer (CDMS) was designed and built to measure the droplet charge, velocity (time-of-flight), and specific charge. The smallest charge the CDMS can measure is 52,990 electron charges (4.1×10^{-15} C). This limit was due mainly to electrical background noise in the detector signal. The CDMS is an inductive charge detector based on a design that has been used by other researchers. In this class of charge detector, a charged particle is allowed to pass through a sensing tube connected to ground through a high impedance amplifier. The induced charge creates a voltage pulse on the sensor tube which can be amplified. The resulting signal, which is a voltage waveform created by the droplet passing through the sensor tube, is used to calculate the droplet charge. An analytical estimate of the induced charge on the sensor tube as a function of time was made using an electrostatics model. These calculations were used to check the sizing of the sensor tube to confirm that the length-to-diameter (aspect) ratio was sufficient to produce an image charge nearly equal to the actual droplet charge. In addition, using this model in conjunction with a simple RC circuit model allowed us to quantify the error induced by the amplifier circuit on the collected signal.

The analysis showed that the reduction in pulse height and the peak shift caused by RC decay were insignificant. The RC effect on the calculations of charge and time-of-flight were also insignificant.

Calculation of the droplet diameter using the charge, velocity (time-of-flight), and specific charge data collected by the CDMS requires independent measurement of the droplet kinetic energy, or “accelerating potential.” A retarding potential measurement methodology is used to measure this energy so that the diameter can be calculated. The accelerating potential is a potential to which a retarding electrode or screen, located at the entry of the CDMS, must be decreased relative to the ground to repel the negatively charged droplets such that the droplet velocity reaches zero at the surface of the retarding screen. For droplets with different sizes (different populations), there will be distinct values of the accelerating potential, each with a characteristic spread or variation. This spread is a result of the droplets having a variation in energy carried from their point of origin in the electrospray. By sweeping the retarding voltage from zero to more negative values, a larger fraction of the droplets in the plume will be repelled by the negatively biased screening electrode, and fewer droplets will be able to enter into the detector tube. The number of the droplets passing through the detector is counted and used to calculate a collection frequency. Droplet counting is a more sensitive alternative to measuring the current directly using an electrometer, as the current becomes undetectable all but the most energetic droplets are repelled. Eventually all the droplets are stopped at the retarding screen. The specific accelerating potentials can then be determined for different sized droplets from the retarding-potential versus droplet frequency curve.

The electron flux was selected as the primary independent variable for evaluation of the effectiveness of the proposed method to break up the droplets by electron bombardment. Seven tests were conducted to investigate the effect of electron flux on the droplet size distribution. The current collected on the anode (electron collection electrode) was used as the measure of the electron flux for each test. Each of these seven tests consists of a set of data collected with and without the electron source turned on.

Of these seven test sets, two showed evidence of the formation of a second, smaller mean diameter droplet population with narrow distribution after electron bombardment as evidenced by the distribution data collected by the CDMS. The mean diameter of second droplet population for one test is $1.8 \mu m$ with standard deviation of $0.7 \mu m$ compared with the original mean diameter of $9.3 \mu m$ with standard deviation of $2.5 \mu m$. Another test shows a $1.4 \mu m$ mean diameter of second population with standard deviations of $0.6 \mu m$ compared with the original mean diameters of $8.3 \mu m$ with standard deviation of $2.2 \mu m$. Four tests showed a possible reduction in the mean diameter of droplets subject to electron bombardment (though still within one standard deviation). In addition to a reduction in the mean diameter of the distributions, these four tests also resulted in a narrower distribution (smaller standard deviation) after electron bombardment. The standard deviations of these four after electron bombardment tests are $0.7 \mu m$, $1.6 \mu m$, $1.86 \mu m$ and $1.6 \mu m$ compared with the standard deviations of original base tests of $1.2 \mu m$, $1.7 \mu m$, $1.9 \mu m$ and $2.1 \mu m$. For all seven test cases, the stopping potential curves with the cathode turned on showed some evidence of a second “step” indicative of a second population.

Some possible reasons why a smaller mean diameter population was not detectable by the CDMS for all seven cases are: 1) droplets (after fission) were below the resolution threshold of the CDMS, which is at the order of 10^{-15} C; 2) smaller, negatively charged droplets produced during breakup were deflected away from the CDMS entry port as a result of attraction by the positively biased anode plate and hence not captured by the detector.

As a result of these tests, it was concluded that the electron bombardment does have an impact on the size distribution of negatively charged droplets.

Chapter 1 Background and Motivation

1.1 Introduction

Electrically charged droplets produced by electrospray have been previously investigated as a potential supply of precursor materials for nanofabrication [Ref 1-4]. In this study, an innovative approach is investigated to control the size distribution of droplets produced with electrospray. The intended future application of this process is the ability to deliver precisely controlled quantities of precursor materials for nanofabrication. Our objective is to use the proposed technique to produce a new droplet size distribution with a smaller mean droplet diameter. The mechanism of droplet fission is used as a means of actively controlling the droplet size distribution. To enable this breakup or fission of droplets, an electrospray is used which generates negatively charged droplets. This electrospray forms a plume of droplets which is directed through a stream of electrons produced by a cathode. The electrons incident on the negatively charged droplets increase the droplet's electric charge beyond the Rayleigh stability limit resulting in fission. Droplet charge-to-mass ratio (specific charge) and charge are determined with a Charge Detection Mass Spectrometer (CDMS) sensor allowing a determination of droplet diameter for fluids of known density.

Figure 1.1 shows a schematic representation of an electrospray (micron to submicron droplets containing nanomaterial precursors) generated with a certain energy, represented by the accelerating potential voltage V_{acc} , and fluid flow rate Q . A cathode, used to generate electrons, is also represented which generates an emission current

density of J_e , and also shown is a diagnostic sensor (Charge Detection Mass Spectrometer or CDMS) used to measure droplet charge q , specific charge $\frac{q}{m}$ and size r_d .

To demonstrate the viability of this approach, experimental measurements were made of the droplet size distribution with and without exposure to electron bombardment. These measurements were supplemented by a simple charging model to help estimate required droplet residence times for electron exposure.

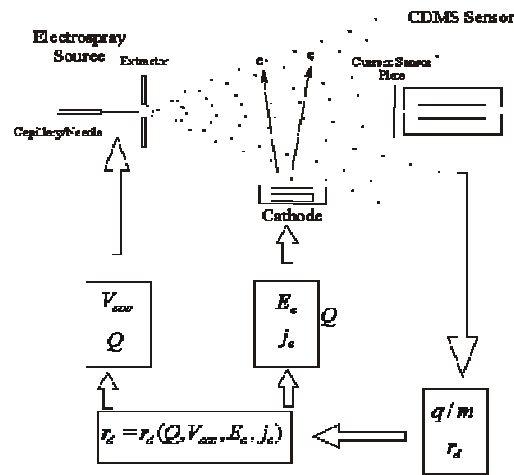


Figure 1.1 Conceptual diagram of droplet fission setup

This dissertation is organized as follows. In the following sections of Chapter 1, the application of droplets in nanomanufacturing will be reviewed, followed by an introduction and review of electrospays, droplet fission, and inductive charge detectors. In Chapter 2, a model for droplet charging and breakup is discussed. Chapter 3 describes the experimental setup including the vacuum system, electro spray source, charging apparatus and the charge detection mass spectrometer. Results and discussion for various

test cases and the uncertainty analysis are included in Chapter 4. Chapter 5 presents conclusions and recommendations for future work.

1.2 Use of Droplets for Nanomanufacturing

Electrosprays provide a means of delivering nearly monodisperse sprays of droplets which, for manufacturing applications, could contain precursor materials for subsequent incorporation into an assembled structure. In one technique, the precursor material is an involatile solute in a volatile solvent. The resulting mixture can be delivered to a target through electrospray after which the volatile solvent evaporates leaving a precursor residue [1]. In another technique, the electrospray plume contains a mixture of liquid precursors, which are injected through a reactor where the precursors form solid particulates [2]. The advantage of the electrospray source in these processes is its ability to deliver a nearly monodisperse jet of submicron droplets. In addition, since the droplets are electrically charged, the option exists to control the placement of the material through electrostatic “steering” of the droplets before delivery to the substrate. Such promising characteristics give electrosprays the potential for industrial application, not only in the nanomanufacturing field, but also in paint spraying, fuel injection, agricultural spray and even fire-fighting [3] and electric propulsion [4].

1.3 Electrospray

When a conducting liquid flowing through a capillary is subjected to an external electric field, the surface of the fluid at the open end of the capillary will be subjected to electrostatic, surface tension and hydrodynamic forces which affect the shape of the free surface. Different combinations of flow rate and applied potential will result in distinctly different regimes of operation. For a given flow rate, if the applied voltage is too low, the flow from the capillary will be dripping with a dripping frequency that increases with the increasing voltage. As the voltage is increased further, an unstable regime is encountered in which an alternating, round or cone shaped meniscus will be formed at the end of capillary. In this so-called pulsating mode [5], the liquid meniscus is unstable and switches shape between a round, hemispherical surface in which the liquid at the tip is accumulating, and a conical surface with a jet appearing at the apex. When the jet forms a small amount of fluid is ejected as droplets break off from this jet. The fluid then accumulates again forming the hemisphere and the process repeats. When applied voltage exceeds a certain value (typically a few kilovolts), a force balance is achieved and a stable cone is formed. A thin micro-jet is formed at the apex as in the pulsating mode, except that it is now stable. This jet (tens to hundreds of nanometers in diameter) eventually breaks up as a result of the Plateau-Rayleigh instability into individual droplets. This mode of operation is referred to as the cone-jet mode and such a source of droplets is commonly referred to as an electrospray.

Figure 1.2 shows the emission of electrospray from a capillary (needle), which is shown electrically biased with respect to a grounded extractor electrode. The potential

difference between the needle and the extractor establishes the required electric field to produce and accelerate the droplets away from the needle. A typical distance between the needle and extractor is usually several millimeters and the applied potential difference, which will be dependent on the fluid conductivity, is 1.5 – 2.5 kV (for the present experiment). Droplets emitted from the tip of Taylor cone are accelerated between the needle and an extractor.

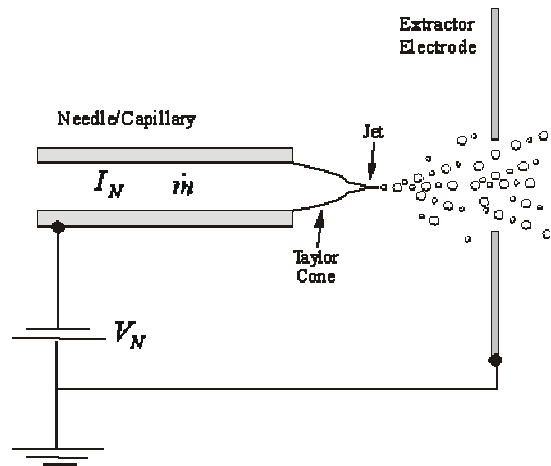


Figure 1.2 Diagram of colloidal electro spray source

The electro spray phenomenon was first reported by Zeleny between 1914 and 1917 [6] and explained by Taylor in 1964 [6]. Because of his pioneering work in this area, the conical meniscus which forms is now referred to as a “Taylor cone”. Taylor was able to predict the potential required for cone formation of water drops and the cone semi-angle which he found to be 49.3° , a value which doesn’t agree with experiments involving highly conducting fluids. De La Mora [7] developed a model, for fluids with high conductivity, which accounted for the space charge of droplets ejected from a cone-

jet. He broadened Taylor's theory to a more general version, in which a stable liquid cone and visible jet spray are formed with a cone semi-angle in the range of 32° - 46° .

It is a well-established feature of electrosprays that for a given liquid, formation of a stable Taylor cone and emission jet (so called cone-jet mode) can be established only over a restricted range of accelerating voltages and flow rates. From the well known scaling law of current with flow rate $I \sim Q^{1/2}$, current of electro spray is governed mostly by flow rate Q . For highly conducting fluid, the current scales as $I \sim (\gamma K Q / \epsilon)^{1/2}$ [8], where γ , K , ϵ are surface tension, liquid conductivity and permittivity, respectively. The current is nearly independent of applied needle voltage and electrode shape.

The size distribution of droplets produced by electro spray operating in different spraying modes was studied by Chen and his colleagues [5, 9]. It was found that the cone-jet mode resulted in a narrow size distribution with smaller droplet sizes compared with other operating modes. The droplet size scales as $D_d \sim (Q / K)^{1/3}$ in cone-jet mode. Chen and his group also confirmed that for low electrical conductivity liquids, the droplet size is mainly determined by liquid flow rate and secondarily by applied voltage [10]. Obtaining a narrow droplet size distribution with smaller droplet size requires a small flow rate and a high applied voltage while operating at cone-jet mode, which further restricts the range of flow rates and voltages over which one can operate. Increasing the voltage at a given flow rate beyond the values consistent with cone-jet mode operation results in a different spray regime characterized by multiple jet formation. This regime is sometimes referred to as the highly stressed regime. As a result, while electro sprays can produce a relatively monodisperse jet of precursor droplets for use in nanofabrication, the

voltage-flow rate space over which delivery of optimal size droplets can be delivered is limited.

1.4 Droplet Fission

Droplet breakup or fission has been extensively investigated and documented in the scientific literature since the Rayleigh criterion was first derived by Lord Rayleigh in 1882 to describe the instability of a charged droplet [12]. There is an upper limit to the charge-to-mass ratio which can be sustained by an electrospray droplet for any given fluid. The repulsive electrostatic force on a charged liquid droplet is counter-balanced by the cohesive surface tension force resulting in a maximum charge which can be sustained for a given droplet radius. This limit is the well-known Rayleigh stability criterion Eq. (1.2.1) which depends on the fluid through the surface tension coefficient. When charge on the droplet exceeds the Rayleigh limit, the repulsive electrostatic force overcomes the attractive surface tension force, the droplet becomes unstable and eventually breaks up.

$$q^2 = 8\pi^2 \epsilon_0 \gamma D_d^3 \quad (1.2.1)$$

In Eqn. (1.4.1), ϵ_0 is the permittivity of free space and γ is the surface tension of the droplet. The stability of a charged, evaporating droplet suspended in an electric field has been studied by previous investigators by measuring the droplet's charge and mass before and after disruption. It was first found by Doyle that the original or "mother" droplet loses about 30% of its charge after one or more highly charged small droplets are ejected [11]. Work by Abbas and Lathan revealed that the mass loss of a mother droplet

is about 25% of its original value [12]. For droplets with radius larger than 200 μm , the Rayleigh criterion is no longer valid because the spherical assumption is not necessarily satisfied for larger droplets. Since their measurements were limited to the droplets after break up, the results do not likely reflect the actual situation at break up. Studies by Schweizer and Hanson showed that a droplet, upon breakup, can lose up to 23% of its charge and 5% of its mass [13]. Those numbers were updated by Taflin and his coworkers to 1 - 2.3% for mass loss and 10 - 18% for charge loss by precisely measuring the droplet size and charge [14]. It is also found that droplet disruption starts when the charge level is between 70 - 80% of the predicted Rayleigh limit [14, 15]. In the work presented in this dissertation, the actively controlled use of droplet fission to effect changes in the electrospray droplet size distribution was attempted. As discussed in Section 1.1, the deliberate exposure of the droplet plume to electrons produced by a cathode should induce fission and enable the delivery of droplets with a smaller mean diameter than obtainable from the jet breakup alone. For a plume of droplets, there will be a subsequent broadening of the size distribution as the initial population of “mother” droplets loses mass in the formation of multiple “daughter” droplets. The small mass loss (1 - 2.3% of the original value) suggests that significant reductions in droplet size require multiple fission events. Subsequent fission events have the combined effect of decreasing the mean droplet diameter but also broadening the size distribution in the plume. For a given droplet exposure length, the number of fission events during a droplet’s transit can be increased by increasing the electron flux to the maximum value possible (this will be discussed in Section 3.4).

1.5 Inductive Charge Detectors

Inductive Charge Detectors (ICD) have been used for decades because of their relatively low cost, simple but mature design, and ease of data analysis. The ICD measures the charge and time-of-flight of charged particles or droplets. The specific charge and the size of the particle or droplet then can be determined if the accelerating potential and fluid properties of the drop are known or can be determined.

The earliest ICD design can be traced back to 1960, when Shelton and his collaborators [16] used a charge-velocity-position detector to measure the velocity, position and the charge of micron-sized spherical solid iron particles that were positively charged. A single sensing tube detector was designed by Shelton firstly, which is capable of measuring the velocity and charge of a particle as shown in Figure 1.3. An insulated drift tube was mounted coaxially within a grounded shielding tube with grids on each end. When a particle passes through the detector, a voltage will induce on the detector which is proportional to particle charge and inversely proportional to system capacity (see the output signal from detector at the top of Figure 1.3). The duration of this induced signal is equal to the time-of-flight of the particle.

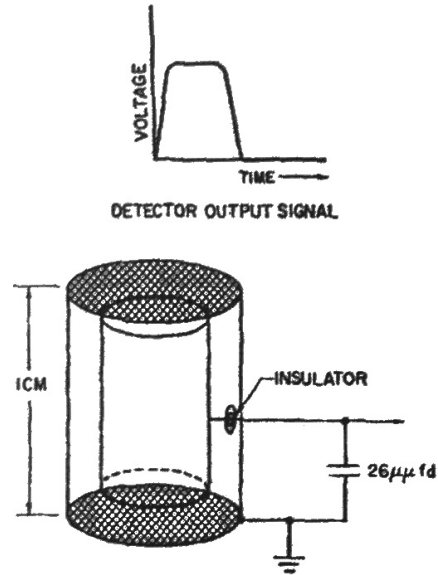


Figure 1.3 Shelton's single sensing tube detector [Ref. 16]

Since the single sending tube detector was only about 20% accurate, a detector with two sensing tubes capable of measuring both position and velocity was used in their test. Figure 1.4 shows the detector and an oscilloscope trace taken by this detector.

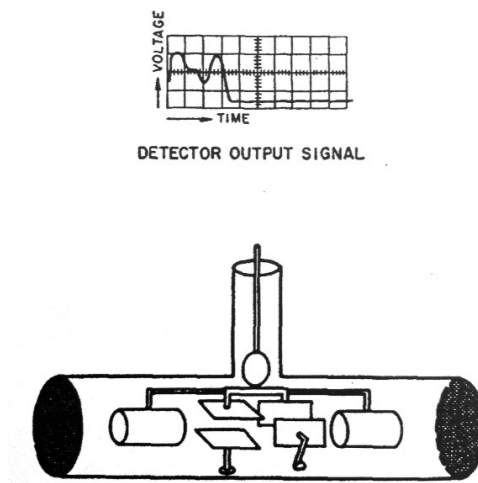


Figure 1.4 Shelton's charge-velocity-position detector [Ref. 16]

This detector had two insulated drift tubes mounted co-axially with a grounded, cylindrical shield. Two mutually orthogonal pairs of parallel plates were situated between tubes. The tubes and one of each pair of the parallel plates were connected together to the amplifier input while the other plates were connected to the shield. As the charged particle passed through the detector, it induced four pulses on the tube. The first and last pulses were the induced voltages generated by the charged droplet and were equal in amplitude. These two pulses were proportional to the charge on the particle and inversely proportional to the capacity of the system. The time measured from the beginning of the first pulse to the end of the last pulse was equal to the time-of-flight through the tube and used to calculate the velocity. The second and third pulses gave the position of the particle in the transverse, x and y directions.

In these tests, particles were charged by contact with a highly charged surface. As shown in Figure 1.5, iron powder was placed in a normally positively biased cup with a positively biased perforated cylindrical cover (both are at high potentials). The powder on the surface was injected by negative potential pulses applied to the cup. Injected powder would collide with a charging spherical tungsten electrode E , which was maintained at a high potential, and then charged and accelerated to enter a high accelerating field (accelerator) established by an external 100 KV dc source, where the detector and target were positioned. The charged particles were accelerated to pass through the detector and then impacted onto the target surface. All tests were conducted in a high vacuum environment. While Shelton does not report the resolution of his detector (in terms of the resolvable number of elementary charges), Fuerstenau and Benner [17] concluded it was few as 10^4 charges.

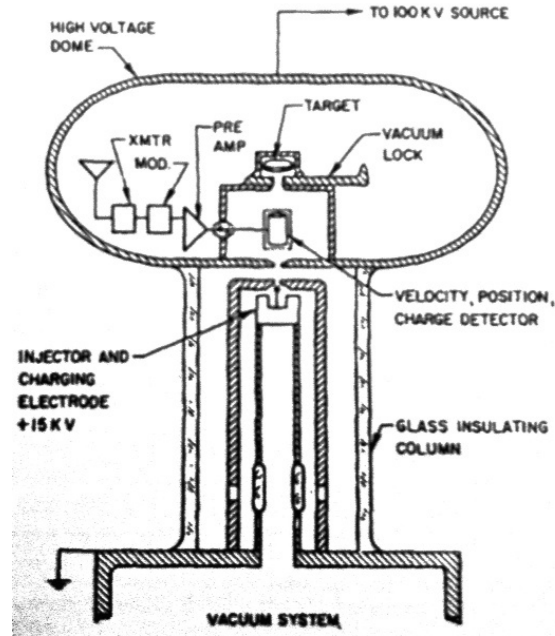


Figure 1.5 Experimental setup used by Shelton to accelerate iron powder particles [Ref. 16]

In 1962, Hendricks [18] applied Shelton's idea to measure the charge, the specific charge and the size of positively charged oil droplets produced by electrospray. The entire setup was in an evacuated bell jar and is shown in Figure 1.6 from Ref. [18]. The detector used a small flat plate, instead of a drift tube, which was mounted in a grounded cylindrical shield and connected to a high impedance voltage measurement circuit. The small hole in the detector plate was aligned with the holes in the detector shield and the needle tip, which allowed the charged droplet to pass through. As the charged droplet entered the shield and travelled toward the plate, the induced charge appeared on the plate and the voltage of plate began to rise, reaching a maximum when the droplet passed through the plate. The time measured from the point of zero volts to the peak of the voltage pulse corresponded to the time-of-flight of the droplet.

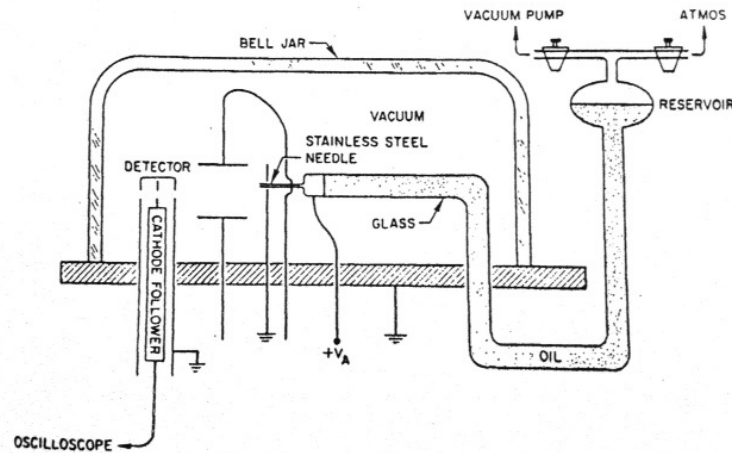


Figure 1.6 Schematic of experimental set up for Hendricks' tests [Ref. 18]

In Hendrick's work, the accelerating potential was defined as the voltage applied between the needle and the grounded copper plate, without any correction for irreversible losses in potential between the needle and the point of jet break up. The charge resolution of this detector was approximately 2×10^{-15} C (12,000 electron charges), primarily limited by the sweep triggering sensitivity of the oscilloscope and the overall system gain.

Later, Hogan and Hendricks [19] investigated the specific charge of droplets produced by the electrospray with a colloidal suspension in glycerin using a Faraday cage detector. The electrospray and a quadrupole mass spectrometer were placed in a high vacuum chamber as shown in Figure 1.7 (shown with a different detector). The Faraday cage detector is not shown in detail in Figure 1.8. The quadrupole mass spectrometer was used to separate the droplets according to their specific charge. The Faraday cage detector

was used in place of the detector shown in Figure 1.7 to measure charge and velocity of individual droplets resolved by the quadrupole mass spectrometer.

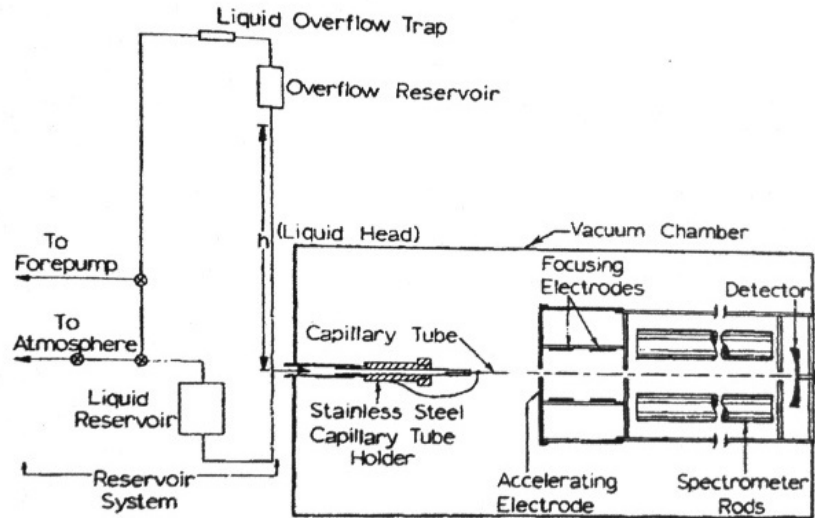


Figure 1.7 Schematic diagram of experimental setup used to generate and measure charge and velocity of liquid droplets in Hogan and Hendricks' tests [Ref. 19]

A small hole in the Faraday cage detector, visible in Figure 1.8 from Ref [19], allowed only a small fraction of droplets to pass into the Faraday cage so that the charge and the velocity of the single droplet would be measured. As the droplet passed through the detector, a voltage pulse was induced on the Faraday cage. The height of the pulse displayed on an oscilloscope was proportional to the charge on the droplet while the width indicated the time of flight. By knowing the length of the Faraday cage, the droplet velocity could be calculated. As done in Hendricks' previous tests, the potential difference applied between the capillary tube and the accelerating electrode was assumed to be equal to the accelerating potential. Since the tests were focused on determining the influence of some of the parameters, such as space charge and conductivity, on the

charge-to-mass ratio (specific charge) of the droplets, the resolution of the Faraday cage detector was not discussed.

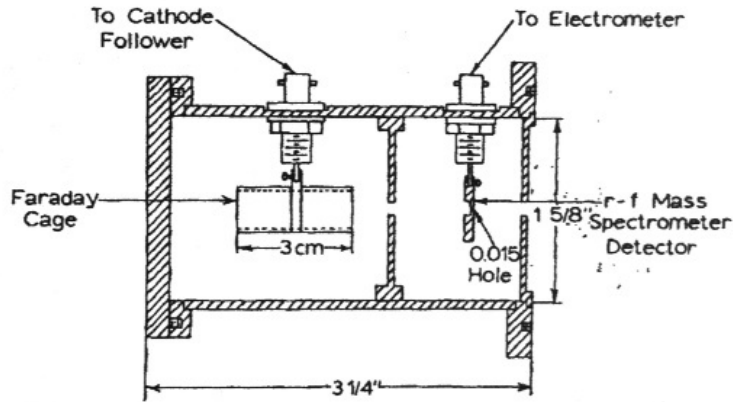


Figure 1.8 Schematic diagram of Faraday cage detector used to measure individual particle charge and velocity in Hogan & Hendricks tests [Ref. 19]

Keaton and his co-workers [20] developed a particle mass spectrometer in 1990 for their hypervelocity, microparticle, impact tests using solid particles. These tests were based on Shelton's work in 1960 [16] and also used solid, conductive particles, accelerated by contact with a high voltage surface. A series of cylindrical "charge pick off" detectors, shown in Figure 1.9 [20], were used to measure the charge and the time-of-flight of the particle. The charge of particle was measured after acceleration by the induced charge on the first cylindrical "pick-off" detector "P1". The velocity was determined by measuring the time-of-flight between two such pick-off detectors separated by a known distance. A pair of so called "selector plates" were used to allow the particles with only pre-determined masses and velocities to be collected on the target. By minimizing the noise level from the charge preamplifiers, which consisted of the preamplifier noise and also the noise introduced by the environment to the charge pick-

off cylinders, the detector was able to detect the particles with charge as small as 2,000 electron charges.

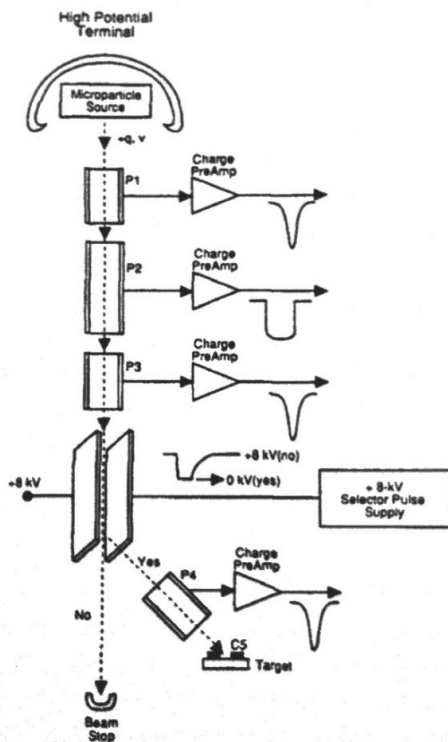


Figure 1.9 General scheme for producing and detecting electrostatically charged microparticles with high velocity in Keaton's tests [Ref. 20]

In order to determine the mass of multiply-charged DNA ions generated from macromolecules in the megaDalton size range, Fuerstenau and Benner [17] used a detector based on the Shelton single sensing tube design but improved the signal-to-noise ratio by differentiating the output from the sensor tube, a process referred to as the “pulse peaking-time filtering technique,” which greatly improved the charge detection resolution to 150 electron charges. The tests were performed in a vacuum environment with the experimental setup shown in Figure 1.10. The ions were generated by an electrospray

needle and accelerated by several lenses with different potential settings, then passed through two conical skimmers and a grounded inlet plate of the analyzer stage.

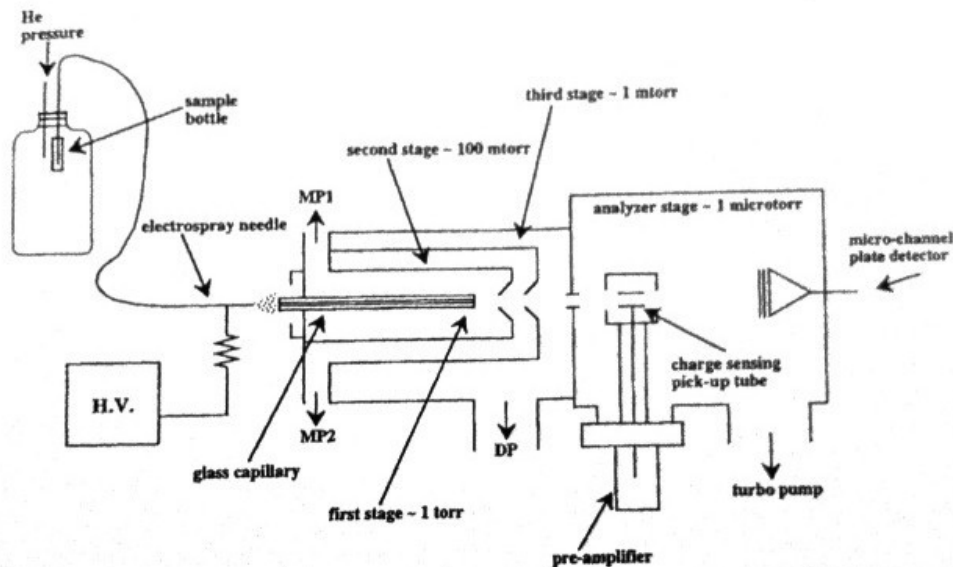


Figure 1.10 Experimental setup in Fuerstenau's test [Ref. 17]

Accelerated DNA ions were measured by the charge detector assembly at the analyzer stage, which was 11.9 cm away from the aligned needle. As shown in Figure 1.11, the charge detector assembly consisted of a 3.5 cm long thin wall brass charge pick-up tube with a 6.35 mm bore, which was supported with an insulator inside of a metal tube providing the electrical shield. As a DNA ion entered the tube, it induced an equal and opposite charge on the tube. The capacitance of the assembly was designed to be as low as possible in order to maximize the voltage presented by a small charge since $V = \frac{q}{C}$. The voltage output from a pre-amplifier was differentiated by a shaping amplifier so that the output signal is better shaped with a more accurate "entrance" and "exit" time points compare with the one without differentiation (see output signal of Shelton's single

sensing tube detector, Figure 1.3). The output shown on the oscilloscope was a double pulse signal whose first pulse corresponded to the charge induced on the tube as the ion entered it and the second pulse presented as ion exited the tube (see the voltage output signal at right upper corner of Figure 1.11). Time between two pulses was equal to the flight time required for the ion passing the tube, which allowed for more accurate determination of the time-of-flight and droplet charge than possible with the original version of Shelton's design.

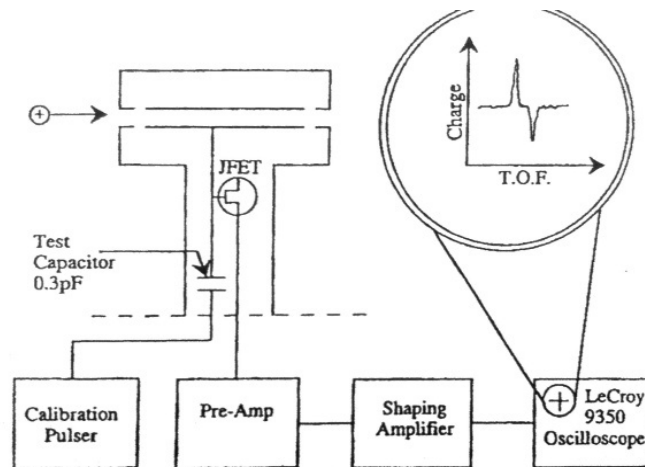


Figure 1.11 Charge detector and amplifier set up in Fuerstenau's test [Ref. 17]

In their paper, Fuerstenau and Benner [17] noted that the energy conservation equation used to determine the specific charge was not accurate because the initial electrostatic potential energy of the electrospray source was not fully converted to ion kinetic energy. A correction term $\frac{1}{2}mv_g^2$ was included to represent the missing part denoted as the initial kinetic energy imparted to the ion by free jet expansion of the gas before accelerated by the electric field, where v_g was defined as the velocity of ions due

to the gas expansion. Its magnitude was determined to be 10% of measured ion velocity with acceleration voltage set at 300 V .

A micro-channel plate detector (MCP) with a retarding potential grid positioned 40 cm behind the charge detection tube, as shown in Figure 1.10, was used by Fuerstenau and Benner to measure the ion energy distribution in the source beam before the acceleration. The retarding potential grid was used to electrostatically repel the DNA ions (particles) so that the arrival rate of particles to MCP detector could be determined as a function of retarding grid potential. These results showed that the kinetic energy of a DNA ion (particle) emerging from a jet in an axial electric field consisted of three components: the energy imparted to the particle, the kinetic energy associate with the drift of the particle relative to jet at the point where the particle's motion ceases to be controlled by gas collision and the particle's electrostatic potential energy at that point. This suggested that the particles were not accelerated with the same initial kinetic energy and the estimated correction term introduced an uncertainty to the particle specific charge results.

Prior to Fuerstenau and Benner' work, determination of the particle or droplet specific charge as reported in the literature assumed the accelerating voltage was equal to the applied electrostatic acceleration voltage. Fuerstenau and Benner's work in 1995 [17] took into account the energy imparted to the ions before acceleration. Unfortunately they did not report a way to measure an accurate value for the accelerating potential V_{acc} for the droplets or particles.

Gamero-Castaño [21] found that the droplets generated at the jet breakup have different acceleration voltages because of the irreversible losses in process of jet formation prior to breakup. These losses are termed “irreversible” because this voltage drop is mostly used to convert conduction current into convected surface charge, rather than to accelerate the fluid. In section 3.3.5, a detailed description of the stopping potential measurement technique will be introduced, which is used to determine the accelerating voltage (i.e. the initial energy of the droplets at the point of formation).

The charge, specific charge and stopping potential of the droplets generated by electrosprays of five tributyl phosphate (TBP) fluid mixtures with conductivities ranging at $10^{-2} - 10^{-4}$ S/m were measured in vacuum by Gamero-Castaño [21]. The schematic diagram of experimental setup is shown in Figure 1.12. Droplets were generated by a electrospray source with a fixed potential difference between the needle and extractor electrode of 1600 volts, while the potential of needle and extractor relative to the (electrical) ground, separately, were adjustable. Droplets passed through the small orifice of the extractor which was aligned with the needle tip and were collected by a grounded collector electrode. The collected current was measured by an electrometer.

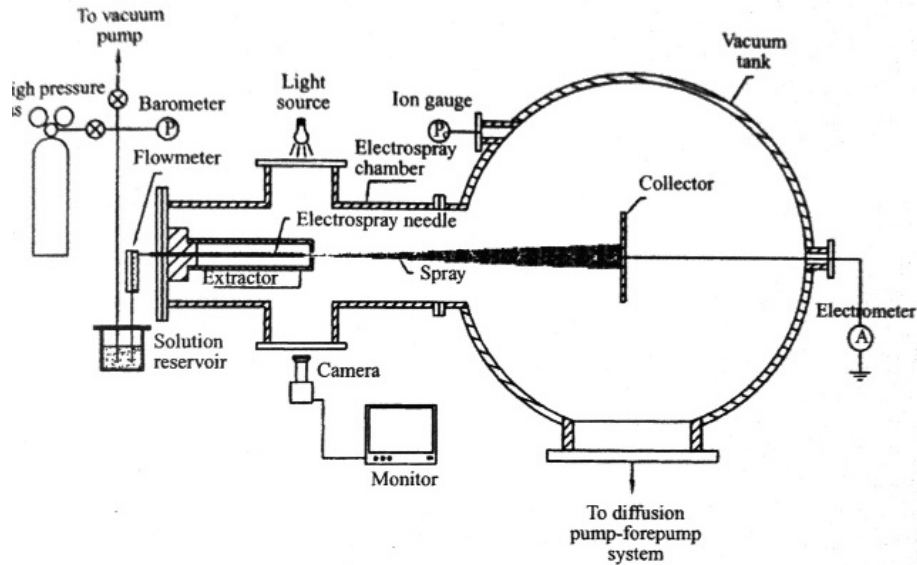


Figure 1.12 Electro spray source and vacuum facility in Gamero-Castaño's tests [Ref. 21]

When the needle voltage relative to ground was increased, the electric field for electro spray was kept constant by increasing the voltage of the extractor (relative to ground). The potential difference between the needle and ground was identified as the “needle voltage”, V_N . When V_N was well below ground there were no droplets able to reach the (grounded) collector and the current measured by electrometer was zero. The droplets were completely stopped at this needle voltage. A typical “stopping potential curve” is shown in Figure 1.13 generated by sweeping V_N from -400 V to 1600 V. Two steps are evident in the figure that represents two populations of droplets, named “main” droplets and “satellite” droplets. Two values of V_N at the center of two steps are identified as representative of the stopping potentials V_S for the two populations, respectively. The accelerating potential was defined by Gamero-Castaño in Ref [21] using the stopping potential V_S and the potential between the needle and extractor. The

significance is that it allows calculation of the actual potential of the droplets at the point of origin, a value used in subsequent calculation of droplet size. This potential is equal to the needle voltage minus the amount of potential lost to irreversibilities in the forming jet.

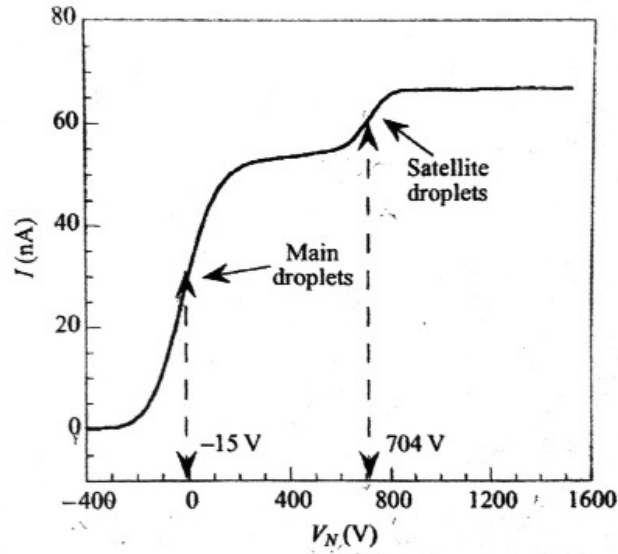


Figure 1.13 Typical stopping potential curve for electro spray in Gamero-Castaño's tests [Ref. 21]

Droplet charge and time of flight were measured by a capacitive detector in Gamero-Castaño's tests, shown in Figure 1.14, which was based on Shelton's single sensing tube design and also similar to that used by Hogan and Hendricks [19]. The "collimator," which is a passage with a small aperture on the collimating electrode plate, only allowed a single droplet to pass through the inner sensing tube at a time. As the droplet passing through the sensing tube, a charge was induced on it and a voltage trace was generated through the capacitor C . The actual capacitance between the sensing tube and ground is represented by C_E (see the equivalent circuit for the detector system shown at the bottom of Figure 1.14.) The inner sensing tube was connected to ground through a

resistor R which produced a signal consisting of a voltage trace with two sharp peaks as the droplet passed through the detector. The time-of-flight of droplet was determined by the two peaks and the charge was determined by

$$q = \frac{1}{2} \int_{-\infty}^{\infty} \frac{|V(t)|}{\Omega} dt \quad (1.3.1)$$

where $V(t)$ is the voltage trace generated when a droplet passing through the detector and Ω is the resistance between the sensing tube and ground.

Along with the known accelerating potential determined from Figure 1.13, a more accurate droplet specific charge was determined and droplet diameter was found using Equation (3.3.7).

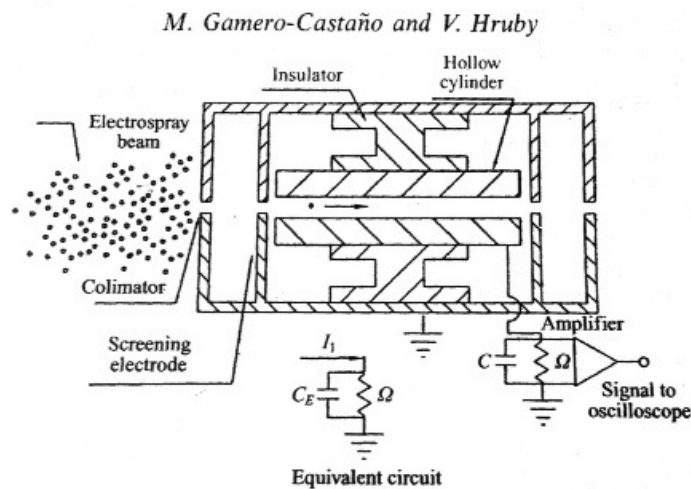


Figure 1.14 Schematic of capacitive detector used by Gamero-Castaño to measure charge and specific charge of electro spray droplets [Ref. 21]

More recently, important progress was made in ICD design by Gamero-Castaño [22], who designed an induction charge detector with multiple sensing stages to increase

the charge detector sensitivity. A set of aligned cylindrical electrodes was used in vacuum to measure the charge of a particle multiple times. As shown in Figure 1.15, the entrance of the detector was a long and narrow collimator channel which limited the number and acceptance angle of the droplets entering it. There were eight identical tubes aligned coaxially with each other and the entrance. The first and last tubes were grounded to shield the sensing tubes from the incoming or outgoing droplets and to increase the sharpness of the rectangular, output signal waves. The remaining six tubes formed two “sensor blocks,” identified as “Sensor 1” and “Sensor 2” and each had three alternating sensing tubes. As a charged droplet passed through the tubes, the potential difference between the tubes induced a rectangular wave, which had an amplitude proportional to droplet charge and a frequency inversely proportional to its time of flight. The collector received charged droplets exiting from the sensing tubes. All these tubes were supported by an insulator to isolate them from the outer grounded housing.

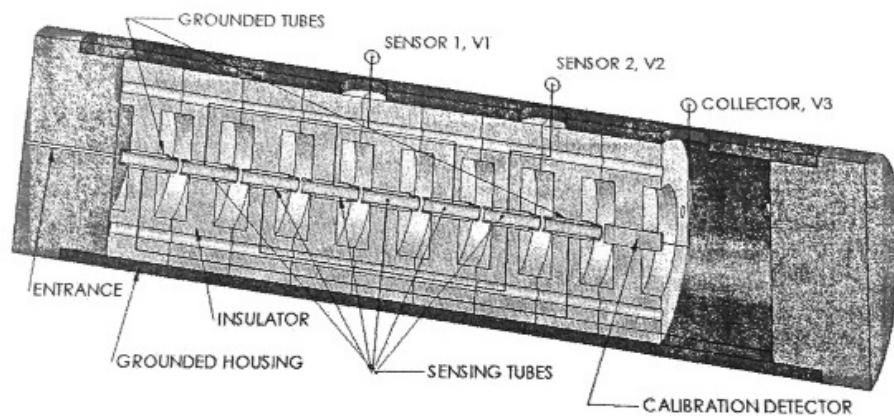


Figure 1.15 ICD with multiple stages by Gamero-Castaño [Ref. 22]

Figure 1.16 shows an output signal wave from the multiple stage detector induced by a charged droplet. The voltage difference, “ $V1 - V2$ ”, represented a rectangular wave

with three cycles created by the passage of a droplet through the alternating sensing tubes of sensor 1 and 2, which was used to calculate the droplet charge. The wave would be symmetric if the capacitances of sensor 1 and 2 were the same. The time difference between t_1 and t_2 was defined as the time-of-flight.

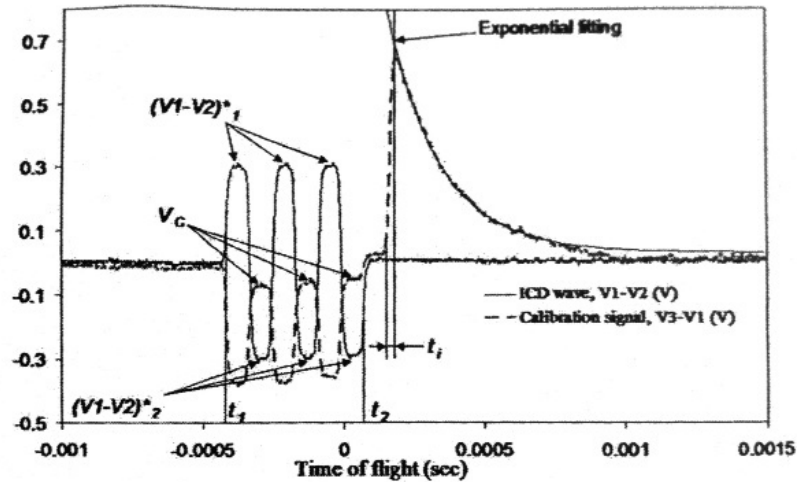


Figure 1.16 Signal induced by a charged droplet passed through the multiple stage ICD detector in Gamero-Castaño's tests [Ref. 22]

Generally, an n -fold periodic signal generated by n sensing tubes that measures n independent droplet charges, increases the signal-to-noise ratio of induced charge signal by a factor of \sqrt{n} by reducing the standard error of the charge measurement. For a periodic signal, the second signal increases the signal to noise ratio by a factor of $\sqrt{2}$, which means the charge detection limit was lowered by a factor of $\sqrt{2}$ in the time domain compared to an induced charge detector with one sensing tube. In principle, analysis of the data from this instrument in the frequency domain, for an unlimited number of periodic signals, could increase the sensitivity of the multiple stage detector to

one electron charge. But the unlimited number of sensing tubes in one sensor block which is connected to one operational amplifier does not improve the charge standard error (or the charge detection limit). This is because each sensing tube increases the net capacitance of the amplifier, which is inversely proportional to its sensitivity. The number of the sensing tube in one sensor block should be limited so that their equivalent capacitance does not exceed the intrinsic capacitance of the amplifier. To further reduce the standard error of the charge measurement, multiple ICD sensor blocks can be arranged in series and recorded independently. This device was designed to be able to significantly enhance charge resolution, and at least in principle, lower the detection limit down to one electron charge.

Chapter 2 Model for Droplet Charging and Breakup

2.1 Introduction

As discussed in Chapter 1, this work seeks to investigate the possibility of actively controlling the droplet size distribution through the use of electron bombardment to induce droplet breakup or fission. In the proposed system, a negatively charged droplet plume is exposed to an electron flux, which is generated by a cathode (filament) and accelerated by an electric field induced by an anode plate electrode, as shown in Figure 1.1. A droplet will break up when it is charged beyond the Rayleigh limit. The droplet is then captured by the CDMS that measures the charge, time-of-flight and specific charge of the droplet. With this information, the diameter of droplet after breakup can be calculated and the feasibility of this technique verified.

To determine whether this approach to controlling droplet size is feasible, the electron flux and energy used to charge the droplet were estimated to determine if it was sufficient for the given experimental geometry. This Chapter presents a simplified charging model used to help answer these questions and to guide the choice of cathode operating conditions such as filament heater current and anode voltage.

2.2 Electron Flux

As discussed in Section 1.3, the plume produced by the electrospray is assumed to consist of a nearly monodisperse distribution of droplets that are below the Rayleigh

charge limit. To charge the (negatively charged) droplets to a sufficient level as to reach the Rayleigh limit to induce fission, a source of electron flux is required. In this Section, the Richardson-Dushman equation is used to model a thermionic emitter and a simplified energy balance is used to estimate the density and velocity of electrons incident on the passing droplets.

In the region between the cathode and the anode plate, through which the droplets pass, the electron current density is given as a function of the local density and velocity as

$$J_e = -en_e v_e \quad (2.2.1)$$

where $-e$ is the charge carried by an electron, n_e is the number density of electrons, and v_e is the velocity of electrons. The electron velocity v_e can be found by solving the energy conservation equation for the electrons in the (collisionless) region between the filament and the anode plate.

Figure 2.1 shows an electron that is emitted by the filament and accelerated by the positively biased anode plate A. One end of the filament is grounded. As a result, the electron will be created at near-zero potential. This assumption is valid because a potential difference of at most a few volts is all that is needed to sustain emission from the filament. The distance between filament and anode plate is $y = H$.

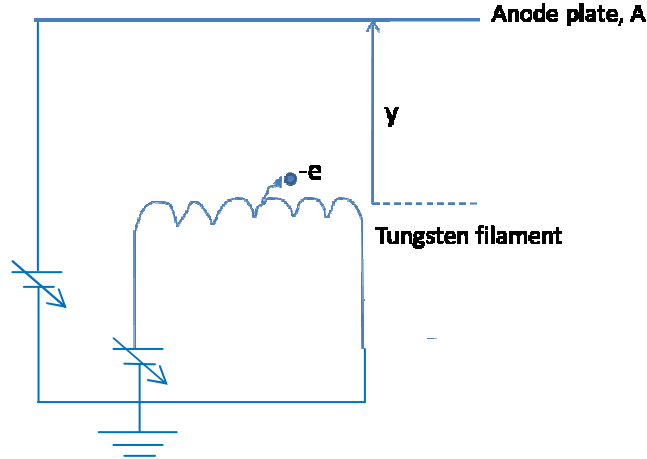


Figure 2.1 Conceptual diagram for electron energy balance

Total energy for a collisionless electron at any intermediate point between the filament and anode will be constant and is given by

$$E_{total} = E_{mech} + E_{thermal} = \frac{1}{2} m_e v_e^2 (y) - e\phi(y)_e + \frac{1}{2} k_B T_e = const \quad (2.2.2)$$

The mechanical energy of an electron consists of kinetic energy $\frac{1}{2} m_e v_e^2 (y)$ and potential energy $-e\phi(y)_e$ at any location y , where m_e is the mass of electron and $\phi(y)_e$ is the local potential relative to the (grounded) filament. The potential will be given by $\phi(y=H) = V_{an}$ at the anode where V_{an} is the voltage applied to the anode to accelerate the electrons. The thermal energy term represents the energy of the electrons emitted at ground potential and with a translational thermal energy of $\frac{1}{2} k_B T_e$, where k_B is the Boltzmann constant. The factor of $\frac{1}{2}$ results from the assumption the electrons are emitted from the cylindrical filament with only a radial velocity component [23].

Eq. (2.2.2) can be represented at location of $y = 0$ and $y = H$ by

$$E_{total} = 0 - eV_{an} + \frac{1}{2}k_B T_e, y = 0 \quad (2.2.3)$$

$$E_{total} = \frac{1}{2}mv_e^2 + 0 + \frac{1}{2}k_B T_e, y = H \quad (2.2.4)$$

The electron drift velocity is defined as,

$$v_d(y) = \sqrt{\frac{2e\phi(y)_e}{m_e}}, 0 < \phi(y)_e < V_{an} \quad (2.2.5)$$

It is assumed that an electron is accelerated from a zero drift velocity to its maximum velocity at the location of anode plate. Assuming the only collision that occurs is with a droplet, the maximum value of the drift velocity will correspond to the electron falling through the entire potential difference between the filament and the anode plate. This maximum value of $v_d(y = H)$ is therefore used as the electron velocity in following simplified calculation, which is

$$v_d(y = H) = \sqrt{\frac{2eV_{an}}{m_e}} \quad (2.2.6)$$

The Richardson-Dushman Equation is used to calculate the current associated with the thermionic emission of electrons [24]. The emission current density J_e is given by Eq. (2.2.7), which provides an estimate of the current density as a function of the filament temperature and material properties (specifically, the work function and reflection coefficient),

$$J_e = A(1-r)T^2 \exp\left(-\frac{e\phi}{k_B T}\right) \quad (2.2.7)$$

In this equation, $A = \frac{4\pi mk^2 e}{h^3}$ is a combination of physical constants which for tungsten is equal to $A = 60.2 \text{ amp/cm}^2 \text{ deg}^2$ (Ref. [24]). For pure metals the reflection coefficient r is of the order 0.05, T is temperature of the (tungsten) filament in Kelvin, and φ is electronic work function (4.30 eV for tungsten) [24].

Solving Eq. (2.2.1) along with Eq. (2.2.5) and Eq. (2.2.7), the number density of electrons required for the charging calculation can be estimated. This density is used in the calculation of the estimated charging time.

In calculating the charging time, it is assumed that all the emitted electrons will drift towards the positively biased anode plate. Since the electrons are assumed to be collisionless with respect to any residual neutral gas or ions, they travel towards the anode and either “collide” with a droplet or are collected at the anode electrode plate. The number density of electrons at the anode plate will be lower than at the filament as a result of the geometric spreading. This is a result of the fact the anode electrode surface area is much larger than that of the filament emission surface area. Assuming that all the current produced by filament is collected by the anode plate,

$$I_e = J_e \cdot A_f = J_{e_{anode}} \cdot A_s \quad (2.2.8)$$

where “anode” denotes values at the anode location, $A_f = \pi dL_{fil}$ is the surface area of the filament with a diameter of 0.254 mm (0.01 inch) and length of 12.7 cm that emits the electrons, and $A_s = WL_{an}$ is area of anode plate of length 12.7 cm and width 12.7 cm that collects the electrons. Using Eqns. (2.2.1) and (2.2.8), the number density of electrons at the filament location can be written as

$$n_{e_{anode}} = \frac{J_e}{ev_d} \cdot \frac{A_f}{A_s} \quad (2.2.9)$$

where v_d is the electron drift velocity which corresponds to the value at the anode plate ($y=H$). A reduction in electron density results from both the increase in area as well as an increase in drift velocity as a result of acceleration from the grounded filament to the positively biased anode plate.

It is assumed that the electron current (not density) remains constant, the attenuation in the electron current is neglected which results from electrons being absorbed by passing droplets. These are reasonable assumptions for the purposes of estimating the number density because 1) the (frontal) surface area of passing droplets will likely be small compared to the surface area of the anode electrode and 2) only electrons with sufficient energy can penetrate the potential well surrounding droplets to reach their surface. Other electrons will be deflected and continue towards the positively-biased anode electrode. Finally, Eq. (2.2.9) represents the electron density at the anode position, where the potential is known. This quantity provides an order of magnitude estimate of the electron density within the region (between the filament and anode plate) where they encounter the droplets. The passing droplets will be distributed in the region between the cathode and the anode, and because they carry their own charge, they will alter the space charge distribution (and hence the local electric potential). The electron velocity and number density is therefore a function of the position and as a result, the local potential. For this reason, the density given by Eq. 2.2.6 is at best an order of magnitude estimate obtained by neglecting the effect of space charge in the region and assuming electrons are not lost to surfaces other than the anode.

The primary advantage of this cathode design is that the length of filament L_{fil} is easily increased as necessary to insure that passing droplets have a sufficient residence time in the electron beam. This “exposure length” is a length scale which drives the facility size for a given experiment and can be estimated as follows.

A droplet in the electrospray plume can be described by a specific charge $(q/m)_{t=0}$ as it enters the electron beam, a radius r_d , surface tension γ , and fluid density ρ . The maximum specific charge for that droplet is given by the Rayleigh criteria:

$$\left(\frac{q}{m}\right)_{\max} = \frac{6(\epsilon_0\gamma)^{1/2}}{\rho r_d^{3/2}} \quad (2.2.10)$$

As a droplet is exposed to the electron flux, characterized by a current density J_e , its mass remains relatively constant since mass loss is very small while its charge increases as a result of electron capture (droplets become more negative). This assumes that evaporation is negligible. For a droplet of mass m_d , the change in specific charge from point of entry until breakup can be written as

$$\left(\frac{q}{m}\right)_{\max} - \left(\frac{q}{m}\right)_{t=0} = \frac{J_e \pi r_d^2}{m_d} \lambda_{res} \quad (2.2.11)$$

Where λ_{res} is the residence time (in the electron beam) required to reach the Rayleigh limit. In this expression, it has been assumed the uniform electron flux is intercepted by the droplet cross sectional area. This will require the electron kinetic energy, a controllable parameter, be sufficient to overcome electrostatic repulsion from the droplet as it is charging up. Solving for the residence time, the relation is obtained

$$\lambda_{res} = \frac{m}{J_e \pi r_d^2} \left[\left(\frac{q}{m} \right)_{\max} - \left(\frac{q}{m} \right)_{t=0} \right] \quad (2.2.12)$$

For a droplet velocity v_d , the required exposure length will be $L = v_d \lambda_{res}$. With known initial specific charge, droplet velocity, and electron current density, the exposure length and residence time can be predicted. Figure 2.2 shows the results of the residence time and exposure length estimates for droplets, which uses the values of droplet velocity and initial specific charge measured by detector. Their initial radii were assumed to range from $0.75 \mu m$ to $7 \mu m$ based on the measurement for droplets generated by electrospray in vacuum chamber. The radius of $7 \mu m$ represents the charge carried by the droplet is as close as to the charge of Rayleigh limit, but not equal. Smaller initial sized droplet carries smaller initial charge. From the results of this calculation, for droplets with the assumed initial specific charge and radius to reach the Rayleigh limit, an exposure length of 10-20 cm is sufficient. It shows that for the droplet with higher assumed initial charge, the required exposure length and required residence time to reach the Rayleigh limit are both smaller. This is in consistent with the Rayleigh criterion. This estimate assumes that the droplets have the same velocity v_d , the electron current density J_e is uniform, and the droplet breaks up at the Rayleigh limit charge. Although it's useful from the standpoint of initial experiment design, it underscores the need for higher fidelity numerical models to better understand the charging process.

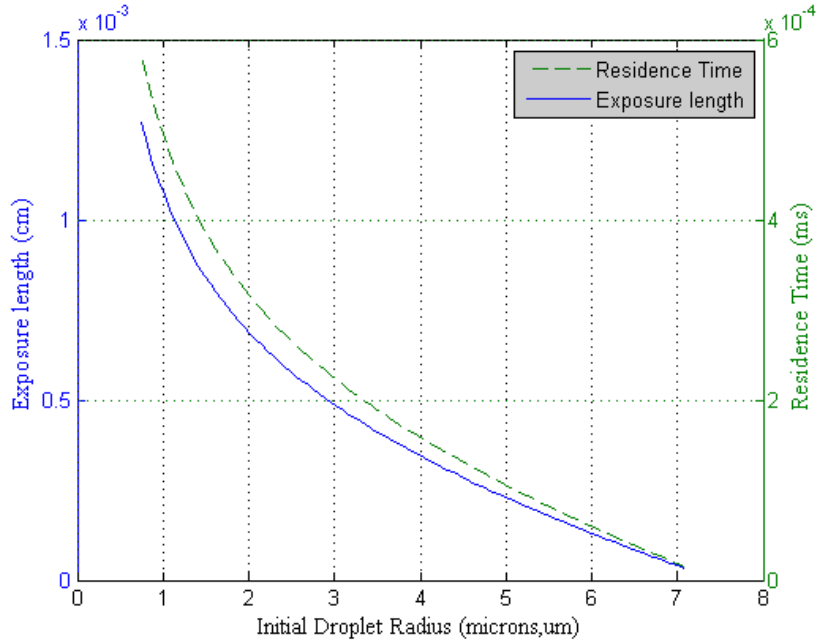


Figure 2.2 Exposure length and residence time (to reach Rayleigh limit) as a function of droplet radius.

Note: Calculation corresponds to droplet velocity $v_d=21.75$ m/s,

initial specific charge $\frac{q}{m} = 0.15$ C/kg, and electron current density of

$$J_e = 7.66 \times 10^3 \text{ A/m}^2.$$

2.3 Droplet Charging and Breakup

Negatively charged droplets that are exposed to an electron flux for a period of time will be charged up to the Rayleigh limit and break into smaller droplets as a consequence. In this section, a simplified droplet charging model is used to investigate the sensitivity of the charging process to several key design parameters. In particular, it is desirable to have a means of calculating the droplet charge as a function of time given and initial droplet size, electron flux and mean electron energy.

An anode plate described in Figure 2.1 is biased positively with respect to the cathode. This produces a potential gradient which accelerates the electrons, insuring that a significant fraction of the electrons have sufficient kinetic energy to reach a target droplet. Increasing the electron flux reaching the droplets increases the rate of charging and should result in a droplet reaching the Rayleigh limit in a shorter period of time. A larger electron flux will also result in a shorter length for the charging. This is illustrated in the drawing in Figure 2.3, which shows a conceptual charging process with and without electron drift velocity, where a shortened charging time ($t_2 < t_1$) implies a shorter/smaller device. Note that the droplets begin with a negative charge and become more negatively charged when exposed to electrons. If no breakup occurred, the charge would reach some asymptotic value corresponding to the “floating potential” of an isolated, conducting droplet. The shortening of the charging time shown in Figure 2.3 occurs because a larger fraction of the incident electrons have sufficient kinetic energy to overcome the repulsive potential of the droplet. If only the drift velocity is increased (and not the overall emission current), then the benefit illustrated in Figure 2.3 may be offset due to a reduction in the current density as evident from equation 2.2.8. (a result of current continuity).

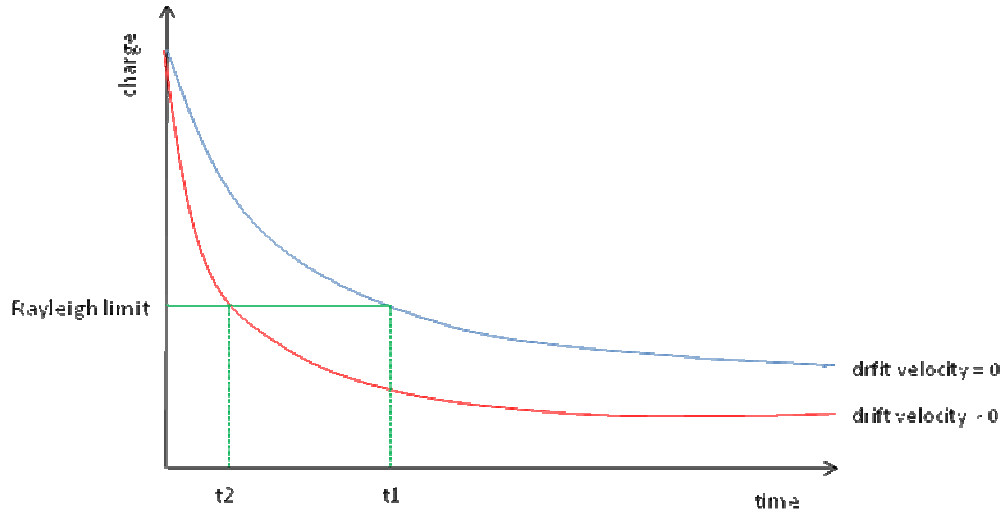


Figure 2.3 Conceptual diagram of charging process with and without electron drift velocity

The current-collection theory, which is the basis for the simplified charging model, is one that has been applied to the problem of dust charging in a plasma (droplets charged by electrons in our case). The remainder of this Section describes the simplified charging model.

In the present work, the droplets are generated at the point of jet breakup with a residual negative charge. This means the charging which occurs as the droplets travel through the electron beam always corresponds to a repulsive “current-collection” regime. In the repulsive regime, the collection area cannot be greater than physical cross sectional area of the droplet, as shown in Figure 2.4. Furthermore, not all electrons incident on the droplet cross sectional area will be captured since only those with sufficient kinetic energy can overcome the electrostatic repulsion of the negatively charged droplet. Electrons will either be repelled if they don’t have enough energy to penetrate the

potential barrier; or collide with and be collected by the droplet. For this reason, the current collection theory used for the repulsive case was based on the theory which has been developed for current collection to a planar (1D) probe [26]. In a one-dimensional analysis, all electrons with sufficient kinetic energy colliding with droplet will be collected.

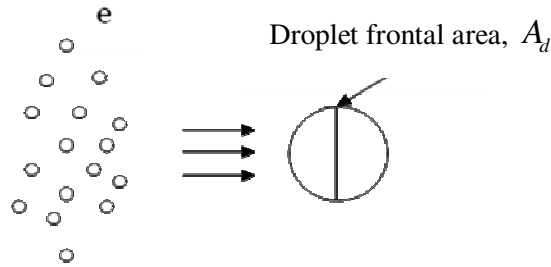


Figure 2.4 Conceptual diagram showing electrons collected by negatively charged droplet

Electrons can be described by the velocity distribution function $f(x, \bar{v}, t)$, which gives the number of electrons per unit volume with velocities between \bar{v} and $\bar{v} + d\bar{v}$ at position x and time t . The density of electrons at x and t is given by

$$n_e(x, t) = \int f(x, \bar{v}, t) dv_x dv_y dv_z \quad (2.2.13)$$

where the integration is over a region of velocity space. The electron current density to the droplet can be written

$$J_e = -en_e v = -e \iiint f(\bar{v}) \bar{v} \cdot \hat{n} dv_x dv_y dv_z \quad (2.2.14)$$

where \hat{n} is the normal to droplet surface. Because the droplet is so much larger than an electron, the curvature of the droplet can be neglected and the droplet treated as a 1-D

surface. It is assumed that the droplet presents a planar area for absorption equal to the cross sectional area as shown in Figure 2.4. The electron current density collected by negatively charged droplet can be written as

$$J_e = -e \int_{v_{\min}}^{\infty} \int_{-\infty}^{\infty} \int_{-\infty}^{\infty} f(v_x, v_y, v_z) v_z dv_x dv_y dv_z \quad (2.2.15)$$

where v_{\min} is the minimum velocity required for electron to overcome the potential barrier of the droplet. Integrating over two velocity components which lie within the collection area plane, eqn

$$J_e = -e \int_{v_{\min}}^{\infty} f_z(v_z) v_z dv_z \quad (2.2.16)$$

Where $f_z(v_z) = \int_{-\infty}^{\infty} \int_{-\infty}^{\infty} f(v_x, v_y, v_z) dv_x dv_y$. Calculation of the droplet current density is reduced to a one-dimensional problem. It is assumed the electrons have a velocity distribution which is Maxwellian. As described in Section 2.1, an anode plate is used in the experiment to accelerate electrons so a drifting velocity term is included. The electrons are then described by a drifting Maxwellian distribution, which is given by

$$f(v_e) = -e \left(\frac{m_e}{2\pi k_B T_e} \right)^{3/2} \exp \left(-\frac{m_e (v_z - v_d)^2}{2k_B T_e} \right) \quad (2.2.17)$$

For this charging analysis, the droplet cross sectional area A_d is considered as the equivalent of a planar probe collection area. So the current is calculated as

$$I_e = A_d J_e \quad (2.2.18)$$

Solving Eq. (2.2.18) with Eq. (2.2.16) and Eq. (2.2.17), the electron charging current carried by electrons to the negatively charged droplet can be solved and shown to be equal to [26]

$$I_e = A_d n_e \sqrt{\frac{T_e}{2\pi m_e}} \exp(-x_m^2) + \frac{en_e v_d}{2} [1 + \text{erf}(x_m)] \quad (2.2.19)$$

where A_d is the frontal cross sectional area of the droplet, and

$$\text{erf}(x_m) = \frac{2}{\sqrt{\pi}} \int_0^{x_m} \exp(-x^2) dx \quad (2.2.20)$$

$$x_m = \sqrt{\frac{m_e}{2T_e}} [v_d - v_{\min}] \quad (2.2.21)$$

$$v_{\min} = \sqrt{-\frac{2e\phi_d}{m_e}} \quad (2.2.22)$$

where ϕ_d is the potential difference between droplet and electrons. This potential difference will change with the time since both droplet charge q and droplet radius r_d are functions of time.

Using an expression used in dust charging analysis [28], the droplet charge can be related to the potential and also the charge current.

$$q(t) = C_d \phi_d(q(t)) \quad (2.2.23)$$

$$I_e = \frac{dq(t)}{dt} \quad (2.2.24)$$

where C_d is the capacitance of the droplet given by $C_d = r_d \exp\left(-\frac{r_d}{\lambda_{De}}\right)$ and λ_{De} is Debye length, defined as $\lambda_{De} = (\epsilon_0 k_B T_e / n_e e^2)^{1/2}$, where ϵ_0 is the vacuum permittivity, n_e is electron number density.

Therefore the droplet charge q_d can be determined by solving Eq. (2.2.19) through (2.2.24) with the number density of electron n_e given by Eq. (2.2.9). The “ode45” solver is used to solve for q in MATLAB by integrating the electron current from time 0 to 10000 seconds with an initial droplet charge of $q_0 = -6.0 \times 10^{-14} C$. These parameters were chosen based on representative values from our tests. Table 2.1 shows all the parameters used in the calculation.

Table 2.1 Parameters used in droplet charging model

Symbol	Quantity	Units
ϵ_0	8.85×10^{-12}	F/m
k	1.38×10^{-23}	J/K
e	1.60×10^{-19}	Coulomb
m_e	9.11×10^{-31}	kg
γ	2.80×10^{-2}	N/m
A	60.2	amp/cm ² deg ²
ϕ	4.3	eV
T	2.5×10^3	K
r	9×10^{-6}	m
q_0	-6×10^{-14}	Coulomb
A_f	1.01×10^{-4}	m ²
A_s	1.6129×10^{-2}	m ²

2.4 Results from Simple Charging Model Analysis

Figure 2.5 and 2.6 show the results of the droplet charging calculation with accelerating voltage V_{an} set to 1 volt. Figure 2.5 shows the charge as a function of time. Fig. 2.6 shows the minimum electron drift velocity v_{min} required for an electron-droplet collision to occur under different accelerating potentials. The droplet's Rayleigh limit charge of $Q_{rayleigh} = -0.3379 \times 10^{-14}$ C and the electron's drift velocity of $v_d = 5.93 \times 10^5$ m/s are indicated on the plots.

Similarly, Figure 2.7 and 2.8 show the corresponding results with the accelerating voltage V_{an} set to 20 volts. The droplet's Rayleigh limit charge is unchanged and the electron's drift velocity is $v_d = 26.5 \times 10^5$ m/s as shown on the plots.

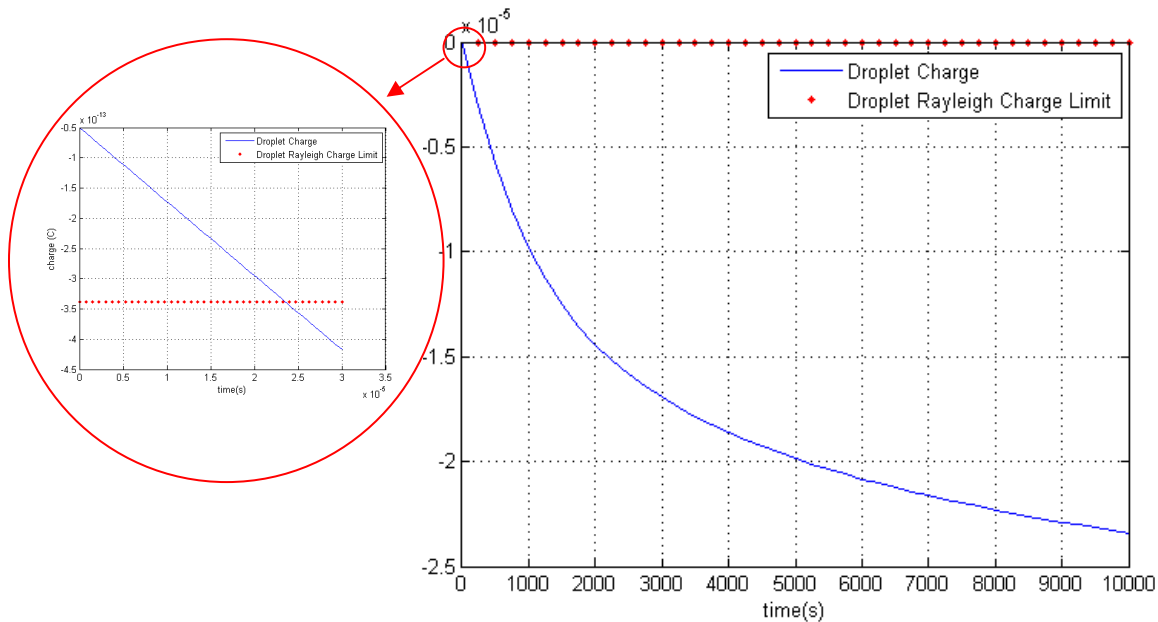


Figure 2.5 Negatively charged droplet charges up with $V_{an}=1V$ (q vs. t)

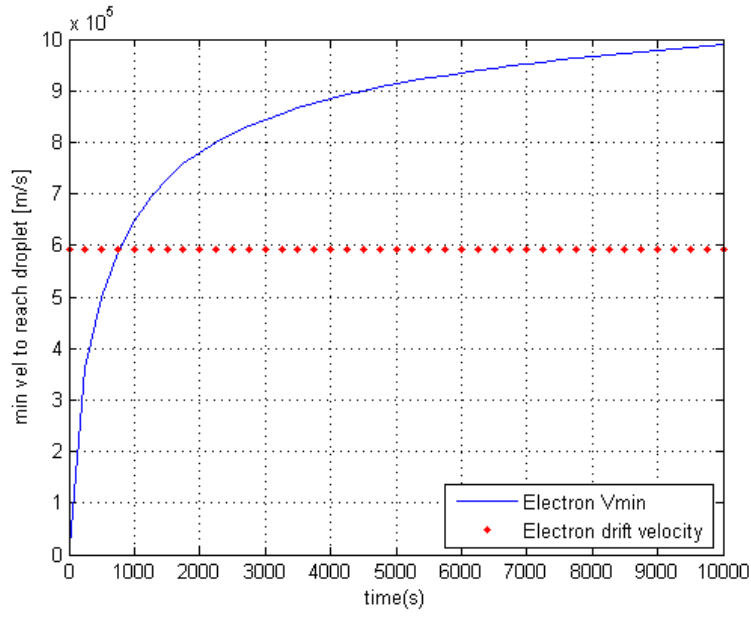


Figure 2.6 Negatively charged droplet charges up with $V_{an}=1V$ (v_{min} vs. t)

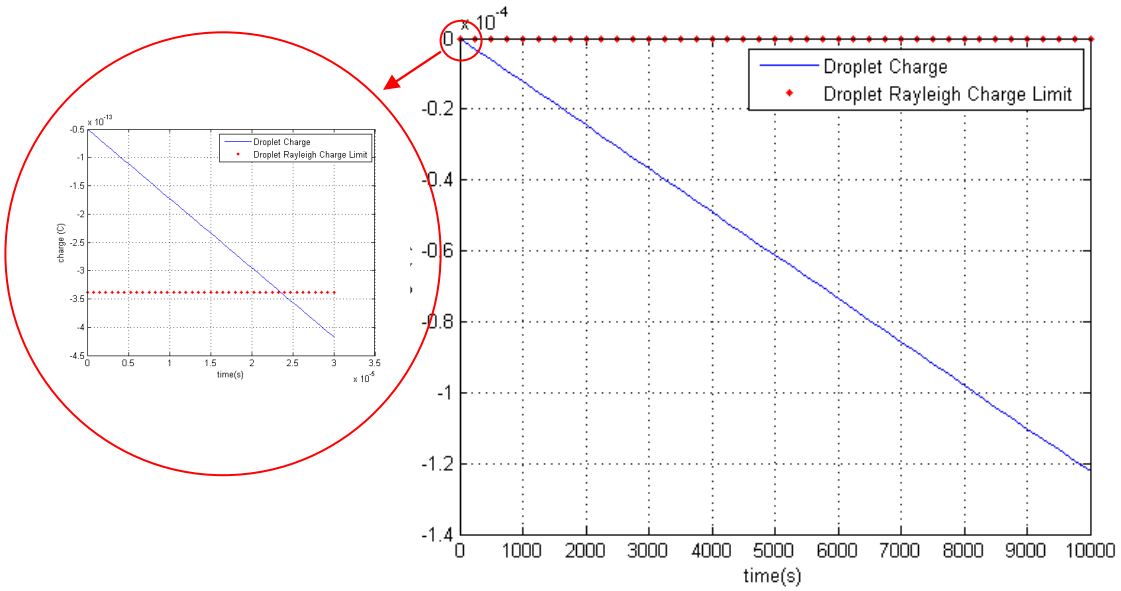


Figure 2.7 Negatively charged droplet charges up with $V_{an}=20$ volts (q vs. t)

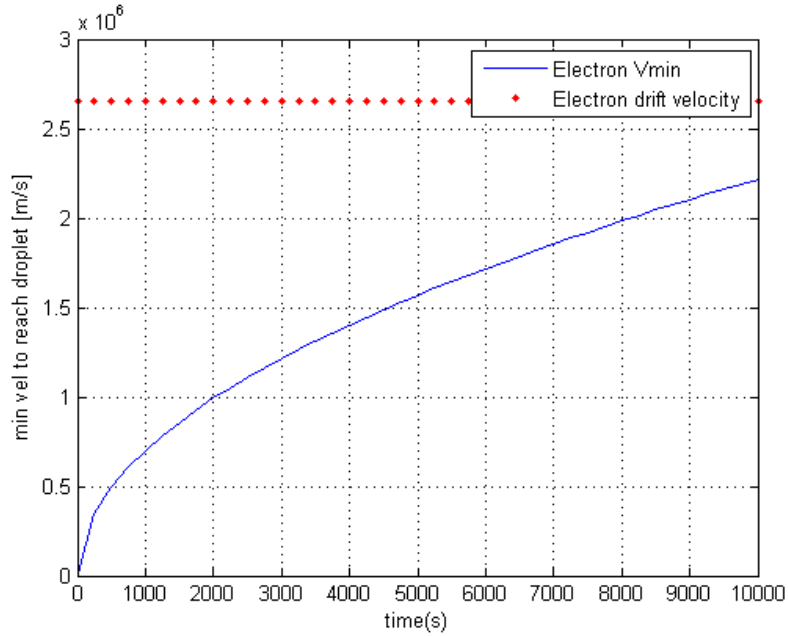


Figure 2.8 Negatively charged droplet charges up with $V_{an}=20$ volts (v_{min} vs. t)

Comparing Figure 2.5 and Figure 2.7, one can see the rate of droplet charging is different. The one with larger electron drift velocity ($V_{an} = 20V$) has a steeper slope representing a faster charging rate than the one with smaller electron drift velocity ($V_{an} = 1V$). Figure 2.8 shows that when the accelerating potential is as large as 20 volts, electron's drift velocity v_d is always larger than the required v_{min} . With this anode voltage, electrons would have sufficient energy to be collected by the droplet even if the droplet were to continue being charged for thousands of seconds. With the droplet velocities anticipated for this experiment (tens of meters per second), the residence time will be less than a second. The above calculation therefore suggests that an accelerating voltage of tens of volts should be sufficient to charge the droplet to the breakup limit if the assumptions made, particularly the initial droplet charge being in the range of “ $-3.5 \times 10^{-14} C$ ” to “ $-6 \times 10^{-14} C$ ”, are accurate. The range of values assumed for the droplet

initial charge is based on the measured charge of droplets generated from electrospray in tests.

The droplet carries an initial charge as a result of its formation in the electrospray. If this initial charge is, in fact, close to the Rayleigh limit, then when the cathode emits electrons, the droplet should begin breaking up just as it enters the electron bombardment region. With this small charge difference (approximately 3×10^{-14} C), the Rayleigh limit is reached in few seconds as shown in the expanded insets of Figure 2.5 and Figure 2.7. Droplets that carry less negatively value of the initial charge, which are not close to Rayleigh limit) should be more likely to show evidence of charging up in tests.

The minimum velocity v_{\min} required for the electron to overcome the droplet electrostatic potential barrier increases along with the increasing of the droplet charge since v_{\min} is a function of charge difference between droplet and electron (Eq. (2.2.22)). Droplets will keep collecting electrons until v_{\min} increases to the point where it is larger than the electron drift velocity v_d . As the negative charge (and hence the repulsive, negative potential) builds up on a droplet, a condition is reached when most electrons have velocities smaller than v_{\min} , ($v_{\min} > v_d$) and the droplet charging rate gets slower compared to the rate at the beginning of the charging process. A small portion of electrons with sufficient velocity can still reach the droplet. In this case, the droplet doesn't stop charging because of those small portion of electrons in the high energy tail of the Maxwellian distribution that still have sufficient energy. As a result, the droplet will continue to charge up at an ever decreasing rate.

Chapter 3 Experimental Setup and Methodology

3.1 Introduction

The experimental setup included a vacuum facility and equipment needed to generate an electrospray, expose the plume to an electron flux, and the charge detection mass spectrometer used to characterize the droplet properties. There were several important reasons for performing these tests in a vacuum chamber. The most important reason is that the thermionic cathode used to generate the electrons will only operate for a very limited time when exposed to oxygen. In addition, the absence of an appreciable atmosphere during tests minimizes the complication of drag and convective evaporation affecting the droplets. The three primary elements of this experiment were the source used to generate the electrospray, the source used to generate the bombarding electrons, and the Charge Detection Mass Spectrometer (CDMS) used to measure the droplets stopping potential, charge, time-of-flight, and diameter. All three of these elements will be described in detail in the following sections. This chapter is organized as follows: first, the vacuum chamber and electrospray source are described. This is followed by a description of the CDMS operation, including presentation of an analytical, electrostatic model of the induced charge obtained for a charged droplet entering the sensor tube. This model was used to evaluate the design of the inductive charge detector. This is followed by a description of the mechanical construction of the CDMS, the amplifier and data acquisition system used, the methodology used for the retarding potential measurement and a discussion of the measurement sensitivity. The last section of this chapter presents a description of the electron source (cathode) used for droplet charging.

3.2 Vacuum Chamber and Electrospray Source

All of the tests were conducted in one of the WPI vacuum facilities in Higgins Laboratory. The chamber used was a bell-jar type with an 18 inch in diameter, 30 inch tall stainless-steel chamber with base pressure on the order of 10^{-5} Torr. This test facility is shown in Figure 3.1. The chamber is rough-pumped by a mechanical pump down to the range of 10^{-2} Torr and then pumped down further to range of 10^{-5} Torr or lower by a vapor diffusion pump. As will be discussed later, for most of the tests reported here, the pressure in the chamber during testing was on the order of 10^{-3} Torr because of a limitation of the diffusion pump used in the tests.



Figure 3.1 Facility used for electrospray including the vacuum chamber, Pyrex bottle containing fluid and digital camera to monitor the Taylor cone and jet.

The electrospray apparatus, consisting of the capillary (needle) and fluid reservoir, is mounted external to a port on the vacuum chamber. The fluid is stored in a Pyrex reservoir which can be pressurized to control the flow rate. For these tests, one side of the reservoir was left open to atmosphere so that the fluid inside is driven by the pressure

difference between the ambient room pressure and chamber pressure (1 atm). Early tests incorporated pressurization of the bottle to increase the flow rate, but later this was determined to be unnecessary. The electrospray needle is mounted to a flange attached to the outside of the stainless steel vacuum chamber. At all times the spray was contained in the vacuum chamber.

The electrospray needle is made of stainless steel with an inner diameter of 127 μm (0.005 inch) and an outer diameter of 508 μm (0.02 inch). Since the needle wall is relatively thick compared with the inner diameter, the tip was chamfered at an angle of 60° on a special lathe to facilitate the formation and attachment of a stable Taylor-cone. For a given needle-extractor distance and needle voltage, a chamfered needle tip requires less voltage to form a stable Taylor-cone.

The fluid used is a mixture of an ionic liquid “EMI-Im”(1-ethyl-3methylimidazolium bis(trifluoromethylsulfonyl) imide) in tributyl phosphate (TBP). This mixture was selected because of its moderate conductivity (10^{-3} - 10^{-2} S/m) tested previously by Blandino [21] and Gamero-Castaño *et al.* [22]. A dilute mixture was used, $10^{-4}\%$ by mass. As a result, the liquid’s physical properties, for the purpose of estimating the Rayleigh specific-charge limit, flow rate, and droplet size were taken to be those of the solvent TBP. The dielectric constant of TBP is $\epsilon = 8.91$, surface tension is $\gamma = 0.028$ N/m and the density is $\rho = 976$ kg/m³. The fluid properties can be used to make an estimate of expected droplet size based on published scaling relations [3]. For this mixture the flow rate from is $Q \sim \frac{\gamma\tau_e}{\rho}$ on the order of 10^{-6} cc/s, where τ_e is an electrical relaxation time give by $\tau_e = \epsilon\epsilon_0 / K$ for a fluid with electrical conductivity K . The

characteristic droplet size from $d \sim \left(\frac{\gamma_e^2}{\rho} \right)^{1/3}$ is estimated to be approximately 120 - 560 nm corresponding to an electrical conductivity of 10^{-2} - 10^{-3} Si/m respectively. The CDMS with a size resolution of 78 nm (see Section 4.4) is capable of measuring the droplets in this range.

The high voltage (HV) power control system used to generate the electrospray, called the Telemetry Control and Capture system (TCAC), was designed and built by a WPI undergraduate (Rosenblad [30]) to allow full computer control of the needle voltage and data recording of the needle voltage and current. Power is supplied by a Glassman EH series high voltage power supply (model No. PS/EH25R04.0) with a maximum voltage and current rating of 25 kV and 4 mA respectively. The TCAC uses a LabView interface to control the output of the Glassman power supply as well as to record the needle voltage and current. The user interface for the virtual instrument or “vi” is shown in Figure 3.2. The power supply can be controlled either by manually using the vi, or using “Auto-sweep” mode on the vi. The TCAC also controls a second power supply, a Spellman SL10 high voltage supply which is used to bias the retarding screen used in the stopping potential measurements (Section 3.3.5). Although the Spellman and Glassman can operate up to 3.3 kV and 25 kV, respectively, the TCAC limits the maximum operating voltage for both supplies to 2.5 kV for operator safety and to prevent damage to the data acquisition system. Both power supplies can be calibrated using the vi.

Two high voltage (HV) test ports on TCAC front panel are used for voltage telemetry and control calibration by attaching a Fluke multimeter using a 1000:1 voltage probe to measure the actual output of the voltage versus the command voltage input sent

to the TCAC. The current signal calibration uses a Keithley Model 6514 system electrometer in series with a 100 M Ω resistor. The “ADC” and “I ADC” windows right above two slider bars (see Figure 3.2) indicate calibrated values of the voltage and current, respectively. Along with the commanded voltages, one can find the calibration equations for voltage and current separately. The resulting calibration equations are entered into the TCAC vi so that the voltage and current displayed are the calibrated values.

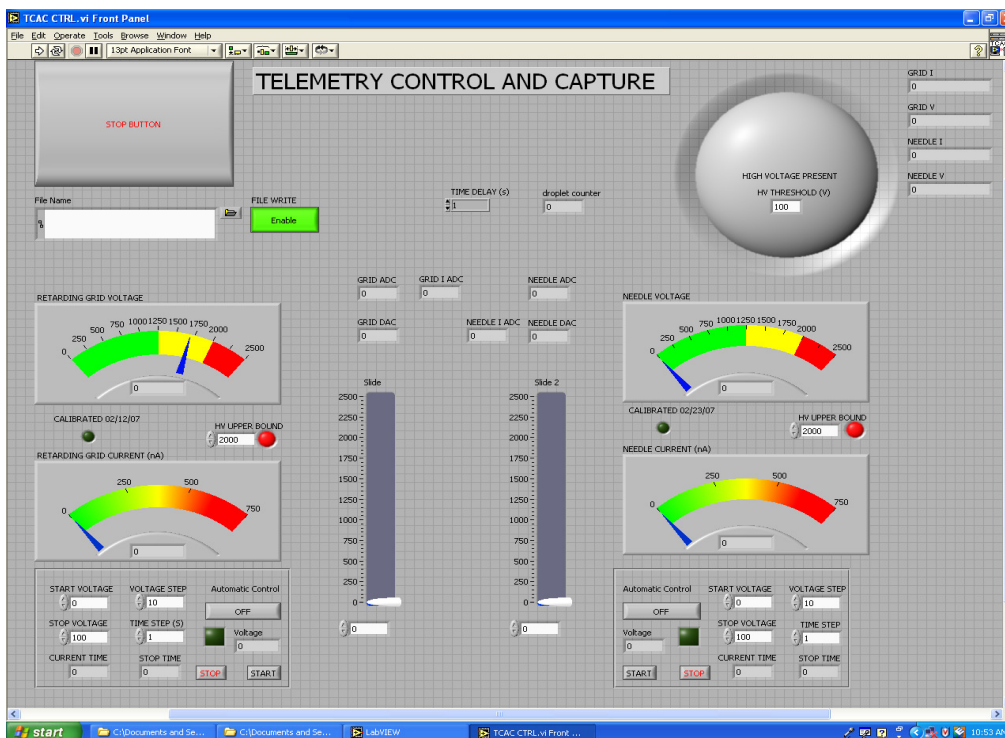


Figure 3.2 Interface of TCAC vi for Spellman & Glassman power supplies

Imaging of the electrospray is made with a high-resolution, monochrome, progressive scan Pulnix-1325 camera using a Meiji UNIMAC Macrozoom with a magnification range of 0.7 – 4.5. This camera has a 1392 (H) \times 1040 (V) active pixel area with a CCD cell size of 6.45 μm \times 6.45 μm . Figure 3.3 shows an image of the

electrospray operating in this facility which was taken by the Pulnix camera. The spray shown was operating with positive droplet emission (picture was taken during an early demonstration test) with a 2.9×10^{-4} % (by wt) mixture of EMI-Im in TBP. The applied potential difference and resulting emission current were approximately 1689 V and 52 nA with 108 μm (0.00425 inch) inner diameter needle. For the work described here, the larger needle described in Section 3.2 was used and negative droplets were generated at a nominal needle voltage of -2100 V with a 10^{-4} % mixture of EMI-Im in TBP. The appearance of the jet produced in the present tests was identical to that shown in Figure 3.3.

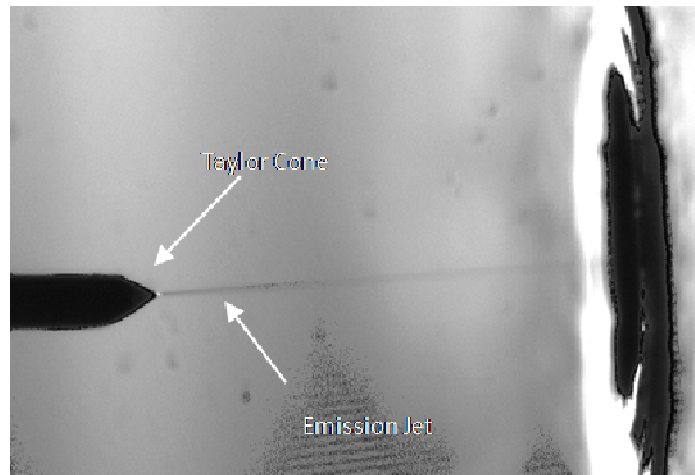


Figure 3.3 Photograph of electrostatic spray operating at $V_n=1688$ V, $I_n=52$ nA and $P_c = 7.1 \times 10^{-5}$ Torr.

Note: Fluid mixture corresponded to a concentration of 2.9×10^{-4} % EMI-Im in TBP.

3.3 Charge Detection Mass Spectrometer (CDMS)

3.3.1 Introduction

A detailed review of the theory and literature related to inductive charge detectors was presented in Section 1.5. A charge detection mass spectrometer (CDMS), based on Shelton's single sensing tube theory [16], was designed and built to measure the droplet charge. An estimate of the induced droplet charge on the sensor tube as a function of time was made using an electrostatics model presented in Weinheimer [31]. This analysis of an ideal detector is discussed first to show how the voltage waveform for a droplet entering and leaving the sensor tube varies as a function of droplet charge, velocity, and tube inner diameter. The discussion of the idealized detector is then followed by a description of the mechanical construction of CDMS, the amplifier circuit, and the automatic wave capture, data acquisition software. A retarding potential measurement methodology is then discussed in detail followed by a measurement sensitivity analysis for the CDMS. The chapter concludes with a description of the charging apparatus used to generate the electron flux for droplet charging.

3.3.2 Model Used for Inductive Charge Detector design

Figure 3.4 shows the different parts of the CDMS. A charged droplet passing through a conducting cylinder will induce an image charge which is equal to the actual charge carried by the droplet. If the sensor tube (conducting cylinder) is connected to ground through current-sensing circuitry, then the image charge will result in a current

flow which can be measured across a sensing resistor. The voltage across this sensing resistor is then amplified and captured by an oscilloscope. The RC time constant measured from the circuit is much shorter than the timescale of the pulse. It also allows the full discharge between two pulse signals. The RC effect on the output signal will be discussed in following.

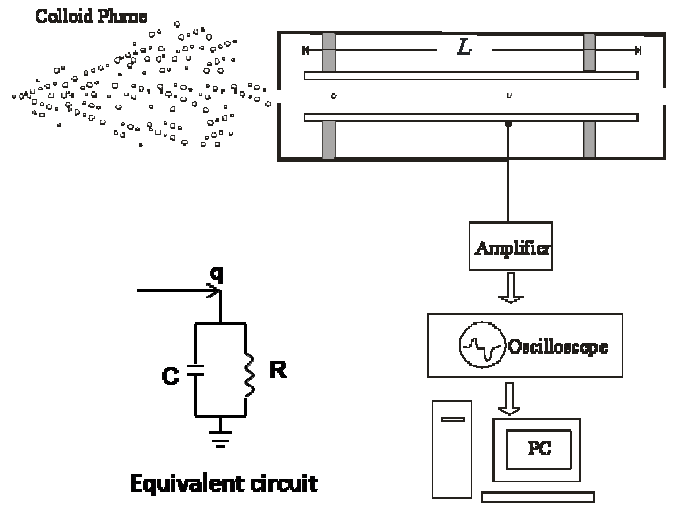


Figure 3.4 Schematic of the induced charge sensor

The induced charge on the detector as a function of time can be solved for analytically using electrostatic analysis as described by Weinheimer [31]. To estimate the induced droplet charge on the sensor tube as a function of time, the ratio of induced charge q' to actual charge on the droplet q is calculated in this section using Weinheimer's solution. This electrostatic solution is for a point charge inside a finite conducting cylinder.

$$\left| \frac{q'}{q} \right| = \sum_{n=1}^{\infty} \frac{2}{x_n} f(c/a, z_0/c, x_n) \frac{J_0 \left(x_n \left[\frac{r_0}{a} \right] \right)}{J_1(x_n)} \quad (3.3.1)$$

where c is half of the length of the sensor tube, a is the radius of the tube, z_0 and r_0 are droplet's axial and radial locations inside the tube (Figure 3.5),

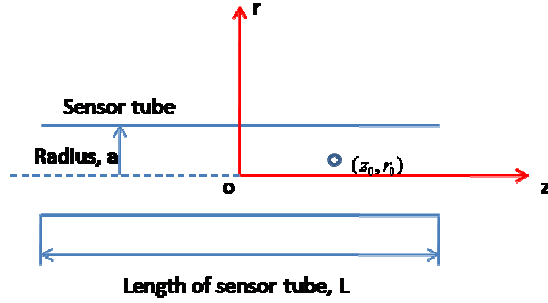


Figure 3.5 Schematic of droplet location in the sensor tube

x_n is the n th zero of 0th order Bessel function J_0 , J_1 is 1st order Bessel function and the function f is given by

$$f = 1 - \exp\left(-x_n \frac{c}{a}\right) \cosh\left(x_n \frac{c}{a} \frac{z_0}{c}\right) \quad \text{for } \frac{|z_0|}{c} \leq 1 \quad (3.3.2)$$

$$f = \exp\left(-x_n \frac{c}{a} \frac{|z_0|}{c}\right) \sinh\left(x_n \frac{c}{a}\right) \quad \text{for } \frac{|z_0|}{c} > 1 \quad (3.3.3)$$

Equations (3.3.1) - (3.3.3) are used to estimate how closely the induced charge will reflect the actual charge for the idealized case modeled with this analytical solution. This solution served the purpose of helping understand the effects of droplet misalignment and sensing tube aspect ratio. The analysis was performed for several cases of a droplet moving along a trajectory which is aligned and misaligned with respect to the tube centerline, for a the tube with a length-to-diameter (aspect) ratio $\frac{c}{a} = 7.59$, length of

$L = 0.0348m$ and radius of $a = 0.00229m$. Figure 3.6 shows the pulse shapes for the charge (top) and current (bottom) for a droplet moving parallel to the axis, evaluated at four radial locations equal to $\frac{r_0}{a} = 0, 0.6, 0.8, 0.99$. The results indicate how accurate the induced charge is for a given tube aspect ratio. The ratio $\frac{r_0}{a}$ of 0 represents the case where a droplet is travelling along the centerline axis and the ratio of 0.99 represents the droplet is travelling along (but not touching) the wall. Since the droplet could pass through the tube at any radial location, the results corresponding to these four radial locations showed the range of pulse shapes one might expect. It is notable that the pulse became more square and narrow as the droplet trajectory approached the wall. These four cases show that no matter what the radial location of the droplet is, the induced charge is likely to be within 99% of actual charge it carries for the aspect ratio tube used in these tests. From this it was inferred that the length of the tube used in our tests was sufficient (compared to its diameter) to produce an image charge with 99% of the actual charge carried by the droplet. The maximum error is 0.7% for the case of a droplet moving along the centerline. The current pulse shapes are also shown at the bottom of Figure 3.6. Four colors represent four various droplet radial locations (trajectories) described above, same as shown in the top plot. It is also notable that the current pulses became more narrow as the droplet trajectory approached the wall. These four current cases show that no matter what radial location of the droplet is, the induced current is likely to be within 99% of the actual current.

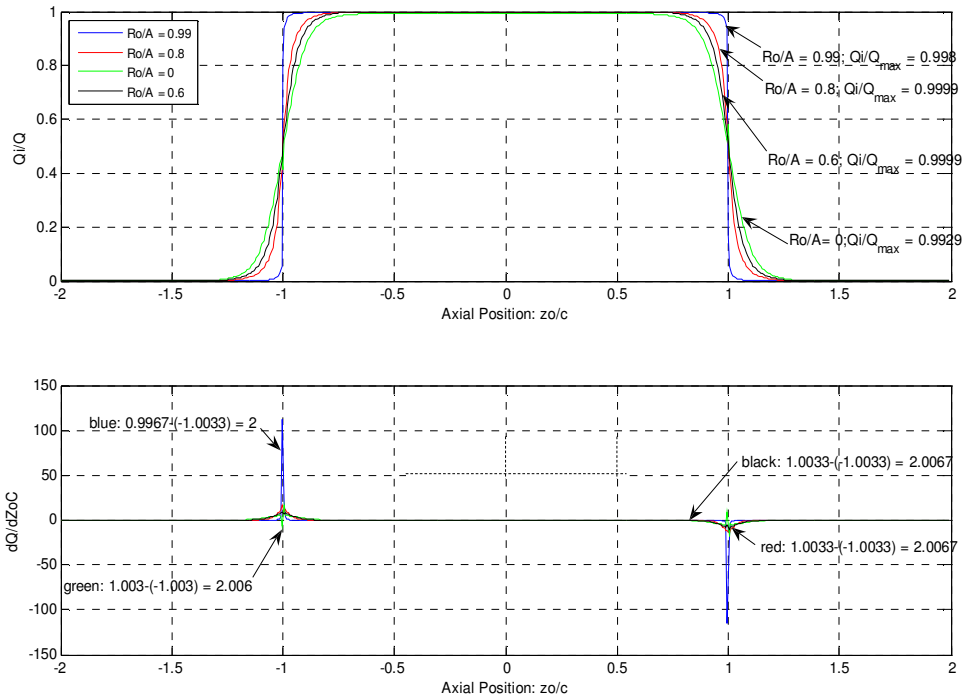


Figure 3.6 Induced charge and current for droplet travelling parallel to the tube axis, with an (trajectory) axis ratio of 0.99, 0.8, 0.6 and 0

A misaligned case was also studied for a droplet flying through the tube with a trajectory that is not parallel to the axis of the tube but at an angle. An extreme case in which the droplet enters the tube at the bottom and exits at the top was evaluated. Figure 3.7 shows the result of the droplet entering at an axial location with a radial ratio $\frac{r_0}{a} = -1$ and exiting at an axial location with a radial ratio $\frac{r_0}{a} = +1$. The induced charge on the sensor tube is 99.99% of the actual charge on the droplet, which means that for a droplet entering the tube with the largest angle that would still permit passage without hitting the inside, the induced charge on the tube is still very good.

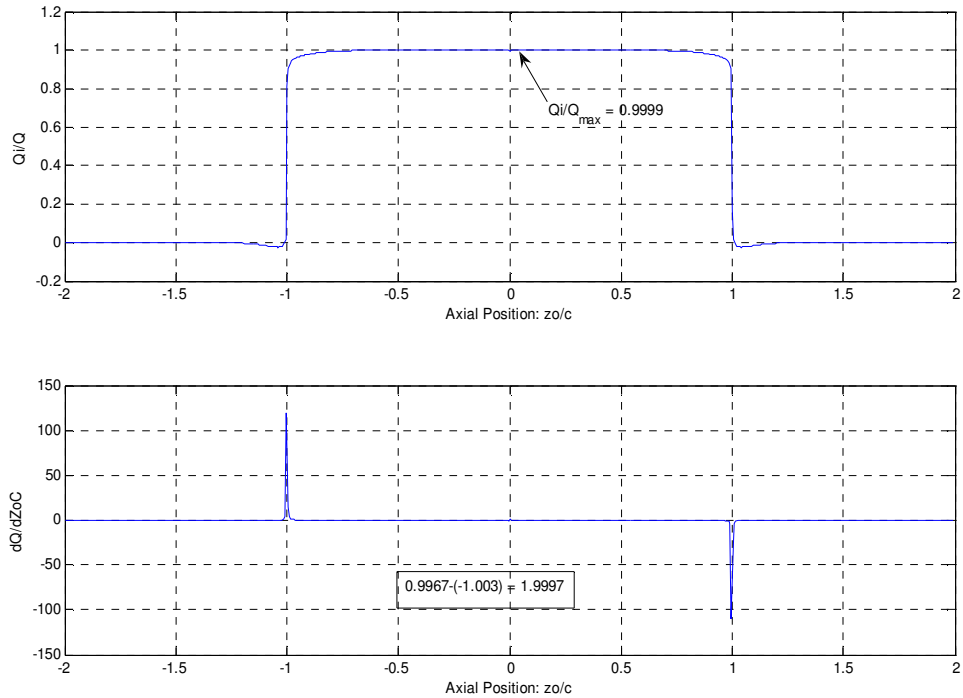


Figure 3.7 Induced charge and current for droplets travelling un-parallel to the axis of tube, droplet enters with $\frac{r_0}{a} = -1$ and exits with $\frac{r_0}{a} = +1$.

These calculations suggest that a sensor tube with a length-to-diameter (aspect) ratio of 7.59, as in these experiments, should be sufficient to produce an image charge nearly equal to the actual droplet charge. As discussed by Weinheimer [31], the longer the tube, the larger the fraction of field lines intersected, and hence the closer the image charge will match the actual charge. This sensitivity is most noticeable for tubes with too small an aspect ratio (e.g. more “ring-like”) for which case the ratio of induced to actual charge will deviate significantly from a value of unity.

Having investigated the effect of sensor tube aspect ratio and droplet trajectory on the induced charge, it is now considered what effect of the amplifier circuit has on the

induced charge. If a sensor tube cylinder is isolated from ground, the potential of the cylinder is q'/C while the droplet remains inside, where C is the capacitance between cylinder and ground. However the sensor tube is connected to the ground through a resistor R_1 , which will include the resistance of the amplifier plus wiring resistance. The RC time-constant of the circuit will affect the induced charge q' recorded and must be taken into the consideration. The equivalent sensor circuit is an RC parallel circuit as shown in Figure 3.4.

A step function input was used as an input to simulate the effect of the RC circuit since the real input to the circuit from induced charge has a very similar shape to a step function. For a step input (induced charge q' is 0 when no charged droplet is inside the cylinder and equal to $-q'$ when charged droplet is inside) to an RC parallel circuit, the derivative of the input (induced potential) is an impulse function at the entrance of the tube. The capacitor in the parallel RC circuit reaches full charge very quickly because as a result of the step function input, which has an infinite slope. Ideally, the induced charge flows only through the equivalent capacitor C , charging it up with all the charge induced on the cylinder. But the parallel resistor bleeds off some charge from the input charge q' , which results in a continuous discharging of the capacitor. Thus the charge on the capacitor as a function of time is:

$$q_c = q' e^{-\frac{t}{RC}} \quad (3.3.4)$$

Eq. (3.3.4) is used to predict the effect of the RC time constant on the measured charge pulse. The closer the exponential term is to unity, the less error is introduced into

the charge measurement with the sensor-amplifier circuit. A larger RC time constant causes a longer discharging process which results in a smaller decay for a given time span.

This raises the question of how large the RC time constant should be. In order to interpret the droplet charge from the waveform, the current is integrated and the time-of-flight must be measured before the next droplet passes. The RC time constant should be short enough that the circuit is fully discharged before second droplet arriving the sensing tube.

In order to estimate the effects of RC decay on the induced charge pulse, a numerical integration was performed. Over the course of a small time step in this numerical integration, the charge on capacitor is changing in two ways. First, the charge is incremented by a change as the droplet moving along the sensor tube. At the same time, it decays as

$$q_c^{n+1} = q_c^n \exp\left[-\frac{\Delta t}{RC}\right] \quad (3.3.5)$$

A ratio of the RC time constant to the time it takes the charged particle to travel through the sensor, $R' = \frac{RC}{TOF}$ was used by Weinheimer [31] to describe the RC time constant effect on the induced charge. The decay factor, $\exp\left[-\frac{\Delta t}{RC}\right]$ in Eq. (3.3.5) is modified to convert the time step of droplet time-of-flight into steps in axial location of the droplet in the sensor in order to represent its induced charge. Eq. (3.3.5) is revised to

$$q_C^{n+1} = q_C^n \exp \left[-\frac{\Delta(z_0 / c)}{2R'} \right] \quad (3.3.6)$$

With known equivalent capacitance and resistance, the RC time constant effect on the induced charge can be determined. For the sensor used in these tests with a resistance and capacitance of $1 \times 10^6 \Omega$ and $0.148 \times 10^{-6} F$ respectively, and a length of 3.48 cm and radius of 0.229 cm, Figure 3.8 shows the effect on charge and current separately. These particular values of length and diameter are from the actual sensor tube used in tests. The value of resistance was measured from the actual RC circuit in use and the capacitance was measured between the sensor tube and the ground.

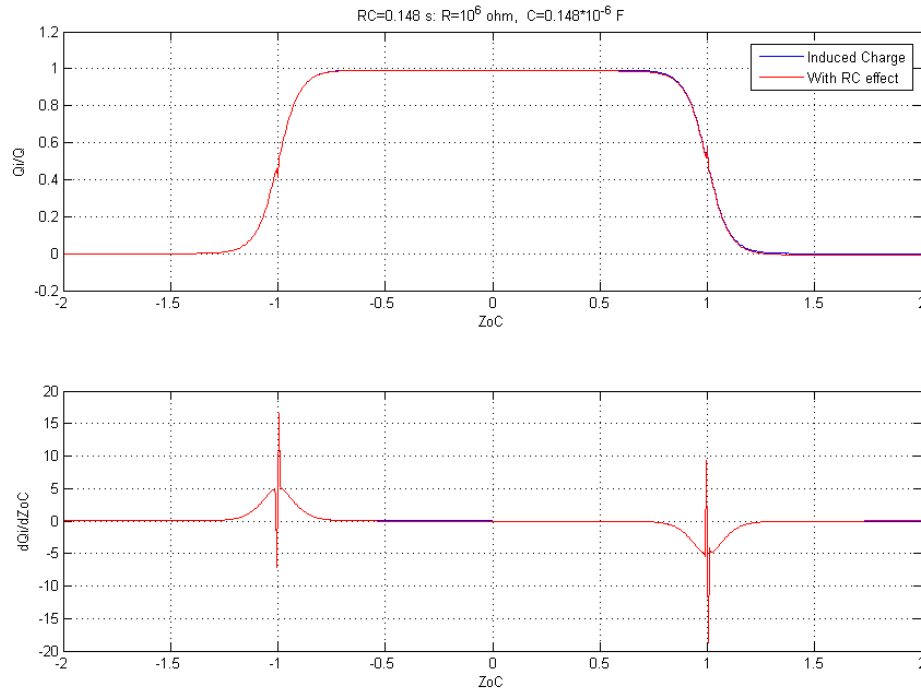


Figure 3.8 Effect of the measuring electronics on induced charge and current

The blue curve in Figure 3.8 (top) represents the ratio of induced charge to actual charge carried by a droplet traveling along the centerline axis of the sensor tube and red

curve represents the ratio of charge on the capacitor to actual charge. Because the RC time constant is much longer than droplet's time-of-flight (TOF), the most significant effect observed from the numerical result is the reduction in the pulse height that remains after passage of droplet, which is 0.65% of reduction of the height compared with the undistorted pulse (different is very small and does not show in Figure 3.8 because of the scale). For these parameters based on the RC circuit used in tests, the reduction in pulse height and the peak shift caused by RC decay are too small to be significant.

As mentioned earlier, a large RC time constant will affect the baseline (value of indicated voltage) for subsequent droplets since the voltage resulting from the slow decay of the image charge in the RC circuit will still be decreasing when a second droplet enters the sensor. A check of this effect is necessary for an RC time constant as long as 0.148 second from the circuit used in tests, compared to the time-of-flight of 0.001 second measured for the droplet generated in tests. It takes about five times the RC time constant to reach what it is considered a "full" discharge of the circuit. So the time needed to fully discharge the circuit is 0.74 seconds, which is about the same of the duration of 0.67 seconds typical of the time between the "exit" half of first wave and the "entry" half of second wave. This value corresponds to the droplet entering and exiting the sensor tube for the present experiment. The capacitor is fully discharged as the induced charge produced by the next entering droplet starts increasing.

The current with and without distortion are compared in Figure 3.8 (bottom), which indicates that the RC effect is negligible. This suggests that the electronics have a negligible effect on the charge calculated by integration of the current pulse. The voltage traces captured by oscilloscope, and integrated to calculate the charge, are negligibly

distorted. The spikes at location of $z_0/c = \pm 1$ in the curve were resulted from the “coarse” grid of z_0/c ($\Delta \frac{z_0}{c} = 0.0001$) and the limited number of x_n (10,000) chose in numerical integration. The required time for the result of numerical simulation to reach a smooth transition at location of $z_0/c = \pm 1$ with a much finer grid and more number of x_n are very long and not necessary.

3.3.3 Mechanical Construction

The mechanical design of the detector is shown in Figure 3.9 with a cutaway mechanical drawing. The primary components of the detector are the sensor head assembly which includes the collimator and retarding screen and the body tube which houses the charge sensor tube and the droplet trap. Metallic components are made of brass with the outer body consisting of a set of telescoping tubes which provide mechanical support and a grounded enclosure. The sensor head is 2.86 cm in outer diameter and 1.94 cm. The body tube is nominally 8.35 cm long and 1.67 cm in diameter. The sensor tube has an inner diameter of 0.458 cm and a length of 3.48 cm (aspect ratio of 7.6). The sensor head includes a collimating aperture with a diameter of 0.089 cm and a length of 0.635 cm. This allows for sampling of droplets within a cone of half angle 8 degrees centered about the instrument centerline axis. Droplets passing through the collimator pass through a screen which is used for the retarding potential measurement described in Section 3.3.5. Additional grounding screens can also be used if needed to shield the region near the instrument from the high potential of the retarding screen. The

retarding screen is pressed into the center segment of the detector head and held in place by a by nylon washer. Two larger nylon washers serve to provide electrical isolation for the center segment which includes the retarding screen and is biased.

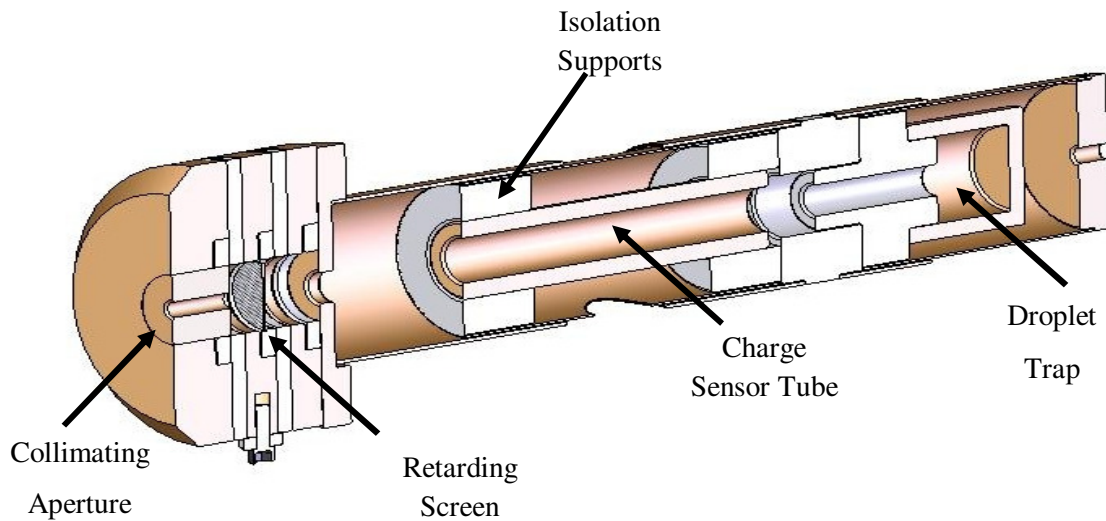


Figure 3.9 Cutaway drawing showing CDMS mechanical layout

After passing through the collimator and retarding screen, droplets travel through the sensor tube which is grounded through a resistor and connected to a high impedance amplifier circuit as described in Section 3.3.4. The charge sensor tube is supported within the grounded brass outer enclosure by Delrin support rings with a shielded lead fed through the hole in the bottom. Droplets which pass through the detector are collected in a brass cup which is supported and isolated from grounded surfaces and the sensor tube by a Delrin support. Over an extended period of operating time, droplets will accumulate

as a film in the collector cup. If needed, all detector components can be disassembled and cleaned of any accumulated residue. Because the current detector configuration relies on counting the droplets rather than current collection, this collection cup is grounded to prevent charging from droplet collection.

3.3.4 Amplifier and Data Acquisition

The amplifier circuit, shown in Figure 3.10, is similar to a design by Gamero-Castaño used in Ref. [23] and was improved and assembled by WPI undergraduate student Rosenblad [32]. The capacitor C_I in the schematic represents the capacitance of the sensor tube and associated shielded cable. A precision resistor of $1.0\text{ M}\Omega$ was used for R_I , the grounding resistor. The current induced on the detector tube by the image charge flows through the resistor creating a potential difference between the noninverting input of the LF411 operational amplifier and ground. The circuit uses a two stage amplification system. The gain of the first stage is determined by R_2 and R_3 and is on the order of 10 while the second stage is determined by R_G and is on the order of 100. The overall gain of the amplifier is determined by the product of the two stages. The overall system gain for the amplifier was measured to be 945 for these tests.

After amplification, the signal from the sensor tube amplifier is split into two separate outputs, one is used for capture of the droplet wave and the second is used for the retarding potential measurement as described in Section 3.3.5.

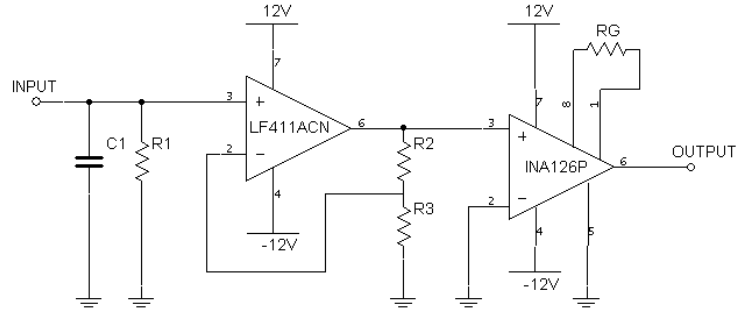


Figure 3.10 Simplified schematic of amplifier circuit [Ref. 32]

This data acquisition system was also designed and assembled by Rosenblad [32]. The droplet wave signal is fed to a Tektronix TDS3034 digital oscilloscope which is automated via a LabVIEW virtual instrument (VI) through a General Purpose Interface Bus (GPIB) port.

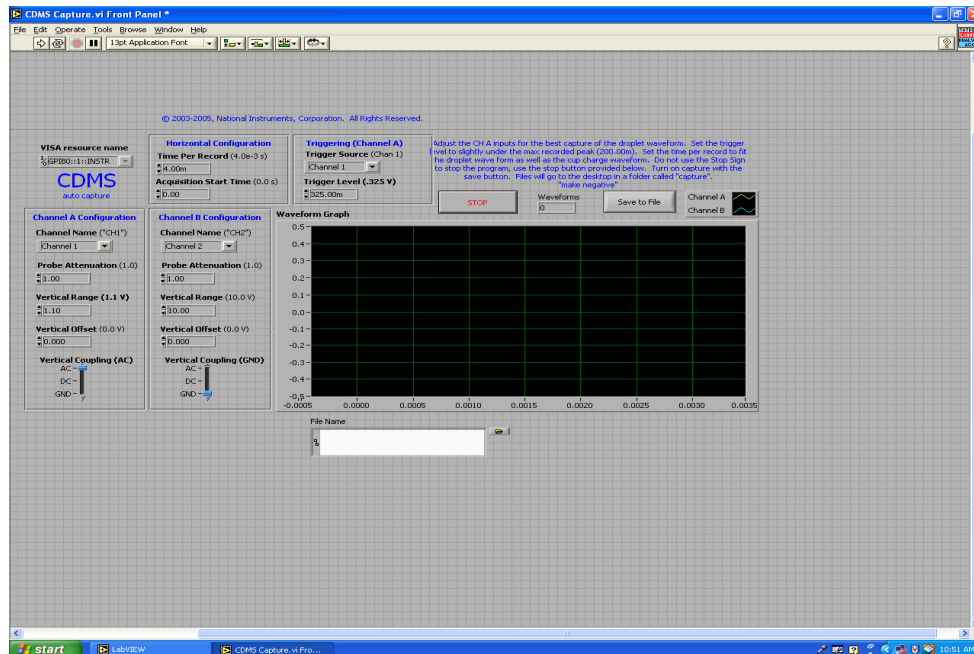


Figure 3.11 Interface of CDMS vi

A LabVIEW vi (CDMS capture vi) was made by Rosenblad [32] (see Figure 3.11) to automatically capture and record any signal present that exceeds a prescribed

threshold. A single droplet wave history consists of ten thousand data points which encompass the voltage peaks as the droplet enters and exits the sensor tube as well as some of the noise baseline. The VI automates the process of capturing the waveform and transferring the data to a PC via a GPIB interface.

3.3.5 Retarding Potential Measurement Methodology

The droplet diameter can be calculated by

$$d = \left(\frac{6}{\rho\pi} \frac{m}{q} \right)^{\frac{1}{3}} \quad (3.3.7)$$

where the droplet charge q and charge-to-mass ratio $\frac{q}{m}$ are unknowns. The charge of the droplet is the average of the area under each peak calculated by integrating the induced voltage trace of a droplet wave,

$$q = \frac{1}{2} \int_{t_i}^{t_f} \frac{|V_1(t)|}{GR_1} dt \quad (3.3.8)$$

An example of the induced voltage trace is shown conceptually in Figure 3.12. Determining the charge-to-mass ratio requires knowledge of the droplet accelerating potential and the time-of-flight, parameters determined through two independent measurements. These measurements will be described in the remainder of this section.

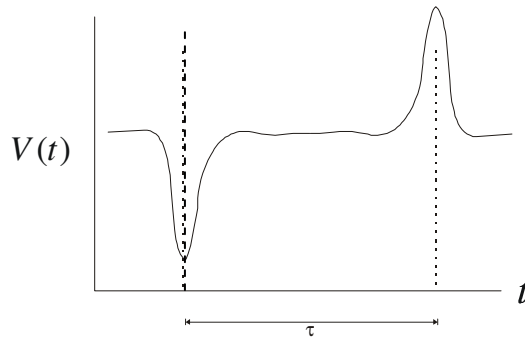


Figure 3.12 Diagram of induced voltage trace on the sensor tube indicating the time-of-flight (TOF) as the distance between pulse peaks.

The charge-to-mass ratio (specific charge) is calculated by

$$\frac{q}{m} = \frac{1}{2V_{acc}} \left(\frac{L}{\tau} \right)^2 \quad (3.3.9)$$

Where L is the length of the sensor tube and τ is the time-of-flight of droplet. With a known accelerating potential V_{acc} , Eq. (3.3.9) can be solved for specific charge.

In Section 1.5, it was briefly discussed the accelerating potential for an electrospray which is described by Gamero-Castaño [22]. Differing somewhat from the setup described in [22], a biased retarding screen was used to measure the “stopping potential curve”, while the needle voltage V_n was maintained the same. Figure 3.13 shows an idealized potential distribution along a droplet path from the needle to the retarding screen.

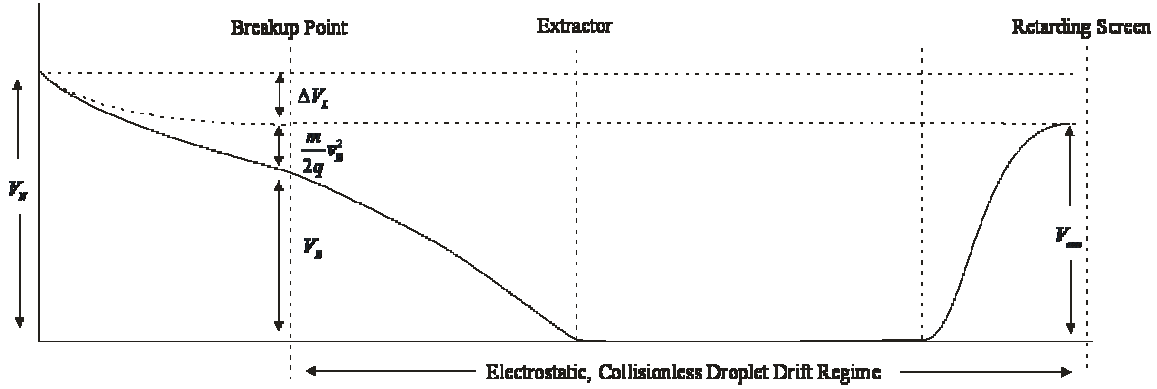


Figure 3.13 Acceleration Potential Mechanism Scheme

The accelerating potential is described by [22]

$$V_{acc} = (V_n - \Delta V_L) = V + \frac{1}{2} \frac{m}{q} v_d^2 \quad (3.3.10)$$

Where ΔV_L represents the irreversible losses in the process of jet formation prior to breakup. The accelerating potential V_{acc} is defined as the potential to which the retarding electrode must be decreased relative to the ground to repel the negatively charged droplets such that the droplet velocity reaches zero at the surface of the retarding screen. For the droplets with different sizes, there will be a distribution of accelerating potentials because different sized droplets carry different charges and will require different accelerating potentials to stop their movement at the retarding screen.

To determine the accelerating potential, a retarding screen, which can be biased, is located at the entrance of the detector tube as shown in Figure 3.9. By sweeping the retarding voltage from zero to more negative values continuously (for negatively charged droplets), the droplets are gradually repelled by the negatively increased voltage and less droplets can fly into the detector tube. Eventually all the droplets are stopped at the

entrance of the tube. The specific accelerating potentials can be determined for different sized droplets from the stopping-potential curve, which is the stopping potential (retarding potential) versus the frequency of the droplets reaching the retarding screen.

For the purpose of illustration, Figure 3.14 shows a sample plot of a stopping-potential curve plotted for the data collected in of the tests (which will be described in detail in the next chapter). The retarding voltage was decreased from 0 volt to -1900 volts (“ramp down” case) then increased back to 0 volts (“ramp up” case) with an increment, or voltage step, of -50 volts and +50 volts respectively, as shown on the x-axis. At every voltage step, the voltage was held for dwell time of 30 seconds (except for a 5 minute period for the point at 0 V). The number of droplets that pass through the tube at a particular voltage over the specified dwell time are counted. This count is used to calculate an arrival frequency at that voltage step, which is then plotted on the y-axis. This methodology allows for greater sensitivity than would be possible if an average current were being recorded using an electrometer.

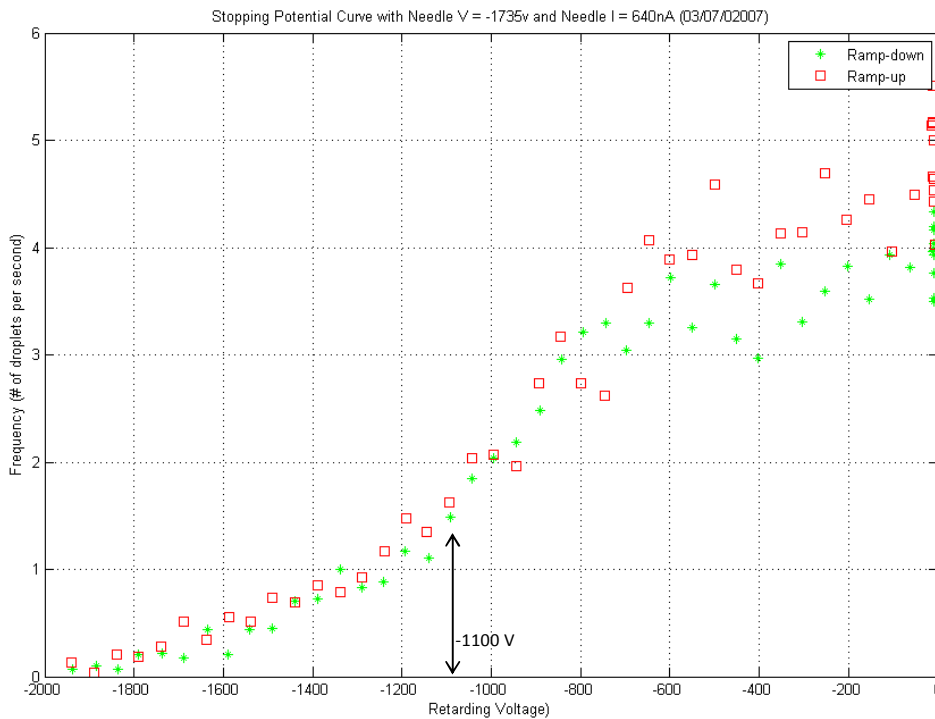


Figure 3.14 Stopping (retarding) potential curve

The retarding potential sweep data recorded by the TCAC LabVIEW vi are numerically processed by a MATLAB program, which is shown in Appendix B.2. The stopping potential curve for each set of sweep data is plotted out by the program and the average accelerating potential for each droplet population is calculated. As noted earlier, the number of droplets passing through the tube is counted at every voltage step (over the dwell time duration) by the TCAC vi program. These counts are then divided by dwell time duration and used to calculate an average (over the dwell time) droplet arrival frequency at each retarding voltage. The dwell time duration for different portions of the stopping potential curve is determined by the time difference between start and end points of a particular voltage set point instead of a fixed value for the dwell time since the actual dwell time could be different from the set value, which makes the frequency

calculation more accurate. This process is used for plotting out stopping potential curves for cases where the voltage is ramping up as well as ramping down. The retarding screen voltage is always referenced to facility ground, regardless of whether the voltage was being ramped up or down. As discussed earlier in Section 1.5, see Figure 1.12 (from Ref [22]), the number steps or “plateaus” shown in the stopping potential curve indicates the number of the droplet populations present, i.e. “one step” indicates the existence of one population of droplets. The center of the sloping region of the curve is taken to correspond to the average value of the retarding potential for this population. In Figure 3.14, there is only one step shown in each case (ramp up and down) indicating that only one population of droplets existed. The average of the center values for the two cases is taken as the accelerating voltage for this droplet population. For a clean and smooth data curve as the one shown in Figure 3.14, one can see that the average accelerating potential V_{acc} is about -1100 volts. To improve the repeatability of our measurements a curve fit was used to provide smoother estimate of the stopping potential curve. The discrete data points are fit by a 6th polynomial fitting curve so that the first derivative can be applied to the stopping potential curve to calculate the center value of the slope. V_{acc} is then determined by the minimum value of first derivative of the fitting curve as shown in Figure 4.9 in Section 4.2. For a noisy data set as shown in Figure 4.4, a 5-step moving average method is used to smooth the data, which improves the quality of the “first derivative” used to calculate the center of the slope. For droplets after electron bombardment, the accelerating potential for smaller droplets was estimated by visual inspection. For larger droplets, the “first derivative” method was applied to the stopping potential curves with a 5-step moving average used to smooth the curves to better

estimate V_{acc} . This was done for stopping potential curves having more than one step because the “moving average” alters the curve slope in the region corresponding to the smaller values of V_{acc} more severely than it does in the region corresponding to the larger values of V_{acc} . As stated earlier, the center of the sloping region of the curve is taken to correspond to the average value of the accelerating potential V_{acc} for a particular population. This can be determined either by the minimum value of first derivative, or by visual inspection to identify the center of the sloping region. Because the “first derivative” method altered the slope, thereby producing incorrect values of V_{acc} , an estimate of V_{acc} based on visual inspection of the original data was used for the smaller droplet (smaller V_{acc}) population.

It is notable that the value of V_{acc} for droplets after electron bombardment was larger compared with the value for droplets in the same size range but before electron bombardment. For example, the accelerating potential was increased from -1700 V to -1850 V after electron bombardment for test on April 05, 2011. To check the validity of this accelerating potential value, a simple calculation was performed using Taflin’s data [14]. For the sake of simplicity in what follows, it is assumed that the droplets only experience one fission event. For convenience, a constant “ C_1 ” is defined as

$$C_1 = \frac{1}{2} \left(\frac{L}{\tau} \right)^2 . \text{ Eq. (3.3.9) can then be written as}$$

$$V_{acc} = C_1 \frac{m}{q} \tag{3.3.11}$$

so that the sensitivity of the accelerating potential to changes in the droplet mass or charge can be written as

$$dV_{acc} = \frac{C_1}{q} dm - \frac{C_1 m}{q^2} dq \quad (3.3.12)$$

Equation (3.3.12) can be rearranged to get an expression for the relative change in the accelerating potential

$$\frac{dV_{acc}}{V_{acc}} = \frac{dm}{m} - \frac{dq}{q} \quad (3.3.13)$$

Substituting representative values [14] of fractional mass loss and charge loss

$\frac{dm}{m} = 0.023$ and $\frac{dq}{q} = 0.18$ into Eq. (3.3.13), it is found that $dV_{acc} \approx 0.16V_{acc}$, which

indicates that the accelerating potential for the parent droplet after fission should be higher. This is consistent with the results from tests.

To determine the droplet charge-to-mass ratio $\frac{q}{m}$, Eq. (3.3.9) also requires the knowledge of droplet's time-of-flight τ , which is the time between two peaks of the droplet induced voltage trace wave (shown in Figure 3.12). Droplet induced voltage trace recorded by CDMS Capture LabVIEW vi program are numerically processed by a MATLAB program, which is shown in Appendix B.1. The time points at that two peaks occurs are determined as “tnp” and “tpp” first and the corresponding voltages “ V_{min} ” and “ V_{max} ” are used to recognize whether the trace wave is a “noise” or a “real” wave. An average value of noise ± 0.07 V is used. Wave with $V_{max} > 0.07$ V and $V_{min} < -0.07$ V are considered “real” and the time difference between “tnp” and “tpp” is the time-of-flight τ for that specific droplet.

3.4 Droplet Charging Apparatus

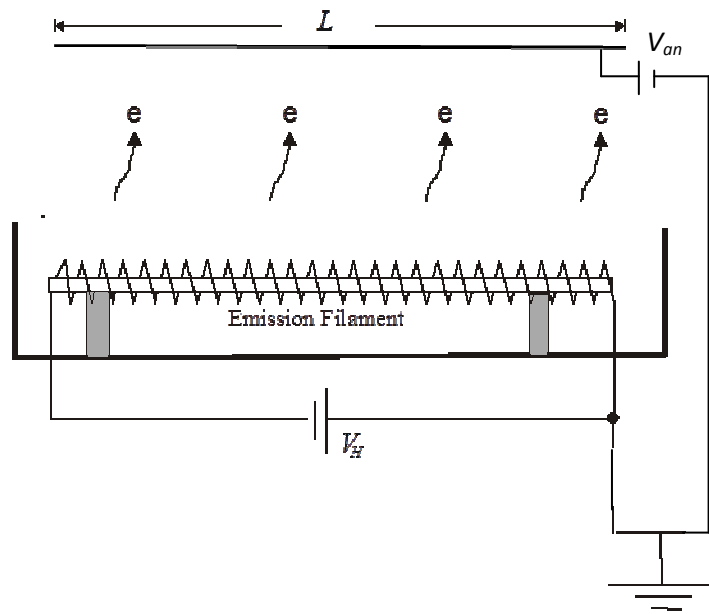


Figure 3.15 Diagram of thermionic cathode with accelerating anode plate

A conventional thermionic emission process is used to generate electrons which can then be accelerated through a potential difference using a separate controlled accelerating anode plate as shown in Figure 3.15. In this device, the power supply indicated by V_H is used to sustain a current through the filament sufficient to produce thermionic emission. The power supply indicated by V_{an} is that applied to the Anode plate for electron acceleration. The anode plate is approximately 10 - 12 cm above the filament. V_{an} determines the kinetic energy of the electrons which are at ground potential after they leave the filament. As discussed in Section 2.2, electrons are accelerated by V_{an} to a sufficient energy to overcome the electric potential barrier of the negatively charged droplets and then be captured. This arrangement allows the electron density and energy to be adjusted independently by controlling V_H and V_{an} respectively. Figure 3.16 and 3.17

show the original CAD drawing of the thermionic cathode setup with CDMS sensor tube and the picture of the apparatus. The anode plate with the top cover of the electron box was removed in Figure 3.17 so that the picture can show most part of the setup. The enclosure of the thermionic cathode with mesh grid was removed in later tests for a better electron emission result.

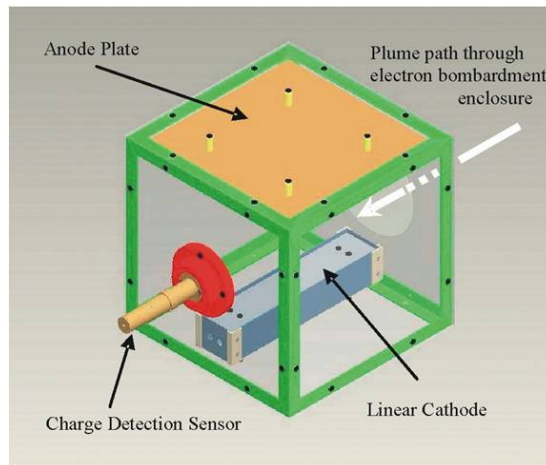


Figure 3.16 CAD drawing of CDMS/Thermionic cathode with anode plate

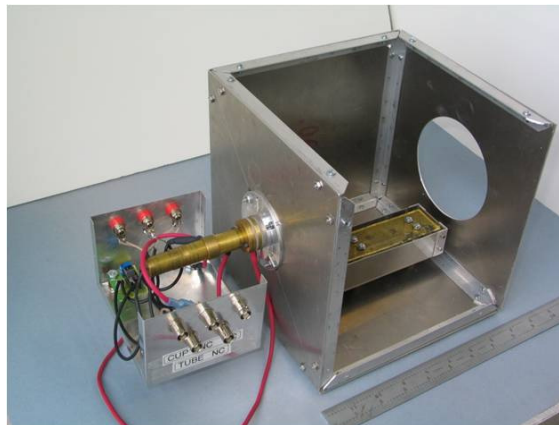


Figure 3.17 Picture of CDMS/Thermionic cathode without anode plate

Chapter 4 Results

4.1 Introduction

To investigate the effect of electron bombardment on the droplet size distribution, tests were conducted to generate an electrospray with and without electron bombardment. Droplet evaporation was neglected based on the low vapor pressure for the fluid used. The liquid (“EMI-Im” in TBP) used has a very low vapor pressure (negligible for EMI-Im [33], 0.006 Torr at 293 K and 7.5 Torr at 417 K for TBP [34]). Tests were run using the same conditions for chamber pressure, fluid flow rate, needle voltage and the trigger voltage used for wave capture. The magnitude of the electron flux could be changed for each case by adjusting the heater current and/or voltage applied to the filament. This provided a means to study the sensitivity of the droplet size to the filament emission density. Ideally, the filament emission current should have been the independent variable used to define the different test cases since it describes the electron flux precisely. However, the filament emission capability was found to vary somewhat with each use even when the same filament was used and hence should have had the same resistance. This variation made reliable calculation of the emission current difficult. For electrospray plumes produced with the same fluid and under the same test conditions, it was assumed that test-to-test variation in the *fraction* of the electron flux intercepted by the droplets was negligible. This assumption means the current collected on the anode plate I_{an} , which is easily measured, is a suitable proxy for the emission current intensity. Stated

differently, this meant that an increase of 50 percent in the anode current was assumed to correspond to a 50% increase in the cathode emission current.

The anode voltage V_{an} used to control the electron drift velocity is another important parameter for droplet size control. This voltage determines whether the electron gets sufficient kinetic energy to overcome the potential barrier of the droplet to be captured. However, V_{an} should not be so large that the droplets are attracted away from the CDMS centerline. So V_{an} should be large enough to maximum the number of the electrons reaching the droplet surface, but not so large as to deflect the droplets. To determine the value of V_{an} used in tests and also better to understand the anode current as a function of anode voltage for a given filament heater current, the current collected at the anode was measured as the anode voltage was increased continuously. Three measurements were made on filaments (Filament 1 and 2, made by high purity tungsten with 0.01 inch in diameter) by varying the power applied corresponded to three filament resistances. Electrospray was set to off, i.e. no droplets passing through. Figure 4.1 shows three anode current-voltage curves on one plot. Filament 1 and 2 were made of the same material and lengths but had been previously used for different lengths of time. The two filaments were operated individually and together, in each case up to the maximum power available from the heater supply (with 5 Amps of maximum output current). Although the power is limited, the power supply has two outputs that can provide power independently (maximum 5 Amps for each output) at the same time. So two filaments were then operated at the same time to reach a higher electron emission rate. Figure 4.1 indicates that when V_{an} is at 50 V, the collect currents I_{an} for three cases are all less than

1000 μA , which covers the required I_{an} operating range in tests. So $V_{an} = 50$ V was chosen for all the tests. Notice that filament 1 was saturated at a low voltage compared to others. This could be the affect of the contamination on the surface of the filament since filament 1 was operated for a longer time than filament 2.

A separate set of tests in which the droplets were exposed to the electron flux, and the anode voltage was increased, indicated that when V_{an} is increased to 100 V, the CDMS can hardly capture any droplets, most likely because of deflection away by the high anode voltage. So it was optimal to set $V_{an} = 50$ V for later tests. A summary of the test cases for the droplet fission tests with two electron flux control parameters V_{an} and I_{an} is listed in Table 4.1.

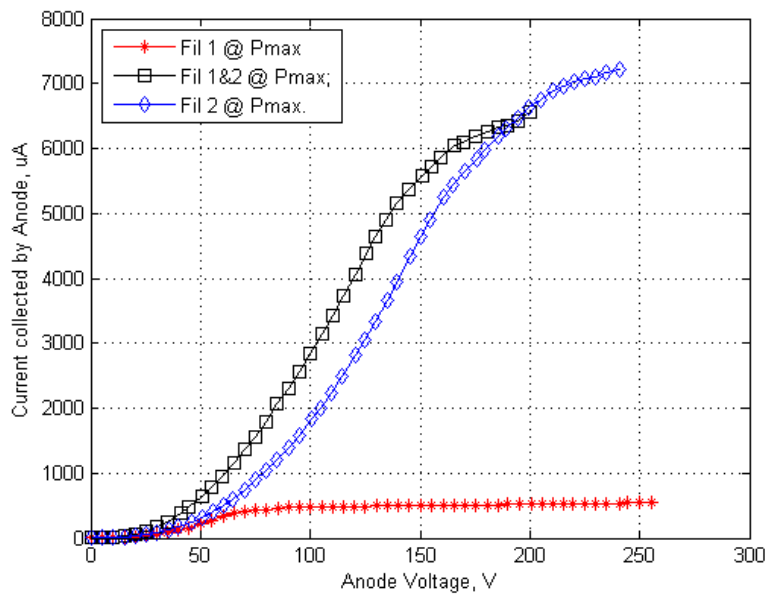


Figure 4.1 Measured anode current I_{an} as a function of anode voltage V_{an} , with no electrospray

Table 4.1 Test cases for droplet fission tests

Case	Test Condition				Comment
	V_{an} (V)	I_{an} (μ A)	V_{trig} (mV)	V_n (V)	
Base	0	0	/	/	Baseline test, with no electrons
1	200	45 \pm 10	74	-1740	Needle: SS 304, 0.00425 inch ID, 0.00925 inch OD
2	50 \pm 1	45 \pm 10	85	-2100	Needle: SS 304, 0.005 inch ID, 0.02 inch OD
3	50 \pm 1	200 \pm 25	85	-2100	
4	50 \pm 1	120 \pm 25	85	-2100	
5	50 \pm 1	45 \pm 10	-52	-2100	

Note: Different size (ID/OD) needle were used for Case 1, resulted in different V_{an} for given I_{an} and V_n . Needle/Extractor distance is the same.

The different test cases are identified with different settings of anode current I_{an} , i.e. different electron flux. The case labeled “Base” corresponds to the baseline case with no electron bombardment (i.e. cathode off). Cases 1 through 5 correspond to different electron emission currents identified by the corresponding anode current as described earlier. Anode voltage was set to approximately +50 volts to ensure the electrons were collected by the anode plate while at the same time minimizing any deflection of the negatively charged droplets. The sensitivity of anode current to anode potential and electron current emission density is discussed in Section 4.3. All the cases used the same ionic fluid mixture. Case 1 was the first “successful” case. The Case 1 test, performed with an earlier setup several years before the other cases, used a different needle with inner and outer diameters as listed in the comment column of Table 4.1. This different needle geometry resulted in the different V_{an} and V_n values listed in the table. As will be

discussed in the next section, the Case 1 results indicated a decrease in the droplet mean diameter after electron bombardment. For this reason, the Case 1 test condition was used as a reference for subsequent tests. Case 2 is basically the same test case as Case 1. Their anode currents are the same, $I_{an} = 45 \pm 10 \mu\text{A}$. To check the influence of the electron flux on the droplet size, Cases 3 and 4 used a much higher I_{an} at 200 μA and a lower I_{an} of 120 μA respectively. Case 5 attempted to duplicate same test condition as Case 2 but with a different trigger level voltage used for wave capture. The fixed test parameters are shown in Table 4.2.

Table 4.2 Fixed test parameters

Test Parameter	
Chamber Pressure	10^{-3} Torr
Fluid Conductivity	10^{-4} s/m
Fluid Flow Rate	10^{-6} cc/s

When interpreting the results, a criterion used to distinguish a “good” droplet wave from a “bad” droplet wave was defined and will be discussed in Section 4.2. Seven sets of data, chosen on the basis of this criterion, are presented. Each set of presented data includes the baseline electrospray droplet characterization (Base Case) as well as the characterization of the droplets subjected to electron flux. The results presented include the charge, the specific charge, the time-of-flight, the stopping potential curve and the size distribution. Discussion of these results is presented in Section 4.3. In Section 4.4, the uncertainty in droplet charge, specific charge and droplet diameter is discussed and estimated.

4.2 Results

In the discussion that follows, the “Case” refers to a specific set of conditions as listed in Table 4.1 and discussed in Section 4.1. The “Test” number refers to a particular test attempt (some cases were run with several attempts) for a certain Case. As shown in Table 4.3, three test attempts were conducted for Case 2, which were named as Test 1, 2 and 3 for Case 2, to re-produce the test at $I_{an} = 45 \pm 10 \mu\text{A}$. Only one test attempt was conducted for Case 1, 3, 4 and 5. Case 5 with a negative trigger voltage setting is not included in Table 4.3 for size compare because only inlet half-waves were captured. The baseline test, “Base Case”, (with filament off, no electron bombardment) was always run first before any “filament on” test. This was to make sure that results collected with and without electron emission corresponded to the same population of the droplets. Data collected for each case included the captured “droplet waves” (discussed in Section 3.3), and the stopping potential curve (discussed in Section 3.3.5).

Table 4.3 Test Results – Droplet Size Before & After Electron Bombardment

Case	Test	$I_{an} (\mu\text{A})$	Before		After			
			Droplet Diameter		Droplet Diameter 1		Droplet Diameter 2	
			$d (\mu\text{m})$	$\sigma_d (\mu\text{m})$	$d (\mu\text{m})$	$\sigma_d (\mu\text{m})$	$d (\mu\text{m})$	$\sigma_d (\mu\text{m})$
1	1	45 ± 10	5.7	1.2	-	-	3.5	0.7
2	1	45 ± 10	9.3	2.5	1.8	0.7	7.8	2.4
2	2	45 ± 10	8.3	2.2	1.4	0.6	8.9	0.2
2	3	45 ± 10	8.7	1.7	-	-	9.1	1.6
3	1	200 ± 25	9.4	1.9	-	-	9.1	1.9
4	1	120 ± 25	9.2	2.1	-	-	8.5	1.6

A typical, single-droplet wave collected by the CDMS is shown in Figure 4.2. Figure 4.3 shows a flow chart that describes the preliminary criterion used to determine whether a collected droplet wave was “good” or not. This criterion was used to filter out the “bad” waves by visual inspection of the waves. The physical significance of the two peaks for a typical wave, as shown in Figure 4.2, was described in Section 3.3. The first (inverted) peak corresponds to the induced potential from a charged droplet entering the sensor tube. The second peak is generated by the charged droplet exiting the sensor tube. Good waves are waves that have one and only one complete “inlet” and “exit” portions. Good waves also have a signal to noise ratio of 1.5, and were used as the input files for a separate MATLAB code used to calculate the charge on each droplet.

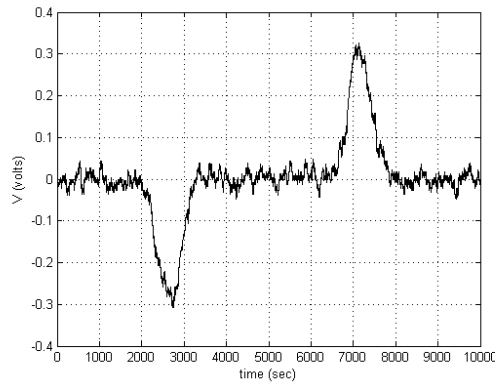


Figure 4.2 Typical wave captured by CDMS

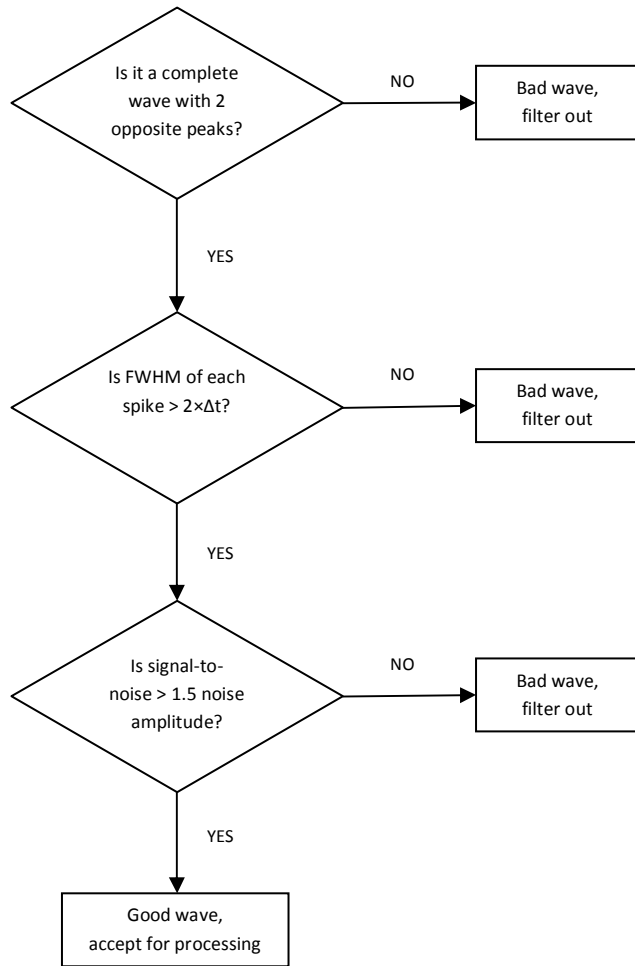


Figure 4.3 Criterion for Preliminary selection of “good” waves. ($\Delta t = 4 \times 10^{-7}$ s, which is the time step used in CDMS capture v_i showing the frequency of data capture)

The physical significance of the stopping potential and the methodology for its measurement were presented in Section 3.3.5. A typical stopping potential curve for the baseline set of parameters (Base Case) is shown in Figure 4.4. This curve was found by sweeping the voltage of retarding screen over a range of 0 V to approximately -2000 V with a -100 V voltage step and a 30 second time step. Figure 4.4 shows the raw data and a corresponding smoothed data set obtained by use of a moving average with a subset size of 5.

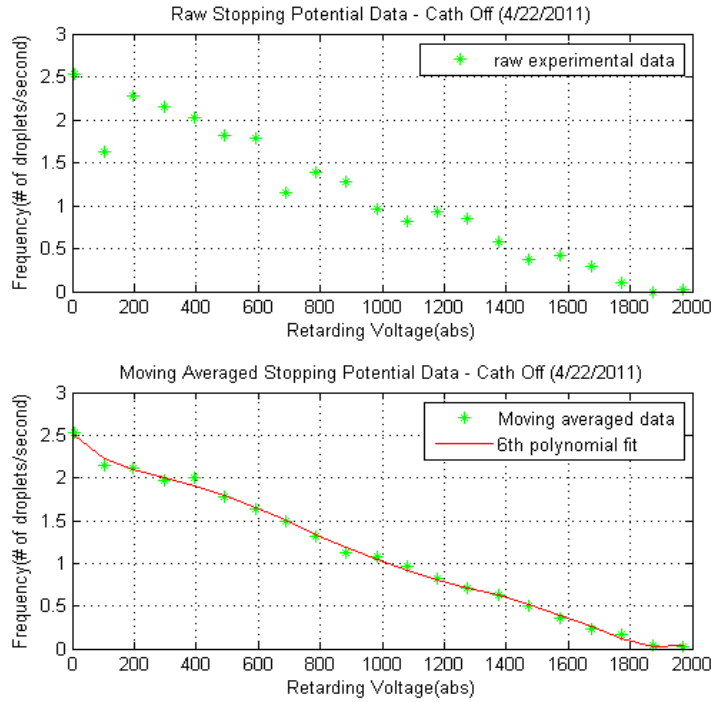


Figure 4.4 Typical baseline Droplet Stopping potential curve with a sweep range of 0 to -2000 V, with $\Delta V = -100$ V, $\Delta t = 30$ sec.

Figure 4.5 presents higher resolution stopping potential curve for the baseline (Base Case) droplets. To obtain a higher resolution stopping potential curve, the potential sweep was made with smaller (-50 V) steps and the “counting” time at each potential was increased to 600 seconds (10 minutes). Because of the time required to make this measurement, collection was divided into two separate sweeps (-400 to -1100 V and -1000 to -2000 V) made on two separate days. Another coarse potential sweep from -400 V to -2000 V with -100 V steps and the same 600 seconds counting time was measured on another day. All three measurements are shown on the same plot. This finer voltage spacing captures the frequency changes more precisely and the longer time step improves the averaging of the frequency at each voltage. Unfortunately, the finer voltage steps and

longer counting time step requires a significantly longer time to collect the entire curve, a process which was not practicable for all of the droplet fission tests since a complete test usually lasts 8-10 hours.

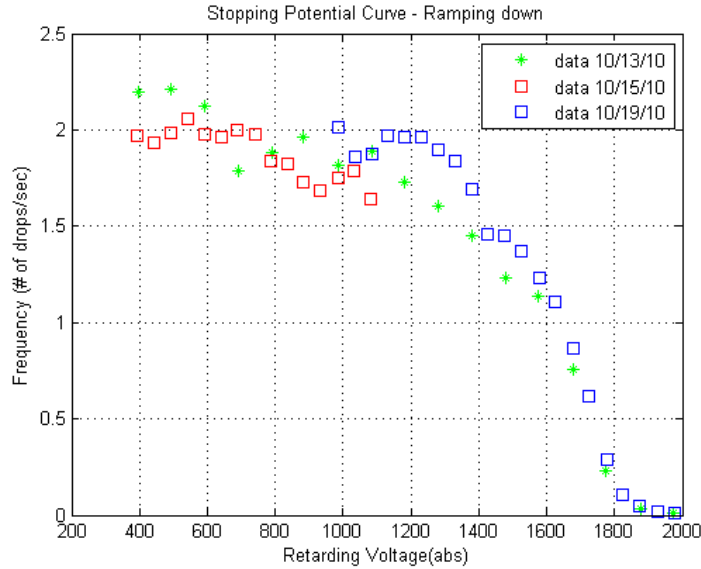


Figure 4.5 Baseline Droplet Stopping potential curve with a sweep range of -400~ -2000 V, $\Delta V = -50$ V, $\Delta t = 600$ S.

Typical CDMS waves collected for droplets which have been subjected to electron bombardment are shown in Figure 4.6. Because the effects of electron bombardment will be collective and only observable in the overall property distributions for the electro spray, the wave for an individual droplet is qualitatively identical to that of a droplet which has not been exposed to electrons (compare Figures 4.6 and 4.2). The three waves in Figure 4.2 and 4.6 were captured at the same test (Test 2 for Case 2, see Table 4.3) and are shown with the same time-volts scale for an easier comparison. They all show the same shape but have different areas under the peaks. The wave in Figure 4.2 (before electron bombardment) is taller and broader and with the signal to noise ratio of 16.3. The waves (a) and (b) in Figure 4.6 (after electron bombardment) are shorter and

narrower compared to the one in Figure 4.2 and with the signal to noise ratio of 9.3 and 5.7, respectively. This means the charge carried by the (these particular) droplets after electron bombardment was lower compared to the one before electron bombardment.

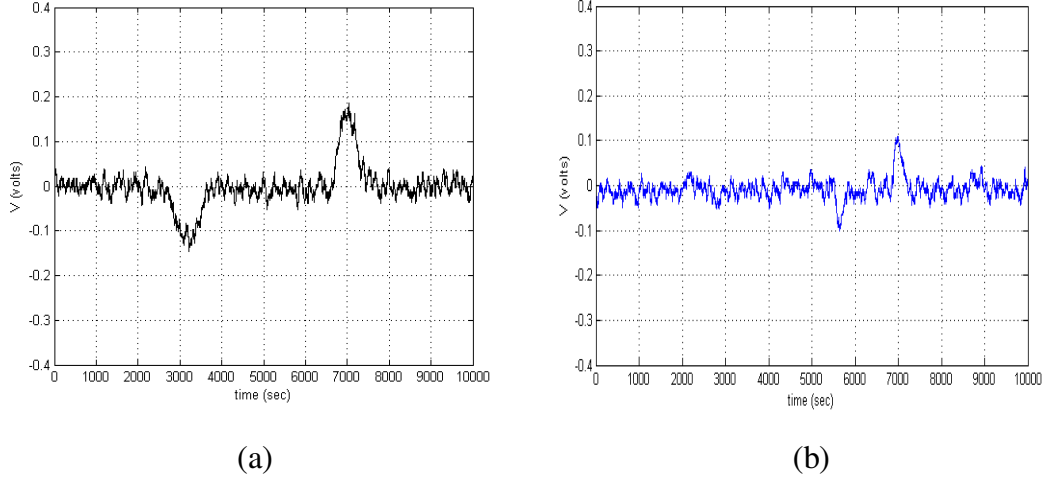


Figure 4.6 Typical waves captured by CDMS, with droplets subjected to electron flux

The criterion for initial selection of a good wave is still the same, whether the droplets are exposed to electrons or not. Wave (b) in Figure 4.6 is carrying the least charge among three droplets because it's shortest and narrowest (compare the signal to noise ratio of 5.7 with wave (a) of 9.3). The signal to noise ratio for all waves was calculated as

$$SNR = \frac{\bar{V}_p}{V_{noise_RMS}} \quad (4.2.1)$$

Where \bar{V}_p is the average potential of the two peaks and V_{noise_RMS} is the root mean square of the noise.

Figure 4.7 shows a typical stopping potential curve for droplets subjected to the electron flux. This curve, corresponding to Test 1 of Case 4, was collected by sweeping the retarding screen potential over a range of 0 to -2800 V with a -100 V voltage step and a 90 second time step. Comparing Figure 4.7 with Figures 4.4 and 4.5, the shape of the stopping potential curve clearly has two steps for the case with the electron bombardment, while the one for the baseline test has only one step. The polynomial fitting for both curves was used to find the value of V_{acc} by taking the first derivative on the fitting curve. Detailed discussion about how the stopping potential is used in the calculation is in Section 3.3.5.

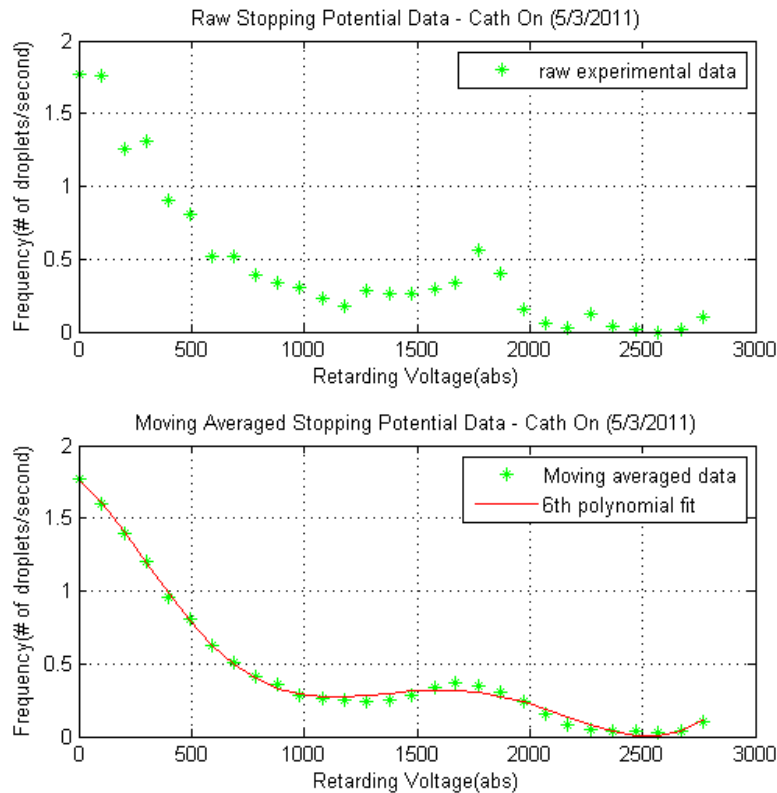
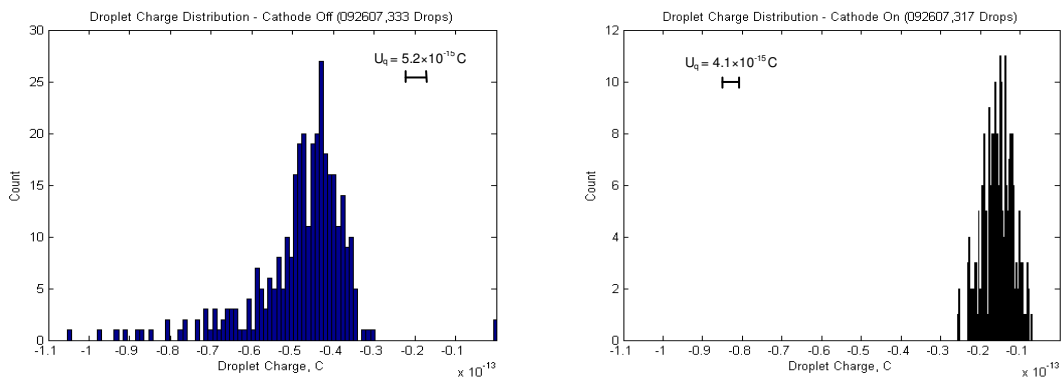


Figure 4.7 Typical stopping potential for droplets subjected to electron flux, with a sweep range of 0 to -2800 V, with $\Delta V=-100$ V, $\Delta t=90$ sec. (Test 1 of Case 4)

A set of results for Cases 1 to 5 are shown in following figures. The charge, time-of-flight, specific charge, and size distribution of droplets with and without electron bombardment are shown (and plotted with the same scale) for comparison for Case 1 to 4. The mean values, standard deviations σ for each test are shown. The uncertainties U of charge, specific charge and diameter for each case are shown on the plots and also in the captions (details are discussed in Section 4.4). For those uncertainty bars within the line thickness, only the numbers are shown on the plots. The stopping potential curves measured with and without electron bombardment are also shown. The values of stopping potential required for specific charge calculation are discussed as well. Case 5 is discussed separately for effects of trigger setting.

Results for Case 1, Test 1

Figure 4.8 - 4.9 are a complete set of results for Case 1, Test 1 (with electron flux at level of $I_{an} = 45 \pm 10 \mu A$). The results from this test clearly showed an effect from the electron bombardment with respect to charge, time-of-flight, and mean droplet size.



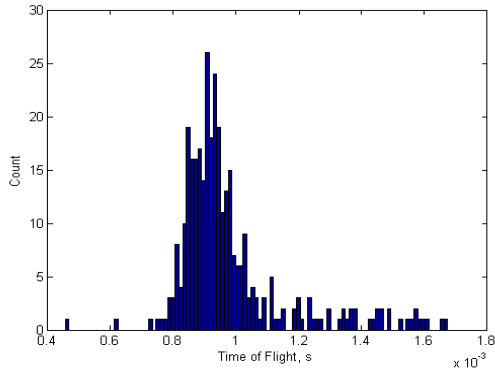
a1) Baseline Droplet charge distribution.

a2) Droplet charge distribution with cathode on.

$\langle q \rangle = -4.8 \times 10^{-14} \text{ C}; \sigma_q = 1.2 \times 10^{-14} \text{ C}; U_q = 5.2 \times 10^{-15} \text{ C}.$

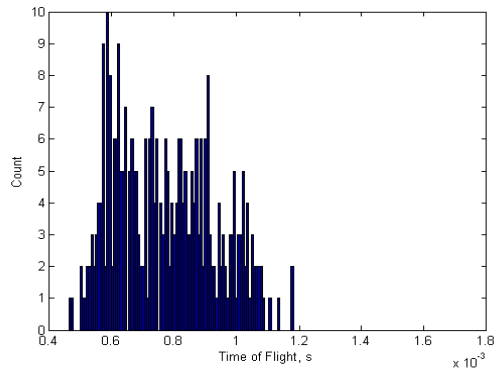
$\langle q \rangle = -1.5 \times 10^{-14} \text{ C}; \sigma_q = 0.4 \times 10^{-14} \text{ C}; U_q = 4.1 \times 10^{-15} \text{ C}.$

Figure 4.8 Results of Case 1, Test 1 (Charge)



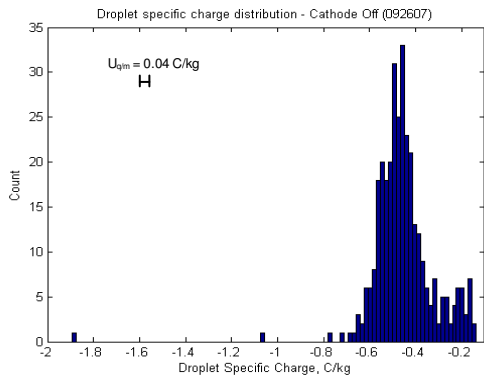
a1) Baseline Droplet time of flight distribution.

$\langle \text{TOF} \rangle = 0.98 \text{ ms}$; $\sigma_{\text{TOF}} = 0.18 \text{ ms}$.



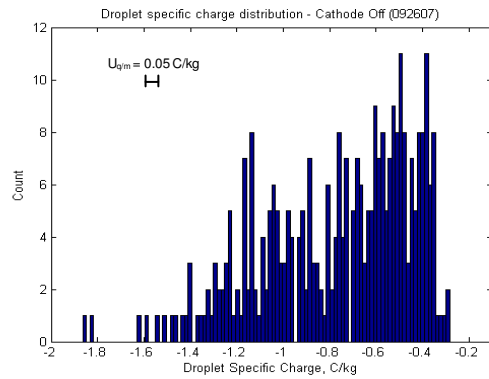
a2) Droplet time of flight distribution with cathode on.

$\langle \text{TOF} \rangle = 0.78 \text{ ms}$; $\sigma_{\text{TOF}} = 0.168 \text{ ms}$.



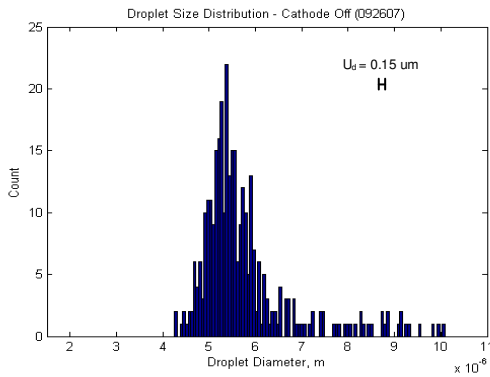
b1) Baseline Droplet specific charge distribution.

$\langle q/m \rangle = -0.53 \text{ C/kg}$; $\sigma_{q/m} = 0.16 \text{ C/kg}$; $U_{q/m} = 0.04 \text{ C/kg}$.



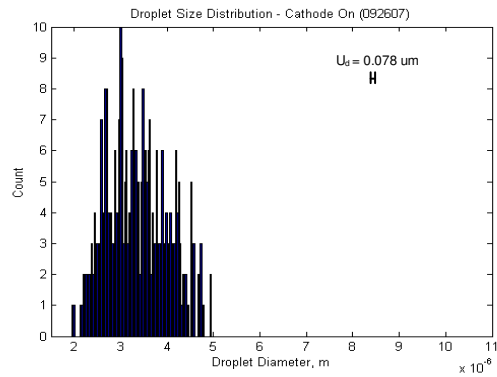
b2) Droplet specific charge distribution with cathode on.

$\langle q/m \rangle = -0.77 \text{ C/kg}$; $\sigma_{q/m} = 0.32 \text{ C/kg}$; $U_{q/m} = 0.05 \text{ C/kg}$.



c1) Baseline Droplet size distribution.

$\langle d \rangle = 5.74 \text{ }\mu\text{m}$; $\sigma_d = 1.2 \text{ }\mu\text{m}$; $U_d = 0.15 \text{ }\mu\text{m}$.



c2) Droplet size distribution with cathode on.

$\langle d \rangle = 3.5 \text{ }\mu\text{m}$; $\sigma_d = 0.7 \text{ }\mu\text{m}$; $U_d = 0.078 \text{ }\mu\text{m}$.

Figure 4.9 Results of Case 1, Test 1 (Time-of-flight, specific charge, size)

The stopping potential $V_{acc} = -1300$ V was measured for Base test of Case 1, Test 1, and used for the specific charge and size calculation as shown in Figure 4.9. Figure 4.10 a) and b) shows the baseline stopping potential curves obtained by ramping down from 0 V to -1900 V and ramping up from -1900 V to 0 V and also the corresponding first derivative curves from the polynomial fitting. V_{acc} for each ramp is -1191 V and -1390 V, respectively. The average of these two values, 1300 V, was used as a baseline V_{acc} .

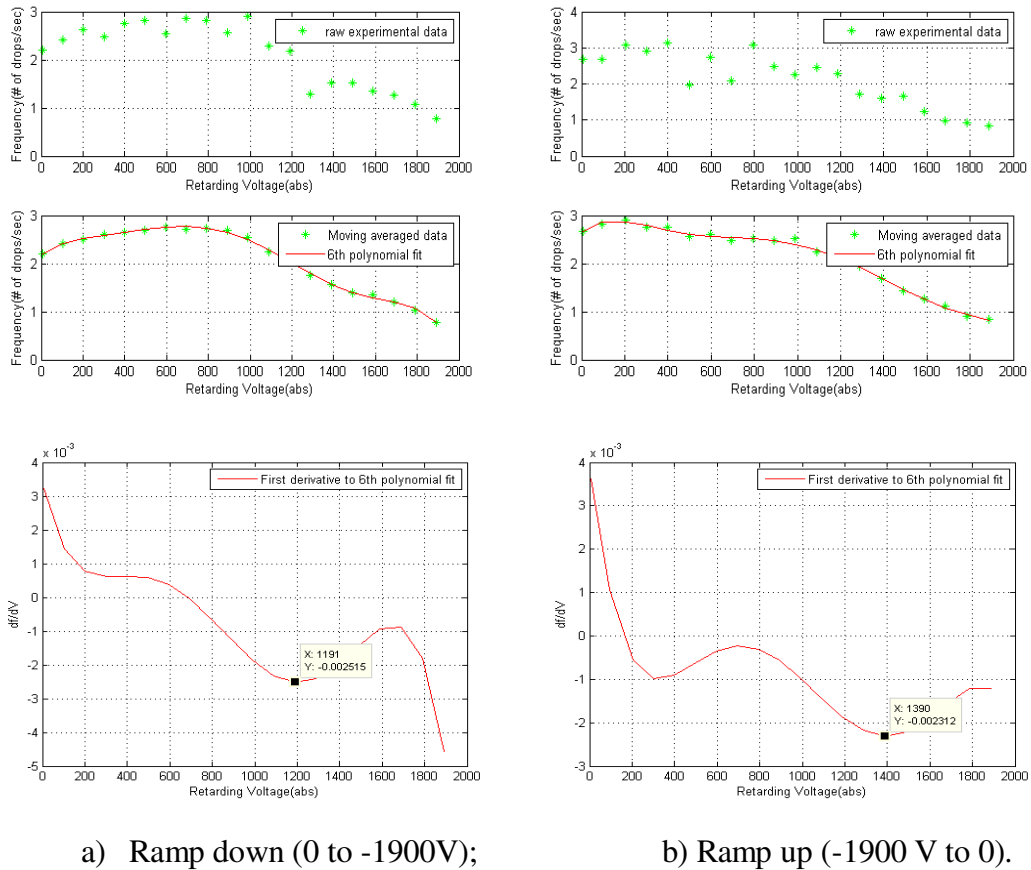
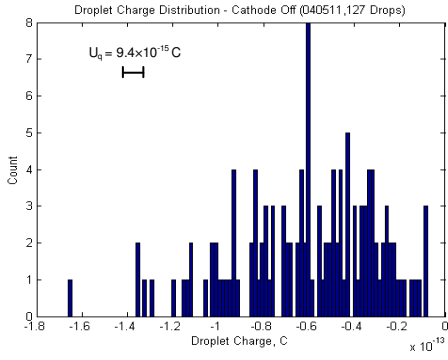


Figure 4.10 Baseline stopping potential curve for Case 1 (Test 1), $V_{acc} = -1300$ V.

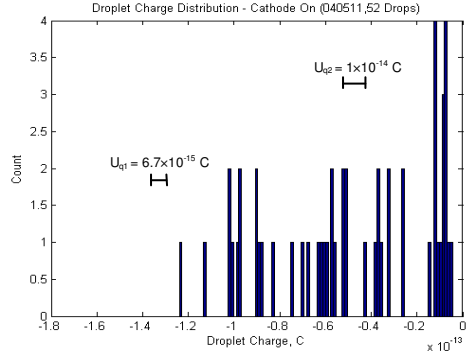
Unfortunately, for Case 1, Test 1, the stopping potential measurement for the case with cathode on failed. The droplet frequency showed no change with the stopping potential sweep from 0 V to -1900 V. But the droplet charge distribution was smaller, and the time-of-flight was shorter after the electron bombardment, these two findings strongly indicate droplet fission was occurring when the cathode was on. As discussed in Section 3.3.5, an estimate of the increase in the accelerating potential for a parent droplet after a single fission has occurred is $dV_{acc} \approx 0.16V_{acc}$. This was used to estimate the V_{acc} for the “cathode on” case based on the accelerating potential measured for the “cathode off” case: $V_{acc} = -1300 \text{ V} \times 1.16 = -1508 \text{ V}$.

Results for Case 2, Test 1

Figures 4.11 through 4.18 present the results of three tests (Test 1, 2, 3) performed using the parameters corresponding to Case 2. The anode plate current of $45 \pm 10 \mu\text{A}$ was selected to attempt to reproduce the electron emission level from Case 1. Results of Test 1 for Case 2 are shown in Figure 4.11 and 4.12 with what appear to be two populations of droplets after electron bombardment. The corresponding stopping potential curves are shown in Figure 4.13 and Figure 4.14.



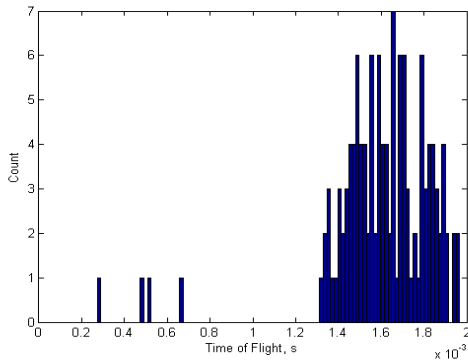
a1) Baseline Droplet charge distribution.



a2) Droplet charge distribution with cathode on.

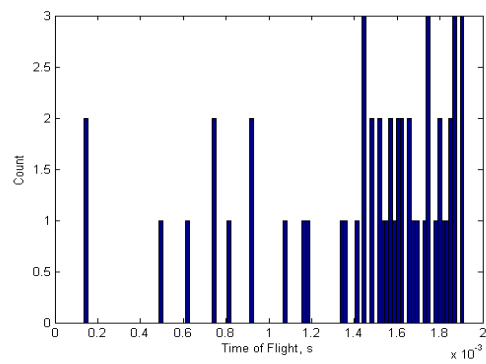
$\langle q \rangle = -6.1 \times 10^{-14} \text{ C}; \sigma_q = 3.1 \times 10^{-14} \text{ C}; U_q = 9.4 \times 10^{-15} \text{ C}.$ $\langle q_1 \rangle = -0.86 \times 10^{-14} \text{ C}; \sigma_{q_1} = 0.24 \times 10^{-14} \text{ C}; U_{q_1} = 6.7 \times 10^{-15} \text{ C}.$

$\langle q_2 \rangle = -6.16 \times 10^{-14} \text{ C}; \sigma_{q_2} = 3.1 \times 10^{-14} \text{ C}; U_{q_2} = 1 \times 10^{-14} \text{ C}.$



b1) Baseline Droplet time of flight distribution.

$\langle \text{TOF} \rangle = 1.6 \text{ ms}; \sigma_{\text{TOF}} = 0.26 \text{ ms}.$

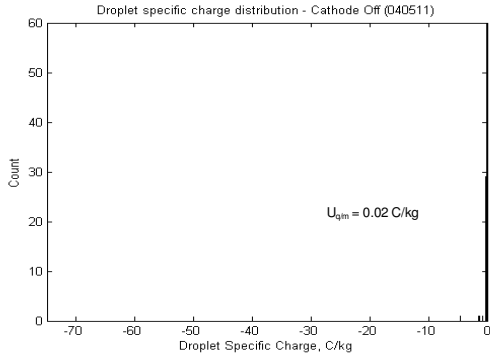


b2) Droplet time of flight distribution with cathode on.

$\langle \text{TOF}_1 \rangle = 0.75 \text{ ms}; \sigma_{\text{TOF}_1} = 0.35 \text{ ms}.$

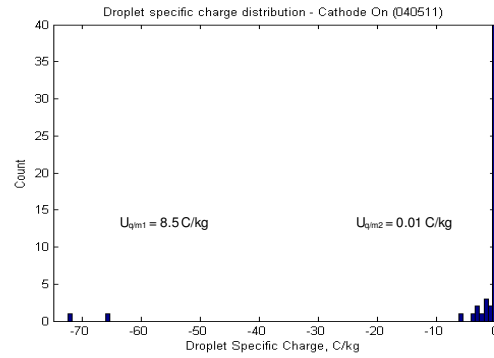
$\langle \text{TOF}_2 \rangle = 1.7 \text{ ms}; \sigma_{\text{TOF}_2} = 0.17 \text{ ms}.$

Figure 4.11 Results of Case 2, Test 1 (Charge, time-of-flight)



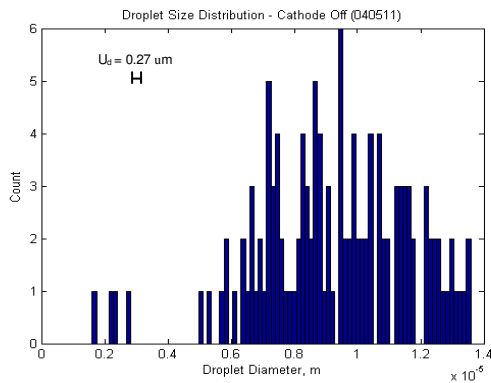
a1) Baseline Droplet specific charge distribution.

$\langle q/m \rangle = -0.20 \text{ C/kg}$; $\sigma_{q/m} = 0.42 \text{ C/kg}$; $U_{q/m} = 0.02 \text{ C/kg}$.



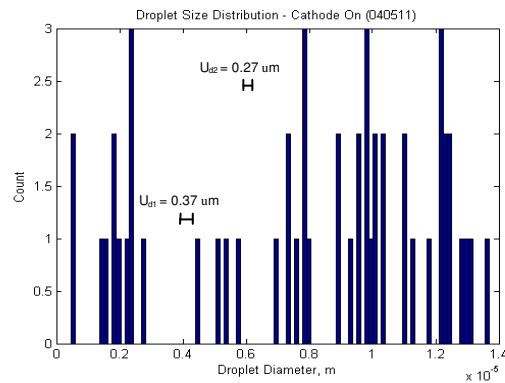
a2) Droplet specific charge distribution with cathode on.

$\langle q/m1 \rangle = -13.6 \text{ C/kg}$; $\sigma_{q/m1} = 26.0 \text{ C/kg}$; $U_{q/m1} = 8.5 \text{ C/kg}$.
 $\langle q/m2 \rangle = -0.12 \text{ C/kg}$; $\sigma_{q/m2} = 0.03 \text{ C/kg}$; $U_{q/m2} = 0.01 \text{ C/kg}$.



b1) Baseline Droplet size distribution.

$\langle d \rangle = 9.3 \text{ }\mu\text{m}$; $\sigma_d = 2.5 \text{ }\mu\text{m}$; $U_d = 0.27 \text{ }\mu\text{m}$.



b2) Droplet size distribution with cathode on.

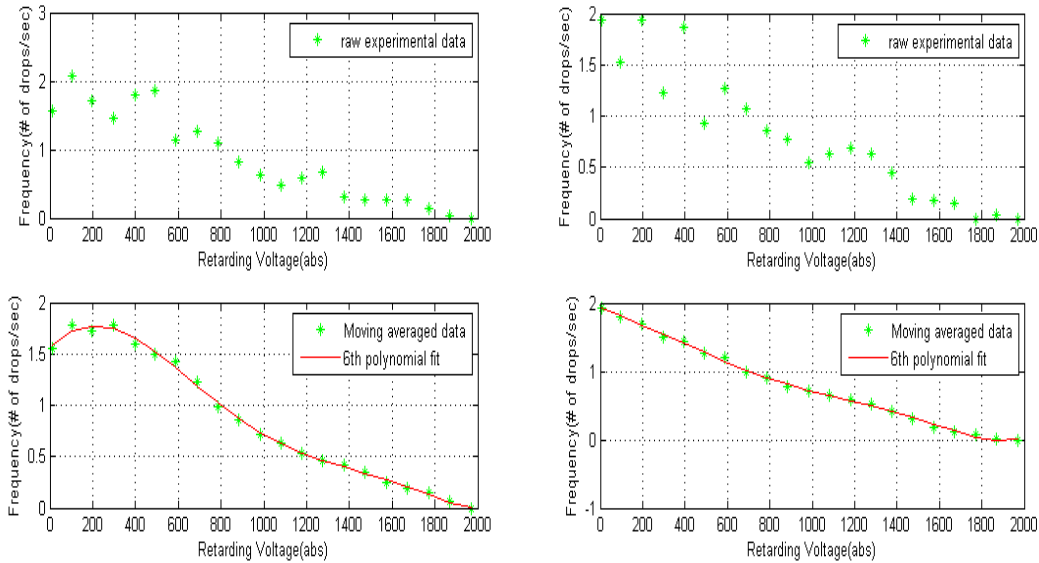
$\langle d1 \rangle = 1.8 \text{ }\mu\text{m}$; $\sigma_{d1} = 0.7 \text{ }\mu\text{m}$; $U_{d1} = 0.37 \text{ }\mu\text{m}$.
 $\langle d2 \rangle = 9.8 \text{ }\mu\text{m}$; $\sigma_{d2} = 2.4 \text{ }\mu\text{m}$; $U_{d2} = 0.27 \text{ }\mu\text{m}$.

Figure 4.12 Results of Case 2, Test 1 (Specific charge, size)

Note: a1) and a2) were plotted on the same scale to allow for direct comparison. Specific charge for a1) is difficult to resolve on this scale.

Stopping potential curves for the baseline test and test with cathode on for Test 1 of Case 2 are shown in Figure 4.13 and 4.14. For baseline tests of Cases 2, 3 and 4, the same ramping down and up potential sweeps were conducted as for Case 1 and the same technique for finding average V_{acc} was used. For tests with the cathode on for Case 1 to 4, only the ramping down sweep was conducted because the larger sweep range (0 to 2500

V) and longer counting time (90 seconds) required significantly longer time to complete. The procedure of using only a single potential sweep (ramping down) with finer resolution actually showed an improved, cleaner stopping potential curve so that collection of additional potential sweeps were not seemed necessary.



a) Potential sweep from 0 to -2000V;

b) Potential sweep from -2000V to 0 V.

Figure 4.13 Baseline Stopping potential curve for Case 2 (Test 1), $V_{acc} = -1700$ V.

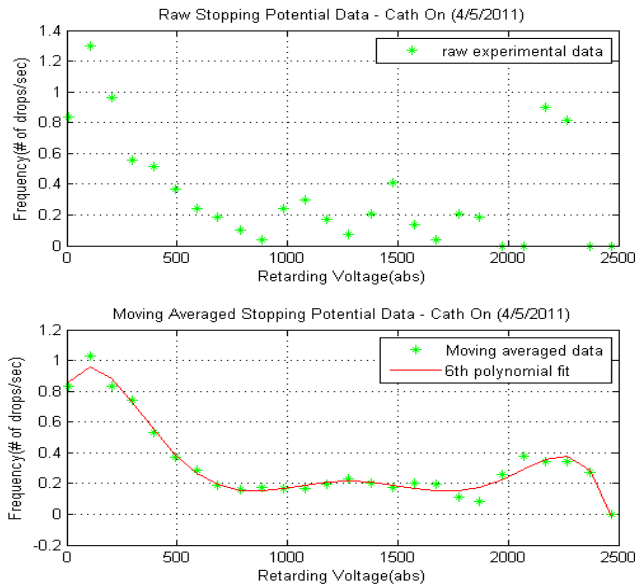
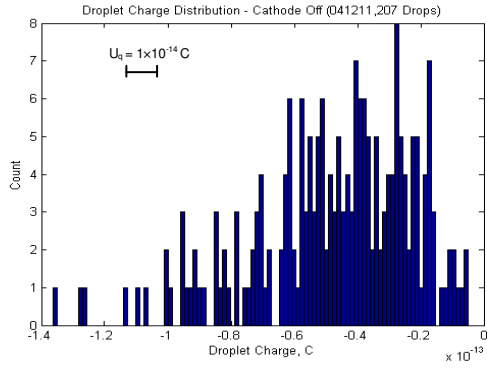


Figure 4.14 Stopping potential curve with “Cathode on” for Case 2 (Test 1) of (0 ~ -2500V), $V_{acc\ 1} = -400\text{ V}$; $V_{acc\ 2} = -1850\text{ V}$.

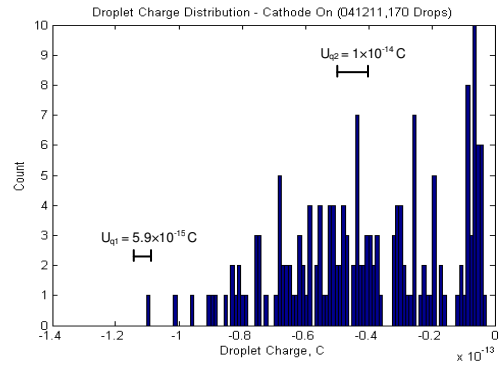
Results for Case 2, Test 2

Test 2 for Case 2, the results of which are shown in Figure 4.15 and Figure 4.16, was another attempt at reproducing the test conditions corresponding to Case 2 that showed clear evidence of two droplets populations.



a1) Baseline Droplet charge distribution.

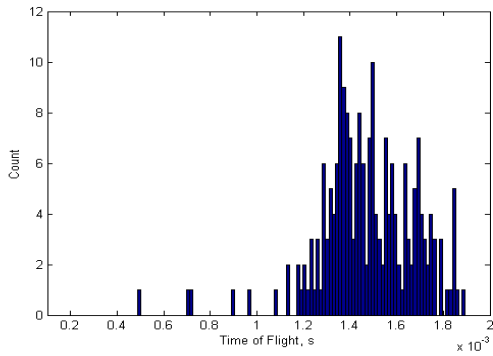
$\langle q \rangle = -4.8 \times 10^{-14} \text{ C}$; $\sigma_q = 2.58 \times 10^{-14} \text{ C}$; $U_q = 1 \times 10^{-14} \text{ C}$.



a2) Droplet charge distribution with cathode on.

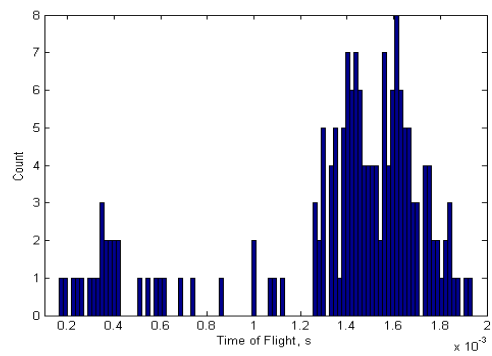
$\langle q_1 \rangle = -0.69 \times 10^{-14} \text{ C}$; $\sigma_{q_1} = 0.29 \times 10^{-14} \text{ C}$; $U_{q_1} = 5.9 \times 10^{-15} \text{ C}$.

$\langle q_2 \rangle = -4.8 \times 10^{-14} \text{ C}$; $\sigma_{q_2} = 2.2 \times 10^{-14} \text{ C}$; $U_{q_2} = 1 \times 10^{-14} \text{ C}$.



b1) Baseline Droplet time of flight distribution.

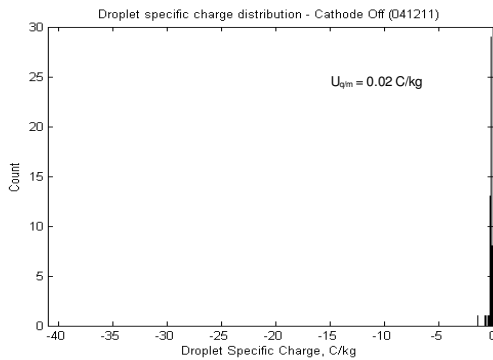
$\langle \text{TOF} \rangle = 1.5 \text{ ms}$; $\sigma_{\text{TOF}} = 0.2 \text{ ms}$.



b2) Droplet time of flight distribution with cathode on.

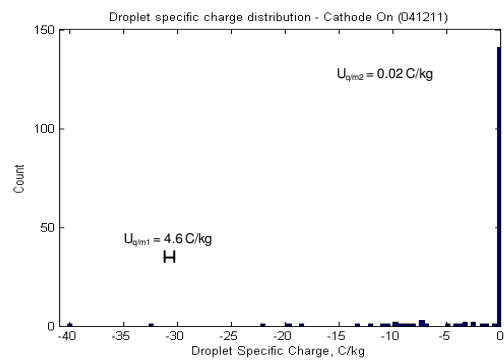
$\langle \text{TOF}_1 \rangle = 0.5 \text{ ms}$; $\sigma_{\text{TOF}_1} = 0.28 \text{ ms}$;

$\langle \text{TOF}_2 \rangle = 1.5 \text{ ms}$; $\sigma_{\text{TOF}_2} = 0.16 \text{ ms}$.



c1) Baseline Droplet specific charge distribution.

$\langle q/m \rangle = -0.17 \text{ C/kg}$; $\sigma_{q/m} = 0.10 \text{ C/kg}$; $U_{q/m} = 0.02 \text{ C/kg}$.

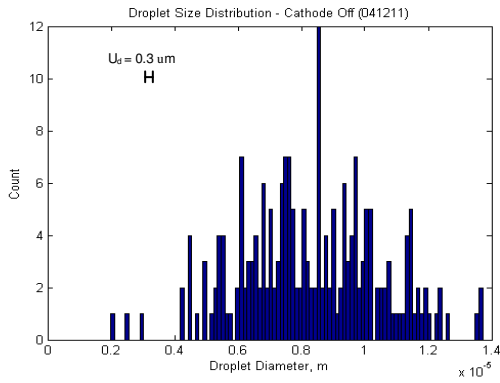


c2) Droplet specific charge distribution with cathode on.

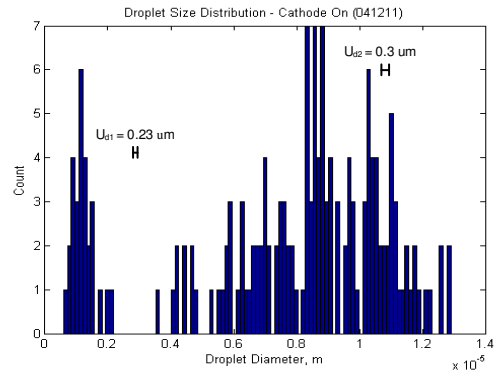
$\langle q/m_1 \rangle = -9.15 \text{ C/kg}$; $\sigma_{q/m_1} = 9.02 \text{ C/kg}$; $U_{q/m_1} = 4.6 \text{ C/kg}$.

$\langle q/m_2 \rangle = -0.13 \text{ C/kg}$; $\sigma_{q/m_2} = 0.03 \text{ C/kg}$; $U_{q/m_2} = 0.02 \text{ C/kg}$.

Figure 4.15 Results of Case 2, Test 2 (Charge, time-of-flight, specific charge)



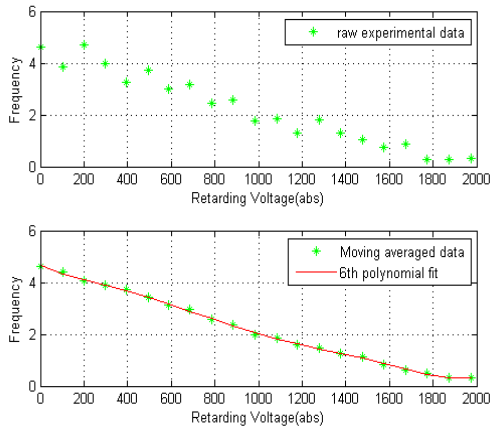
a1) Baseline Droplet size distribution.
 $\langle d \rangle = 8.3 \mu\text{m}$; $\sigma_d = 2.2 \mu\text{m}$; $U_d = 0.3 \mu\text{m}$.



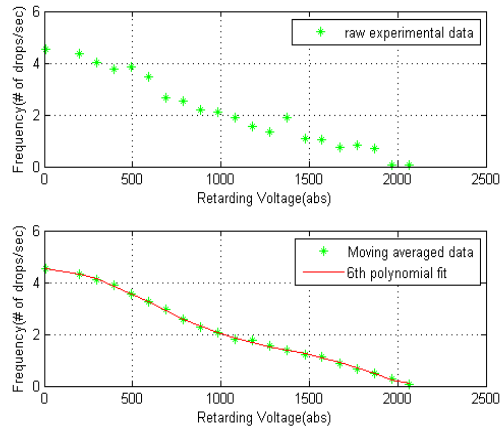
a2) Droplet size distribution with cathode on.
 $\langle d_1 \rangle = 1.4 \mu\text{m}$; $\sigma_{d_1} = 0.6 \mu\text{m}$; $U_{d_1} = 0.23 \mu\text{m}$.
 $\langle d_2 \rangle = 8.9 \mu\text{m}$; $\sigma_{d_2} = 0.2 \mu\text{m}$; $U_{d_2} = 0.3 \mu\text{m}$.

Figure 4.16 Results of Case 2, Test 2 (Size)

The stopping potential curves for the baseline test and test with cathode on for Test 2 of Case 2 are shown in Figure 4.17 and 4.18.



a) Potential sweep from 0 to -2000V;



b) sweep from -2000V to 0 V.

Figure 4.17 Baseline Stopping potential curve for Case 2 (Test 2), $V_{acc} = -1820 \text{ V}$.

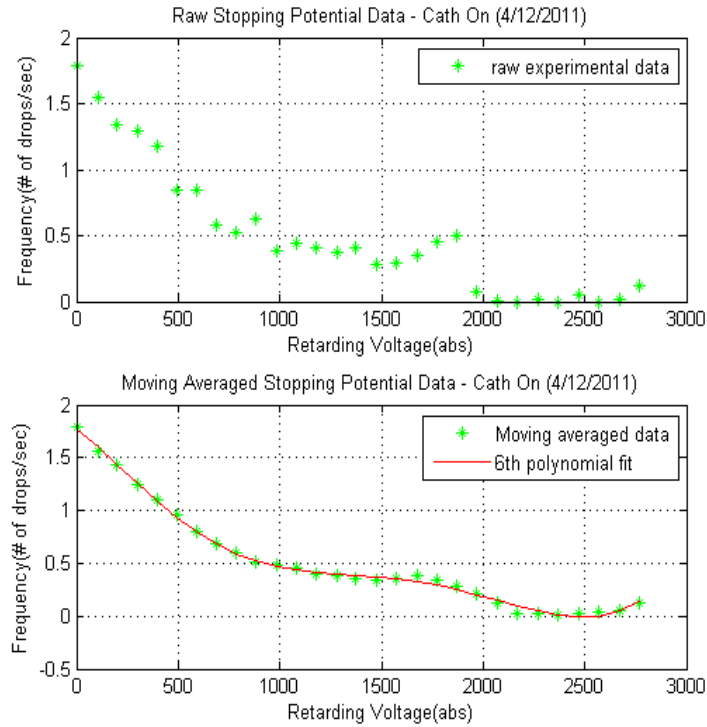
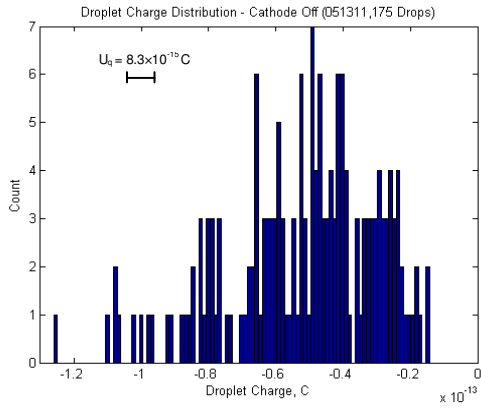


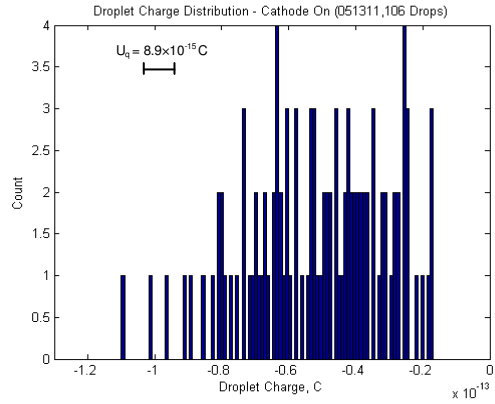
Figure 4.18 Stopping potential curve with “Cathode on” for Case 2 (Test 2) of (0 to -2800V), $V_{acc\ 1} = -500\text{ V}$; $V_{acc\ 2} = -2000\text{ V}$.

Results for Case 2, Test 3

A third test using the conditions corresponding to Case 2, the results of which are shown in Figure 4.19 and Figure 4.20, did not show the same evidence of two populations, although the stopping potential curves did show evidence of a second population.



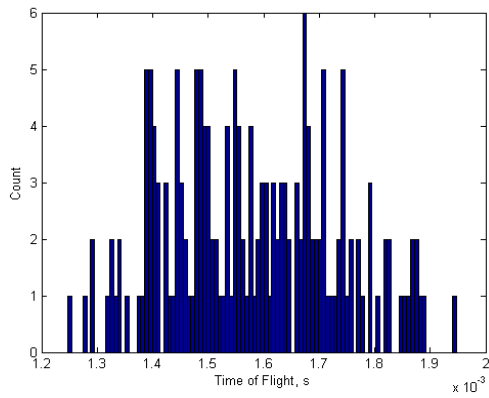
a1) Baseline Droplet charge distribution.



a2) Droplet charge distribution with cathode on.

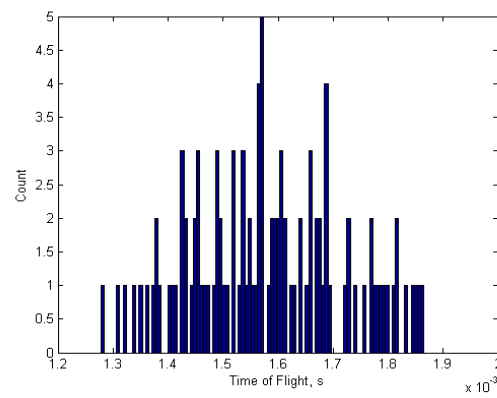
$\langle q \rangle = -5.2 \times 10^{-14} \text{ C}; \sigma_q = 2.2 \times 10^{-14} \text{ C}; U_q = 8.3 \times 10^{-15} \text{ C}.$

$\langle q \rangle = -5.1 \times 10^{-14} \text{ C}; \sigma_q = 2.0 \times 10^{-14} \text{ C}; U_q = 8.9 \times 10^{-15} \text{ C}.$



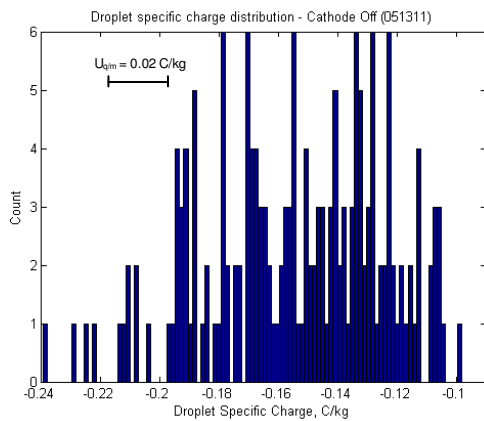
b1) Baseline Droplet time of flight distribution.

$\langle \text{TOF} \rangle = 1.6 \text{ ms}; \sigma_{\text{TOF}} = 0.15 \text{ ms}.$



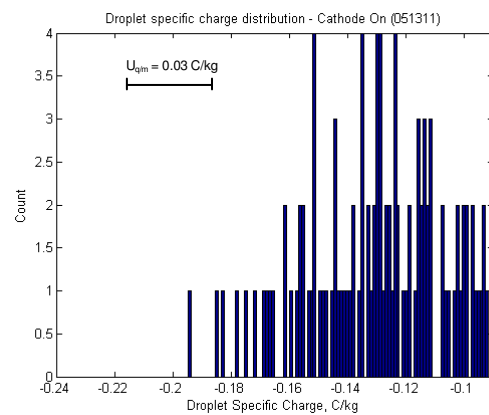
b2) Droplet time of flight distribution with cathode on.

$\langle \text{TOF} \rangle = 1.6 \text{ ms}; \sigma_{\text{TOF}} = 0.14 \text{ ms}.$



c1) Baseline Droplet specific charge distribution.

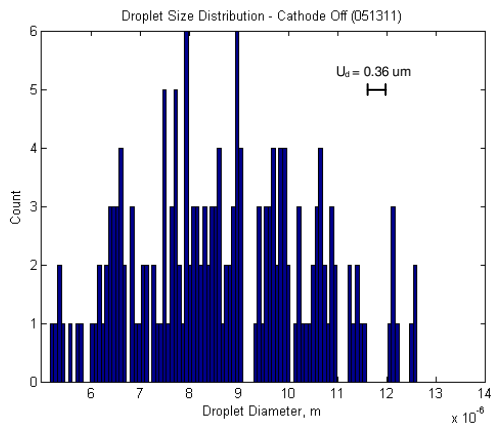
$\langle q/m \rangle = -0.15 \text{ C/kg}; \sigma_{q/m} = 0.03 \text{ C/kg}; U_{q/m} = 0.02 \text{ C/kg}.$



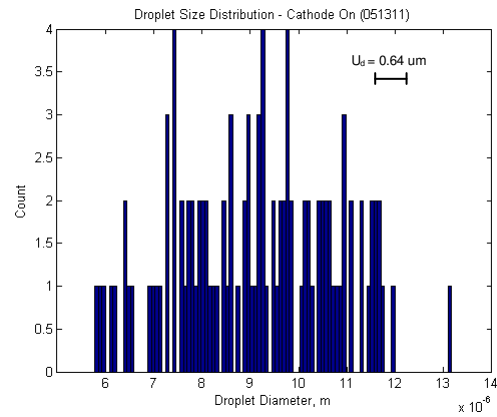
c2) Droplet specific charge distribution with cathode on.

$\langle q/m \rangle = -0.13 \text{ C/kg}; \sigma_{q/m} = 0.02 \text{ C/kg}; U_{q/m} = 0.03 \text{ C/kg}.$

Figure 4.19 Results of Case 2, Test 3 (Charge, time-of-flight, specific charge)



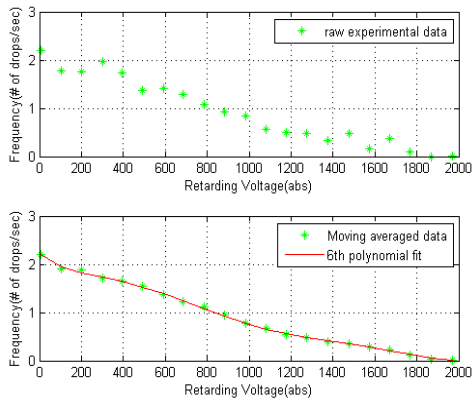
a1) Baseline Droplet size distribution.
 $\langle d \rangle = 8.7 \text{ um}$; $\sigma_d = 1.7 \text{ um}$; $U_d = 0.36 \text{ um}$.



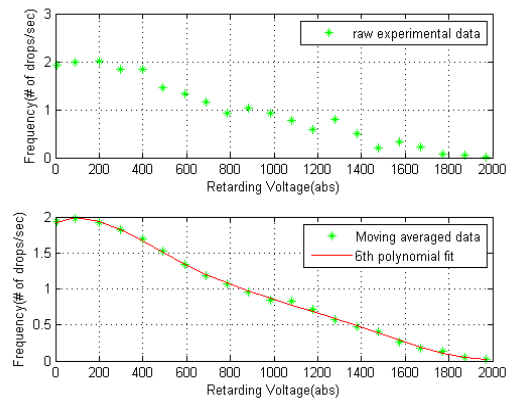
a2) Droplet size distribution with cathode on.
 $\langle d \rangle = 9.1 \text{ um}$; $\sigma_d = 1.6 \text{ um}$; $U_d = 0.64 \text{ um}$.

Figure 4.20 Results of Case 2, Test 3 (Size)

Stopping potential curves for baseline test and test with cathode on for Test 3 of Case 2 are shown in Figure 4.21 and 4.22.



a) Potential sweep from 0 to -2000V;



b) sweep from -2000V to 0 V.

Figure 4.21 Baseline Stopping potential curve for Case 2 (Test 3), $V_{acc} = -1622 \text{ V}$.

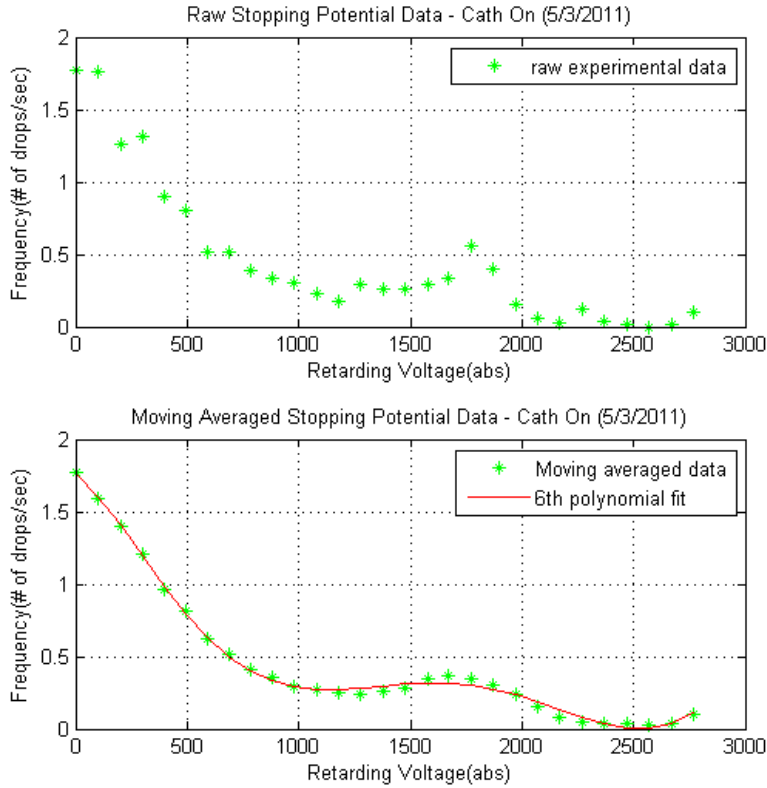
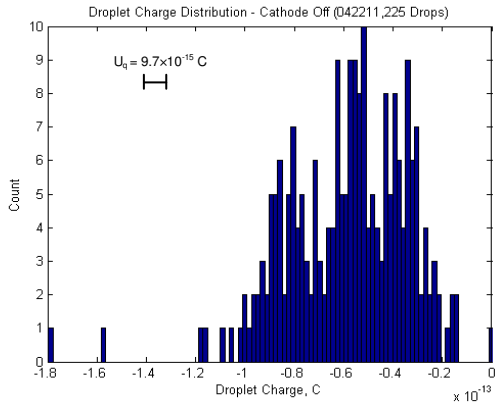


Figure 4.22 Stopping potential curve with “Cathode on” for Case 2 (Test 3) of (0 to -2800V). $V_{acc\ 1} = -450\text{ V}$; $V_{acc\ 2} = -1900\text{ V}$.

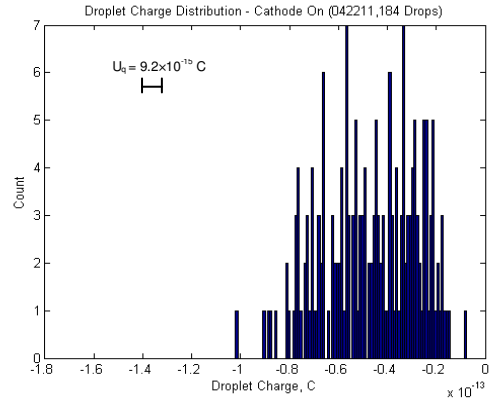
Results for Case 3, Test 1

Figure 4.23 and Figure 4.24 present the results for Case 3 (Test 1). The test parameters for Case 3 were the same as Case 2 except that collected anode current was increased to $I_{an} = 200 \pm 25\ \mu\text{A}$ to determine if the higher electron flux had a noticeable effect on the droplet size distribution.



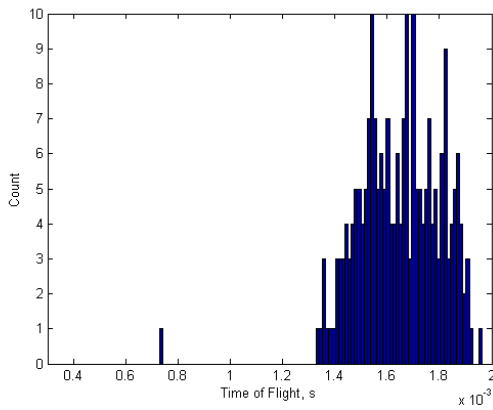
a1) Baseline Droplet charge distribution.

$$\langle q \rangle = -5.9 \times 10^{-14} \text{ C}; \sigma_q = 2.5 \times 10^{-14} \text{ C}; U_q = 9.7 \times 10^{-15} \text{ C}.$$



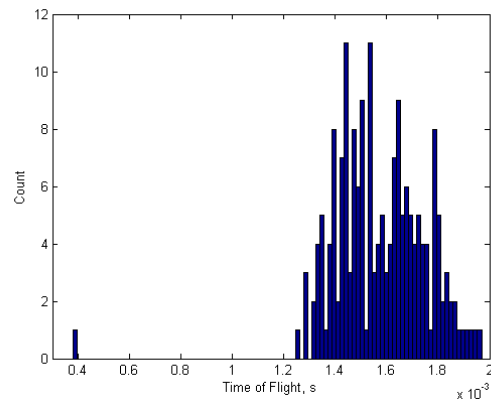
a2) Droplet charge distribution with cathode on.

$$\langle q \rangle = -4.7 \times 10^{-14} \text{ C}; \sigma_q = 1.9 \times 10^{-14} \text{ C}; U_q = 9.2 \times 10^{-15} \text{ C}.$$



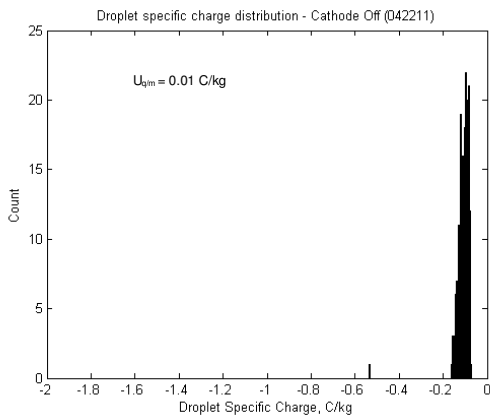
b1) Baseline Droplet time of flight distribution.

$$\langle \text{TOF} \rangle = 1.6 \text{ ms}; \sigma_{\text{TOF}} = 0.16 \text{ ms}.$$



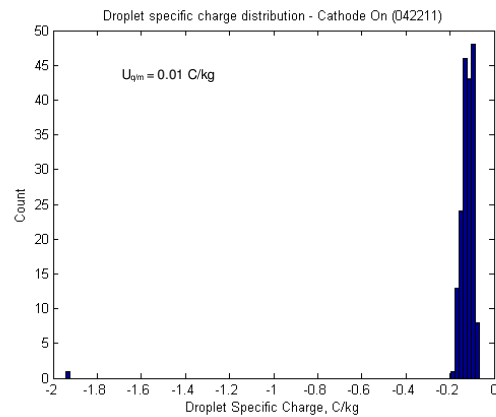
b2) Droplet time of flight distribution with cathode on.

$$\langle \text{TOF} \rangle = 1.6 \text{ ms}; \sigma_{\text{TOF}} = 0.18 \text{ ms}.$$



c1) Baseline Droplet specific charge distribution.

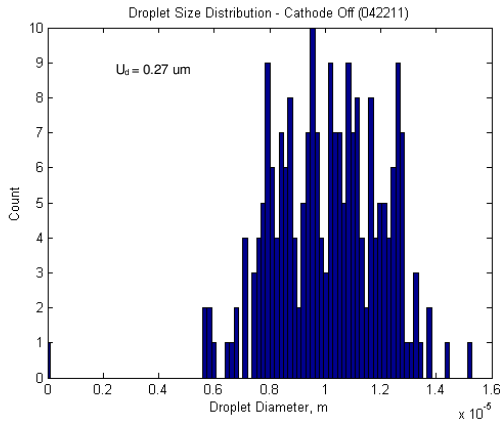
$$\langle q/m \rangle = -0.13 \text{ C/kg}; \sigma_{q/m} = 0.04 \text{ C/kg}; U_{q/m} = 0.01 \text{ C/kg}.$$



c2) Droplet specific charge distribution with cathode on.

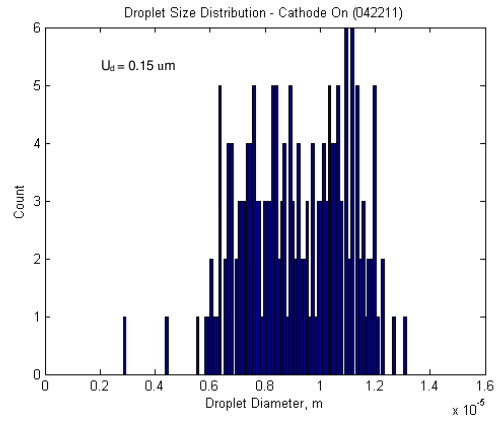
$$\langle q/m \rangle = -0.13 \text{ C/kg}; \sigma_{q/m} = 0.14 \text{ C/kg}; U_{q/m} = 0.01 \text{ C/kg}.$$

Figure 4.23 Results of Case 3, Test 1 (Charge, time-of-flight, specific charge)



a1) Baseline Droplet size distribution.

$\langle d \rangle = 9.4 \text{ um}$; $\sigma_d = 1.9 \text{ um}$; $U_d = 0.27 \text{ um}$.

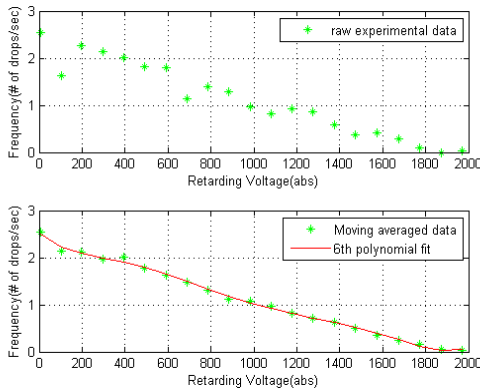


a2) Droplet size distribution with cathode on.

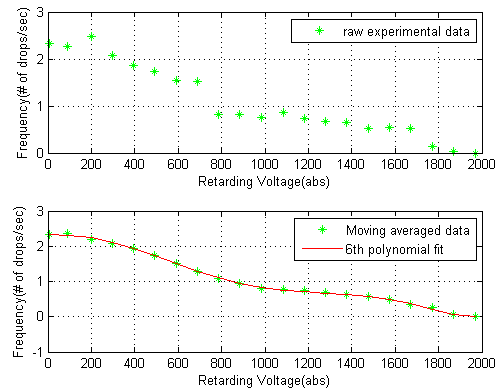
$\langle d \rangle = 9.1 \text{ um}$; $\sigma_d = 1.9 \text{ um}$; $U_d = 0.15 \text{ um}$.

Figure 4.24 Results of Case 3, Test 1 (Size)

Stopping potential curves for the baseline test and test with cathode on for Test 1 of Case 3 are shown in Figure 4.25 and 4.26.



a) Potential sweep from 0 to -2000V;



b) sweep from -2000V to 0 V.

Figure 4.25 Baseline Stopping potential curve for Case 3 (Test 1), $V_{acc} = -1723 \text{ V}$.

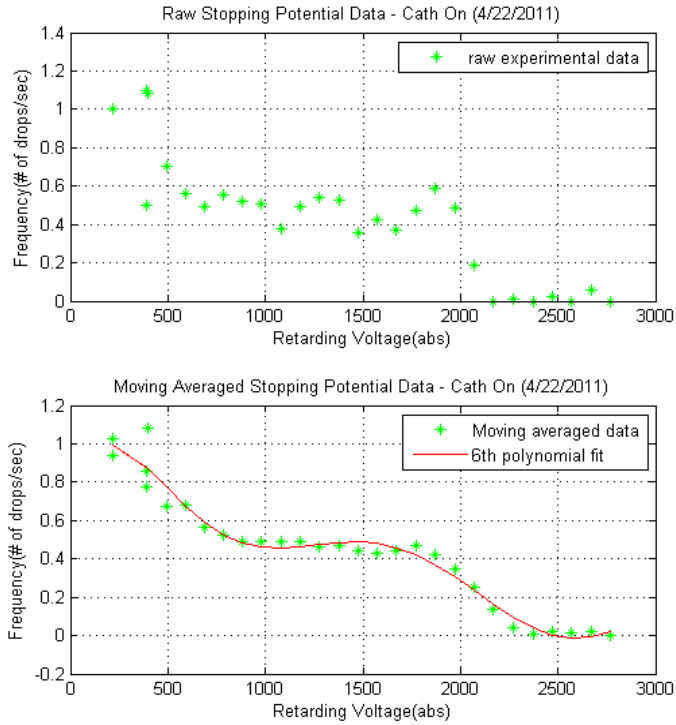
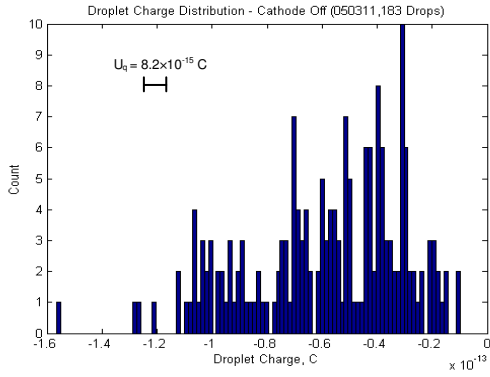


Figure 4.26 Stopping potential curve with “Cathode on” for Case 3 (Test 1) of (0 to -2800V), $V_{acc1} = -450$ V; $V_{acc2} = -2100$ V.

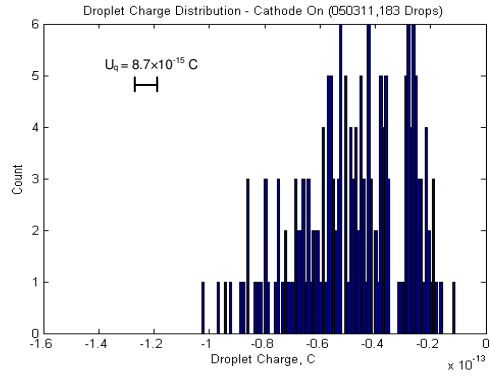
Results for Case 4, Test 1

The anode current for Case 4 of $I_{an} = 120 \pm 25$ μ A was selected to see the difference from Case 3, which was about half strength of the electron flux. The results are shown in Figure 4.27 and Figure 4.28.



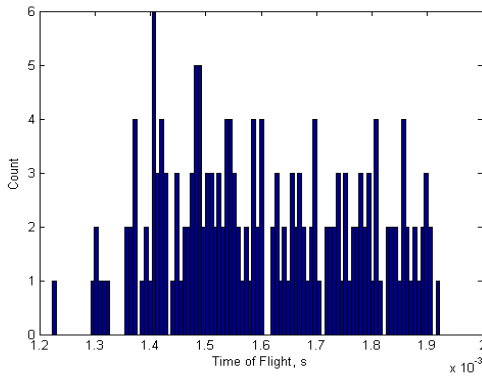
a1) Baseline Droplet charge distribution.

$$\langle q \rangle = -5.9 \times 10^{-14} \text{ C}; \sigma_q = 2.8 \times 10^{-14} \text{ C}; U_q = 8.2 \times 10^{-15} \text{ C};$$



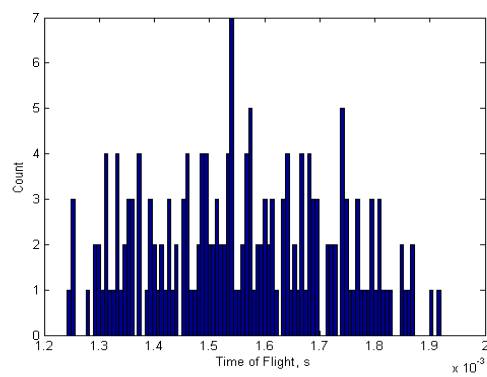
a2) Droplet charge distribution with cathode on.

$$\langle q \rangle = -4.8 \times 10^{-14} \text{ C}; \sigma_q = 1.9 \times 10^{-14} \text{ C}; U_q = 8.7 \times 10^{-15} \text{ C}$$



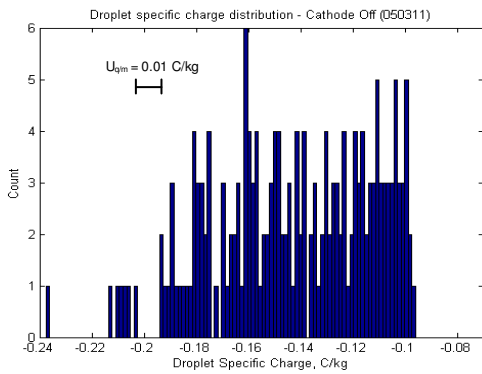
b1) Baseline Droplet time of flight distribution.

$$\langle \text{TOF} \rangle = 1.6 \text{ ms}; \sigma_{\text{TOF}} = 0.17 \text{ ms}.$$



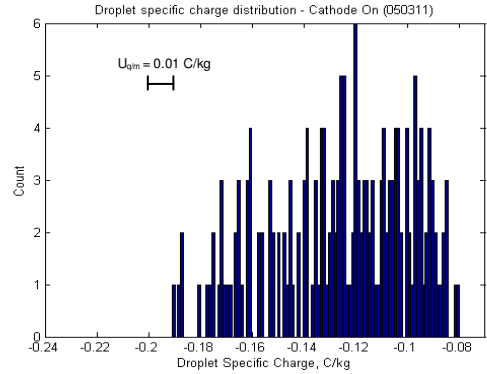
b2) Droplet time of flight distribution with cathode on.

$$\langle \text{TOF} \rangle = 1.6 \text{ ms}; \sigma_{\text{TOF}} = 0.167 \text{ ms}.$$



c) Baseline Droplet specific charge distribution.

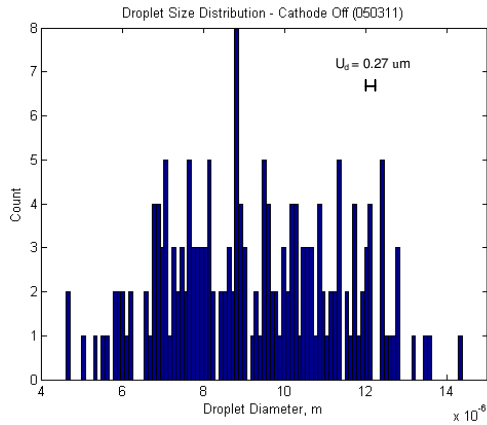
$$\langle q/m \rangle = -0.14 \text{ C/kg}; \sigma_{q/m} = 0.03 \text{ C/kg}; U_{q/m} = 0.01 \text{ C/kg}.$$



c2) Droplet specific charge distribution with cathode on.

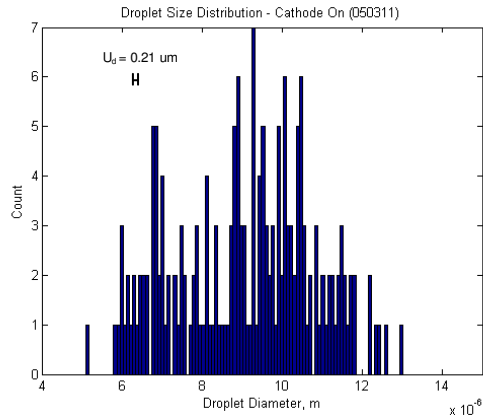
$$\langle q/m \rangle = -0.15 \text{ C/kg}; \sigma_{q/m} = 0.03 \text{ C/kg}; U_{q/m} = 0.01 \text{ C/kg}.$$

Figure 4.27 Results of Case 4, Test 1 (Charge, time-of-flight and specific charge)



a1) Baseline Droplet size distribution.

$\langle d \rangle = 9.2 \text{ um}$; $\sigma_d = 2.1 \text{ um}$; $U_d = 0.27 \text{ um}$.

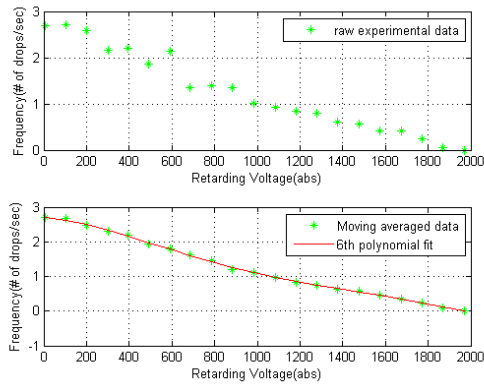


a2) Droplet size distribution with cathode on.

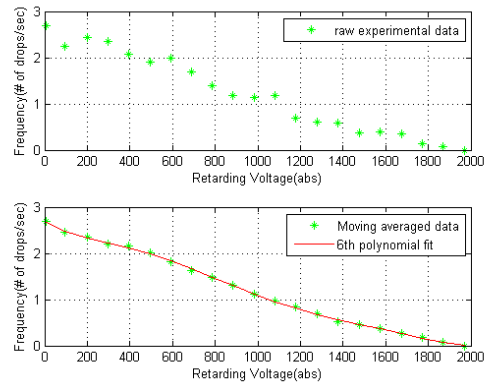
$\langle d \rangle = 8.5 \text{ um}$; $\sigma_d = 1.6 \text{ um}$; $U_d = 0.21 \text{ um}$.

Figure 4.28 Results of Case 4, Test 1 (Size)

Stopping potential curves for the baseline test and test with cathode on for Test 1 of Case 4 are shown in Figure 4.29 and 4.30.



a) Potential sweep from 0 to -2000V;



b) sweep from -2000V to 0 V.

Figure 4.29 Baseline Stopping potential curve for Case 4 (Test 1), $V_{acc} = -1700 \text{ V}$.

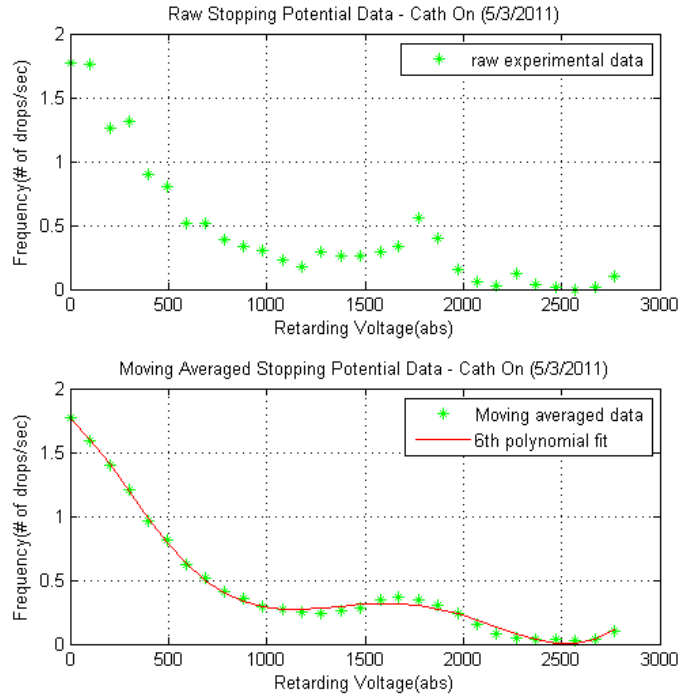


Figure 4.30 Stopping potential curve with “Cathode on” for Case 4 (Test 1) of (0 to -2800V), $V_{acc1} = -500$ V; $V_{acc2} = -2050$ V.

Because the droplet wave capture is initiated by the trigger level set on the collecting oscilloscope, the choice of trigger level is very important. Ideally, this is chosen to be as low as possible (so that the smallest possible droplets will trigger capture), but not so small that the background noise in the CDMS amplifier will trigger acquisition without a droplet having entered the sensor tube. Since time-of-flight is required for the specific charge calculation, a positive trigger level is usually set for acquisition of complete waves (since the incoming droplet generates a negative peak as shown in Figure 3.12). But the “entering” half-waves were found to occur much more frequently than complete waves. Filtering out those entering half-waves might cause some information loss. For instance, Figure 4.25 shows three plots of the droplet charge q versus V_{peak} of

each half wave, which is based on the complete waves captured in Test 1, 2 and 3 of Case 2. V_{peak} is the absolute value of induced voltage of peaks corresponding to the droplet entrance and exit from the sensing tube. In Figure 4.25, the negative, “entering” waves are mostly below the green average line compare to the positive, “exiting” waves, which means the charge calculated from the “entering” half-waves would be smaller and have a corresponding smaller value of the peak voltage than “exiting” half-waves. Figure 4.31 (b) also clearly shows that V_{peak} for some of the “entering” half-waves are less than -85 mV trigger setting. Droplet waves with V_{peak} less than the trigger level will not be captured.

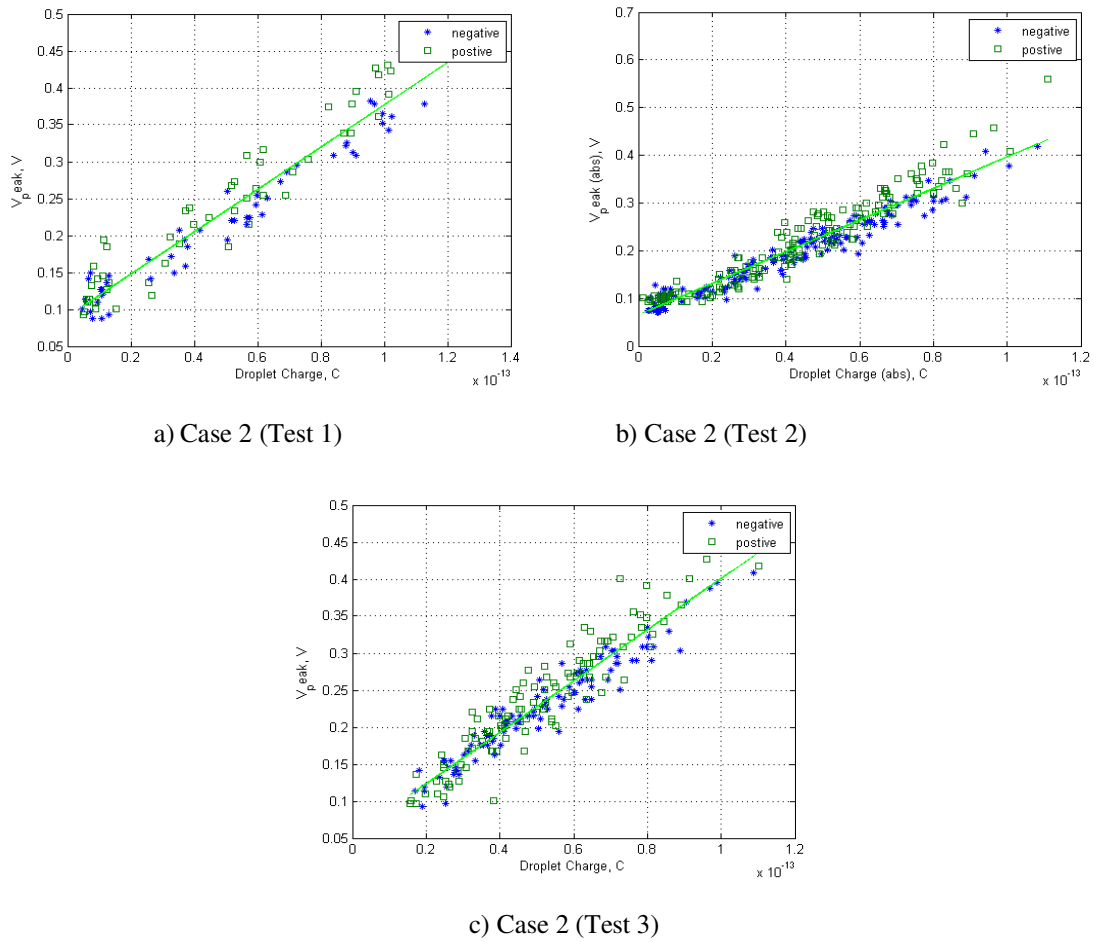
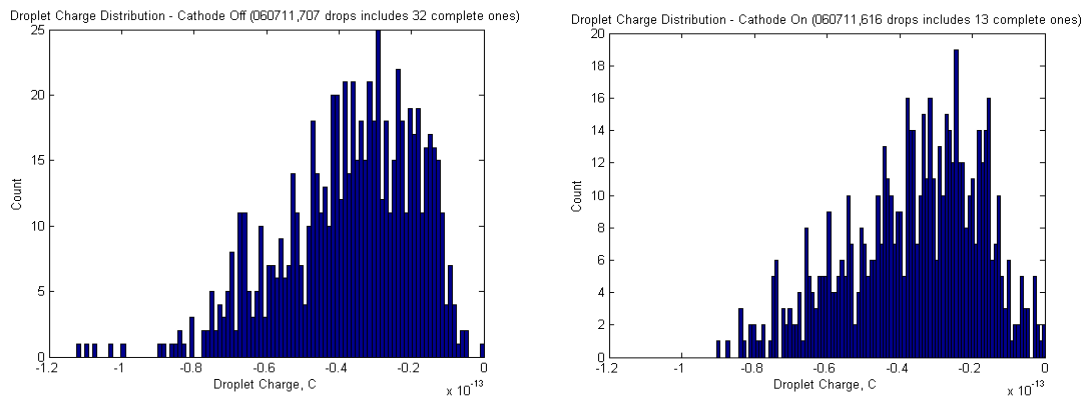


Figure 4.31 Droplet wave peak V_{peak} vs. droplet charge q for each half wave

To investigate the effect of the of the oscilloscope trigger setting on the measured droplet charge distribution, a test was performed using the conditions for Case 5, but with a negative trigger setting of -52 mV, a value just larger than the noise. 643 “entering” half waves and 32 complete waves for the cathode off case and 590 “entering” half-waves and 13 complete waves for the cathode on case were collected. Charge distributions of these two cases are presented in Figure 4.32.



a) Baseline Droplet charge distribution.

$$\langle q \rangle = -5.8528e-14 \text{ C}; \sigma = 2.8059e-14 \text{ C}.$$

b) Droplet charge distribution with cathode on.

$$\langle q \rangle = -4.8099e-14 \text{ C}; \sigma = 1.9491e-14 \text{ C}.$$

Figure 4.32 Results of Case 5 (Test 1)

Mean values and standard deviations (68% confidence level) for the distributions of droplet charge, specific charge, time-of-flight, stopping potential and droplet size before and after electron bombardment for all seven test cases are shown in Table 4.4.

Table 4.4 Summary of Test Results for Charge, Specific Charge, TOF, V_{acc} and Diameter Before and After Electron Bombardment

Case	Test	Date		Results										Remarks
				V_{acc} (V)	Diameter (μm)		Charge (10^{-14} C)		Specific C (C/kg)		TOF (ms)			
					<d>	σ_d	<q>	σ_q	<q/m>	$\sigma_{q/m}$	<TOF>	σ_{TOF}		
1	1	9/26/07	Before	-1300	5.7	1.2	-4.8	1.2	-0.5	0.2	1.0	0.2		
			After	-1508	3.5	0.7	-1.5	0.4	-0.8	0.3	0.8	0.2	Use estimated V_{acc}	
2	1	4/5/11	Before	-1700	9.3	2.5	-6.1	3.1	-0.2	0.4	1.6	0.3		
			After	-400	1.8	0.7	-0.9	0.2	-13.6	26.0	0.8	0.3		
				-1850	9.8	2.4	-6.2	3.1	-0.1	0.03	1.7	0.2		
2	2	4/12/11	Before	-1820	8.3	2.2	-4.8	2.5	-0.2	0.1	1.5	0.2		
			After	-500	1.4	0.6	-0.7	0.3	-9.1	9.0	0.5	0.3		
				-2000	8.9	0.2	-4.8	2.2	-0.1	0.03	1.5	0.2		
2	3	5/13/11	Before	-1622	8.7	1.7	-5.2	2.2	-0.2	0.03	1.6	0.2		
			After	-450	-	-	-	-	-	-	-	-		
				-1900	9.1	1.6	-5.1	2.0	-0.1	0.02	1.6	0.1		
3	1	4/22/11	Before	-1723	9.4	1.9	-5.9	2.5	-0.1	0.04	1.6	0.2		
			After	-450	-	-	-	-	-	-	-	-		
				-2100	9.1	1.9	-4.7	1.9	-0.1	0.1	1.6	0.2		
4	1	5/3/11	Before	-1700	9.2	2.1	-5.9	2.8	-0.1	0.03	1.6	0.2		
			After	-500	-	-	-	-	-	-	-	-		
				-2050	8.5	1.6	-4.8	1.9	-0.2	0.03	1.6	0.2		
5	1	6/7/11	Before	-	-	-	-3.6	1.8	-	-	-	-	Inlet half-waves	
			After	-	-	-	-3.7	1.9	-	-	-	-	Inlet half-waves	

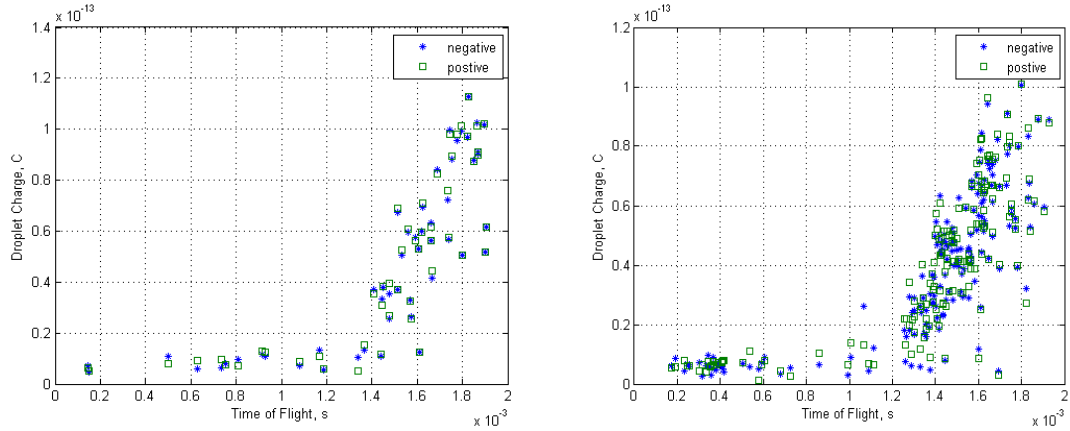
4.3 Discussion of results

Results in Section 4.2 show that among the five cases tested, two tests of Case 2 (Tests 1 and 2) clearly showed evidence of two droplet populations after the electron bombardment based on the measurements made with the CDMS. There are two indicators of multiple populations: 1) the retarding potential curve and 2) the charge/TOF distributions (histograms). While the latter only showed a clear indication of smaller drops for Test 1 and 2 of Case 2, the former always showed evidence of a smaller population when the cathode was on. Figures 4.14, 4.18, 4.22, 4.26 and 4.30 presented the stopping potential curves the five tests for which stopping potential sweeps were collected. The stopping potential curve is an important indicator used to determine if there is more than one population of droplets present.

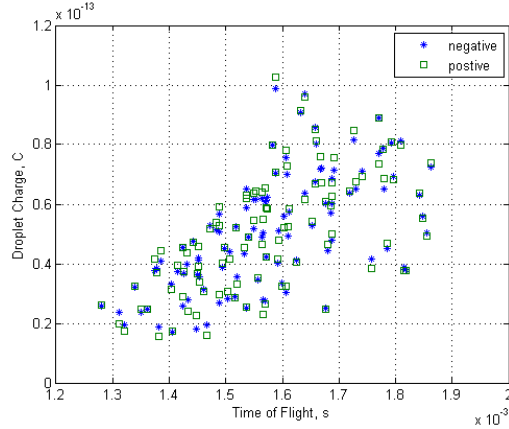
Figure 4.6 (b) shows a smaller droplet wave captured in Test 2 of Case 2 that has a very narrow area under the curve and a shorter time-of-flight (shorter distance between two peaks). This was one of two tests in which droplet waves, captured by the oscilloscope, appeared to also capture smaller droplet waves which would not have triggered capture on their own.

Figure 4.33 is a set of plots for droplet time-of-flight (TOF) versus the droplet charge for all three tests of Case 2. The charge under each half-wave, the “entering half” and “exiting half,” is calculated and plotted separately for each droplet time-of-flight (recall that the time-of-flight is the time between peaks corresponding to each half-wave). This figure shows evidence that droplets carrying less charge have a shorter time-of-flight. Droplets passing through the detector with a time-of-flight less than 0.2 milliseconds

carry a charge (magnitude) as low as $0.1 \times 10^{-13} C$. Droplets with a time-of-flight of at least 1.8 milliseconds carry more than $1 \times 10^{-13} C$ charge. This data indicates that the time-of-flight can be used as an independent indicator of a second droplet population, at least with respect to charge.



a) Two populations shown in Case 2 (Test 1) b) Two populations shown in Case 2 (Test 2)



c) One population shown in Case 2 (Test 3)

Figure 4.33 Time-of-flight vs. droplet charge for “Cathode on” cases, Case 2

For tests in which there appear to be two distinct populations, as evidenced by “plateaus” in the stopping potential curve, one needs to identify which accelerating potential, V_{acc} , corresponds to each population. Because the electrostatic potential energy

is equal to the product of the charge and electric potential, it is reasonable to assume that (post-fission) droplets with a smaller charge will have a lower accelerating potential required to bring them to rest. However the sampled droplets do not have just two values of charge, but rather a distribution of charges. So the question becomes, what value of charge should be used as the “cutoff” (i.e. in order to assign the correct value of accelerating voltage)? In the MATLAB code used to calculate the droplet properties, droplets with a charge smaller than this cutoff were assigned the smaller accelerating voltage for the purpose of calculating the specific charge and droplet size. Conversely, droplets with a larger charge were assigned the larger value of accelerating potential.

Examining Figure 4.33(c), corresponding to one population present, one can see, as discussed earlier, that there is a correlation between charge and TOF, with larger values of charge having longer flight time. From Figures 4.33(a) and (b) one can see that for cases with two populations, there is a distinct transition in the charge vs. TOF curve. For these latter cases, there appears to be one population in which the charge is proportional to the TOF and one population where the charge is relatively independent of the TOF. The transition between these two populations is relatively distinct and occurs at a charge of approximately $0.2 \times 10^{-13} C$ or a TOF of approximately 1.2 ms. Therefore, for Case 2, the TOF value of 1.2 ms was used as a parameter to determine which accelerating voltage to apply in the droplet specific charge and size calculation.

For both Test 1 and 2 of Case 2, the size distributions for droplets after electron bombardment were about the same, see Figure 4.35. Furthermore, in Test 1 a smaller sized group with mean diameter of 1.8 μm (standard deviation of 0.7 μm), as compared to the (no bombardment) mean diameter of 9.3 μm (standard deviation of 2.5 μm), was

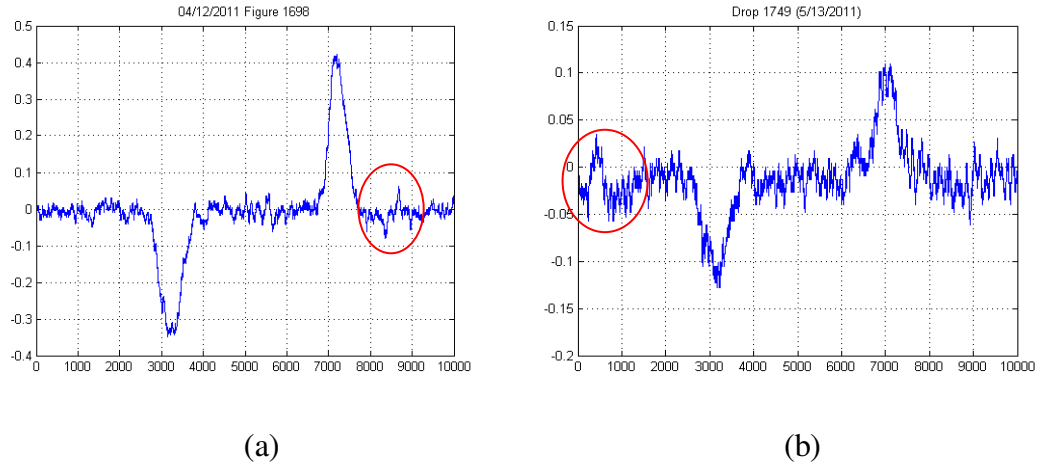
observed as shown in Figure 4.12. Similarly, for Test 2 of Case 2, a smaller sized group with mean diameter of 1.4 μm (standard deviation of 0.6 μm), as compared to the original mean diameter of 8.3 μm (standard deviation of 2.2 μm), was observed as shown in Figure 4.16.

A distinct, second population of smaller droplets was not observed in Test 3 of Case 2 or any tests of Cases 1, 3, and 4. Test results for Case 1 show a decrease in the mean droplet charge of more than two standard deviations and a time-of-flight decrease of more than one standard deviation after the electron bombardment. This suggests that the electron bombardment did result in a droplet population with a smaller diameter, although the calculation of droplet size for this case did require an estimate of the accelerating voltage (for the cathode on case) as discussed in Section 4.2. The much narrower charge distributions after the electron bombardment (0.4×10^{-14} C versus 1.2×10^{-14} C) imply a narrower distribution of droplet diameter since the estimated value of the accelerating voltage only affect the magnitude not the distribution.

Although only two sets of distribution data showed clear evidence of a second, smaller diameter droplet population after electron bombardment, the stopping potential curves for all cases, except Test 1 for Case 1, with the cathode turned on showed some evidence of a second “step” indicative of a second population. There are likely several reasons why this second population was not always detectable in the distribution data collected by the CDMS. Possible reasons as to why detection of the smaller distribution by the CDMS was limited to two tests include the following: 1) droplets (after fission) were below the resolution threshold of the CDMS; 2) smaller, negatively charged droplets produced during breakup were deflected away from their original trajectories

and attracted to the positive anode plate after fission. For a small drop with diameter $1.4 \mu m$ and charge $-0.7 \times 10^{-14} C$, it will be deflected away from its original trajectory by $6.7 mm$ when the anode plate is biased at its normal operating voltage, $V_{an} = 50 V$. This droplet will not be captured if its original trajectory is aligned up with the collimator of CDMS since the diameter of the collimator is only $0.9 mm$.

Figure 4.34 shows two examples of collected waves, in which small drops may have been captured inadvertently (because the oscilloscope had triggered on a larger drop). Small waves in (a) and (b) of Figure 4.34 have a signal-noise-ratio of 4.5 and 2.5, respectively, which is larger than 1.5 times of the criterion setting in Figure 4.3 so that is enough to be distinguished from the noise. This data supports the possibility that a smaller charge (and diameter) population was present but was just not detected by the instrument. Both small waves (highlighted in the red circles) of Figure 4.34 were accidentally captured along with the larger wave but without the larger wave, those small ones would not have been detected because the oscilloscope trigger level setting of $85 mV$ is larger than their amplitudes, especially for the half-wave in (b) which has a peak amplitude less than $50 mV$.



(a) (b)
 Figure 4.34 Small drops observed accidentally

Figure 4.35 shows a summary of droplet size changes with standard deviations for all test cases. Test 1 of Case 5 is not included because only half-waves were collected and no size measurement made. As shown in Figure 4.35, Test 3 of Case 2 shows a slightly broader distribution of droplet size with a slightly larger mean diameter after electron bombardment. Test results of Case 3 (Test 1) and Case 4 (Test 1) show the droplets subject to electron bombardment have smaller average sizes (though still within one standard deviation) but with a narrower distribution, as shown in Figure 4.35. The mean charge is smaller and mean specific charge is larger after the electron bombardment. If the droplets only had a few occurrences of fission, it is possible the mass and charge for parent droplets did not change enough for detection. It's possible the daughter droplets were below the detection threshold of the CDMS (estimated in Section 4.4). This is consistent with Taflin's findings [14] that the parent droplet loses approximately 1 - 2.3% of its mass and 10 - 18% of its charge after daughter drops being ejected in one fission event.

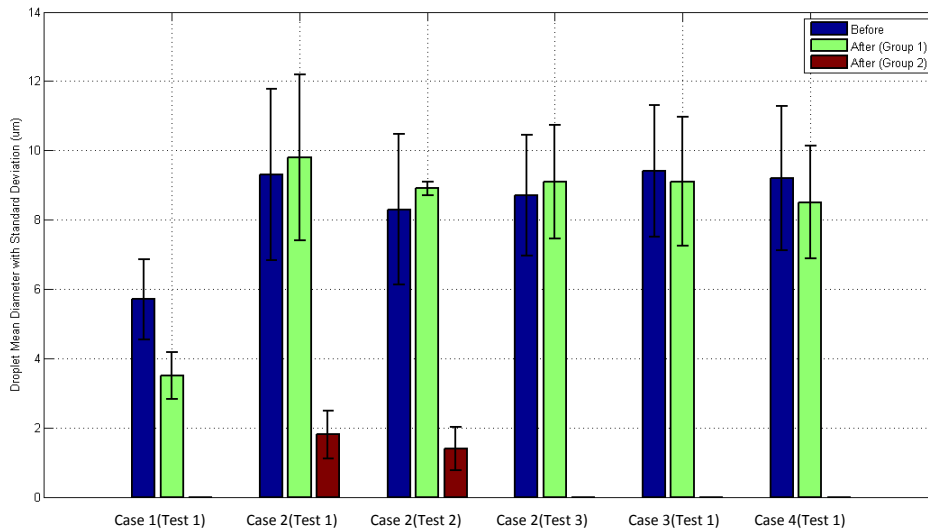


Figure 4.35 Droplet diameter changes before and after electron bombardment for all test cases (Test 1 of Case 5 not included)

Complete waves were observed much less frequently for the cases in which the cathode was on. This might have been the result of deflection of the negatively charged droplets which were attracted towards the positively biased anode plate. Despite the use of a collimator in the CDMS construction (see Section 3.3.3), it is possible that the trajectory of incoming droplets could have been deflected to the point that only the first half of the droplet wave, corresponding to the droplet entering the sensor tube, is detected. If this occurred, then the droplet would have hit the inside of the sensor tube and never produced the second (exiting) half of the waveform. Since our charge, specific charge, and diameter distributions were based only on complete (good) waves showing both peaks, the effect of including half-waves on the resulting distribution data was investigated.

Test 1 of Case 5 was performed with a trigger level that was set to a negative value, and a magnitude smaller than those used for Cases 1 through 4 (Table 4.1). The smaller trigger level for Case 5 (Test 1) was set to $V_{trig} = -52$ mV in an attempt to collect the incomplete, “inlet-half only” waves which are usually filtered out. This was done to check the effect, if any, of including these half-waves on the charge distribution. But the distribution is still similar to the complete-waves-only cases at previous tests. It was concluded that capturing the half-waves would not have significantly altered the reported charge distributions.

4.4 Measurement Sensitivity and Uncertainty Analysis

This Section presents the methodology used to estimate the uncertainty in reported values of droplet charge, specific charge, and diameter. First, the equations used to calculate these quantities from experimentally measured data are presented. This is followed by a discussion of the error propagation formula used to evaluate the relative uncertainty which has been reported in the Results Section 4.3.

The droplet diameter d is calculated from the droplet charge q and specific charge q/m

$$d = \left(\frac{6}{\rho\pi} \frac{m}{q} \right)^{\frac{1}{3}} \quad (4.4.1)$$

For a given fluid density ρ , the charge in this equation is determined from the experimentally measured (captured) droplet voltage history, the amplifier circuit gain, and the grounding resistance from the following equation.

$$q = \frac{1}{2} \int_{t_i}^{t_f} \frac{|V_1(t)|}{GR_1} dt \quad (4.4.2)$$

The specific charge is determined from the experimentally measured accelerating potential, time-of-flight and sensor tube length as

$$\frac{q}{m} = \frac{1}{2V_{acc}} \left(\frac{L}{\tau} \right)^2 \quad (4.4.3)$$

In the following discussion, it is assumed that all systematic (bias) errors are either negligible, or have been made negligible through calibration, so the uncertainties reported for the droplet charge, specific charge, and diameter are random errors. This assumption is based primarily on the following rationale:

- 1) The factory calibration of the Fluke multimeters and Tektronix oscilloscopes used make any systematic error in the reported voltages and currents small compared to the random errors. For the needle voltage, any systematic error was minimized by our own calibration of the data acquisition system used.
- 2) When calculating the droplet charge, the voltage history is integrated as shown in Eq. (4.4.2). The baseline or zero value for this integration is based on the mean value of the voltage history \overline{V}_1 , instead of assuming 0 Volts as the reference. Using the mean voltage eliminates a bias error in the droplet charge that would otherwise be introduced into the integration.
- 3) The value used for the sensing resistor R_1 , in Eq. (4.4.2) is the labeled value ($1 M\Omega$), which is slightly larger than the actual measured value ($0.9999 M\Omega$). However, the difference in the value of the charge calculated using Eq. (4.4.2) with the labeled value of R_1 (instead of the measured value) is on the order of $10^{-17} C$. Compared with the charge of the droplet, which is in the range of $10^{-15} - 10^{-14} C$ this difference is considered small enough to be negligible.

While it is impossible to completely eliminate bias error, It is believed the bias error has been reduced to a level which makes it negligible compared to the random error present. Estimation of the random error is described in the following paragraphs.

Droplet Charge

In the charge calculation, Eq. (4.4.2) can be written as

$$q = \int_{t_i}^{t_f} C(t)dt \quad (4.4.4)$$

Where the integrand parameter $C(t) = \frac{V_1(t)}{2GR_1}$. Using standard error propagation formulas

(Eq. 3.19 in Ref [35]), the relative uncertainty of the integrand is given by

$$\frac{U_C^2}{C^2} = \frac{U_{V_1}^2}{\bar{V}_p^2} + \frac{U_G^2}{G^2} + \frac{U_{R_1}^2}{R_1^2} \quad (4.4.5)$$

Where U represents the random uncertainty of a particular variable in the expression. The “signals” representing the passing droplet are the two voltage pulses, one on entry and one on exit, induced on the sensing tube. \bar{V}_p is the average of these two peaks and is used in the relative uncertainty estimation of the voltage in Eq. (4.4.5) as will be described below. The mean value of the gain \bar{G} used in the charge calculation is measured by applying a signal, produced by a signal generator, into the sensing tube and collecting the output signal of the CDMS by an oscilloscope. Comparison of the voltage amplitude for the applied and amplified waveform allows a determination of the gain. In the laboratory,

the gain was measured N_G times, usually $N_G = 10$, then values for the mean and variance of the gain are given by

$$\bar{G} = \frac{1}{N_G} \sum_{i=1}^{N_G} G_i \quad (4.4.6)$$

$$U_G^2 = \frac{1}{N_G - 1} \sum_{i=1}^{N_G} (G_i - \bar{G})^2 \quad (4.4.7)$$

The uncertainty of the load resistance R_1 was estimated to be the product of the nominal, or labeled (not the measured) resistance, and the resistor's indicated tolerance (1%).

The integrand numerator, $V_1(t)$, is the history of the induced voltage through the grounding resistor R_1 , produced by an image charge within the sensing tube. Numerical simulation of the induced charge and voltage on the sensing tube, based on the method of Weinheimer, was presented in Section 3.3.2. The simulation showed that the induced charge should represent 99.3% of the full value of the actual charge. In addition, the simulation showed that two voltage peaks produced, of opposite sign, are slightly off the positions of the entrance and exit of the tube (0.3%). This offset results in an inaccuracy in the time-of-flight recorded. These systematic errors, which result from the fact that the sensing tube is not infinitely long, are negligible compared with the random error in the voltage history $V_1(t)$ as described next.

For each test on a specific test date, a subset of a randomly chosen complete wave signal, which includes only noise, was used to determine the random error of $V_1(t)$. To

illustrate this, an example of a droplet wave is shown in Figure 4.36. Indicated on this figure is an example of this subset (of the entire history) used to estimate the signal noise level. The reference (baseline) value of the voltage used for the integration is given by the mean

$$\bar{V}_1 = \frac{1}{N_{V_1}} \sum_{i=1}^{N_{V_1}} V_{1_i} \quad (4.4.8)$$

Where N_{V_1} represents the number of the voltage data points used. The random uncertainty for the voltage waveform is given by the variance

$$U_{V_1}^2 = \frac{1}{N_{V_1} - 1} \sum_{i=1}^{N_{V_1}} (V_{1_i} - \bar{V}_1)^2 \quad (4.4.9)$$

As noted earlier, the “signals” representing the passing droplet are the two voltage pulses, one on entry and one on exit, induced on the sensing tube. \bar{V}_p is the average of these two peaks and is used in the relative uncertainty estimation of the voltage in Eq. (4.4.5). Because the pulses differ in sign, the average of the magnitudes is used, and so the average value of $V(t)$ is denoted by \bar{V}_p , and is defined by

$$\bar{V}_p = \frac{|V_{p_1}| + |V_{p_2}|}{2} \quad (4.4.10)$$

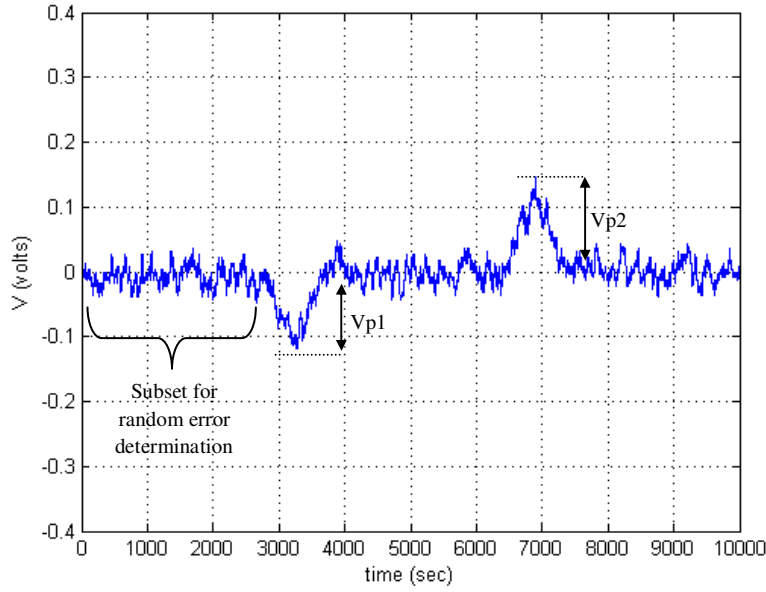


Figure 4.36 Determination of U_{V_1} and \bar{V}_p

Once the uncertainty of the integrand was determined (U_C), the propagation of error upon integration was calculated using the method described in Ref. [36]. Using Equation 18 from Ref. [36], the variance in the calculated charge is given by

$$U_q^2 \approx U_C^2 \Delta t \beta \quad (4.4.11)$$

where $\beta = t_f - t_i$, is the time span of the integration, which is two times of the droplet time-of-flight, and the time step (set on the oscilloscope) was $\Delta t = 4 \cdot 10^{-7}$ seconds. Therefore, the uncertainty of q can be found by Eq. (4.4.5) and Eq. (4.4.11), which is in a range of $4.1 \times 10^{-15} \text{ C} - 1.0 \times 10^{-14} \text{ C}$. Since $e = 1.6022 \times 10^{-19} \text{ C}$, the CDMS system can measure with a resolution of at best 25590 electrons. See Appendix C for detailed calculations.

Droplet Specific Charge

From Eq. (4.4.3), the random uncertainty of the specific charge q/m , which is denoted as $U_{q/m}$, is determined by the uncertainty in the tube length L , the droplet's time-of-flight τ , and the accelerating potential V_{acc} . The relative error for the specific charge is given by

$$\frac{U_{q/m}^2}{(q/m)^2} = \frac{U_{V_{acc}}^2}{V_{acc}^2} + 4 \left(\frac{U_L^2}{L^2} + \frac{U_\tau^2}{\tau^2} \right) \quad (4.4.12)$$

The relative uncertainty in the tube length (measured by precision caliper) and the time-of-flight (measured by an oscilloscope) will be much less than the uncertainty in the accelerating potential, so $\frac{U_L^2}{L^2}, \frac{U_\tau^2}{\tau^2} \ll \frac{U_{V_{acc}}^2}{V_{acc}^2}$ and $U_{q/m}$ is dominated by the uncertainty of V_{acc} . The last two terms at right hand side of Eq. (4.4.12) can be neglected and the specific charge relative error given by

$$\frac{U_{q/m}^2}{(q/m)^2} = \frac{U_{V_{acc}}^2}{V_{acc}^2} \quad (4.4.13)$$

The accelerating potential is determined by fitting the retarding potential distribution pattern by a polynomial curve then differentiating, which gives a value of accelerating voltage that corresponds to the maximum value of derivative. This was one of the most challenging of the measurements made. The uncertainty of accelerating potential was then determined by the spans of the sloping regions on the stopping potential curves for each test. Figure 4.36 shows the conceptual diagram of how $U_{V_{acc}}$

was determined for reach group of droplets. As described in the Results section, each test, and each case of each test (i.e. with filament on and filament off), had an associated value of V_{acc} and $U_{V_{acc}}$. For details, see Appendix C.

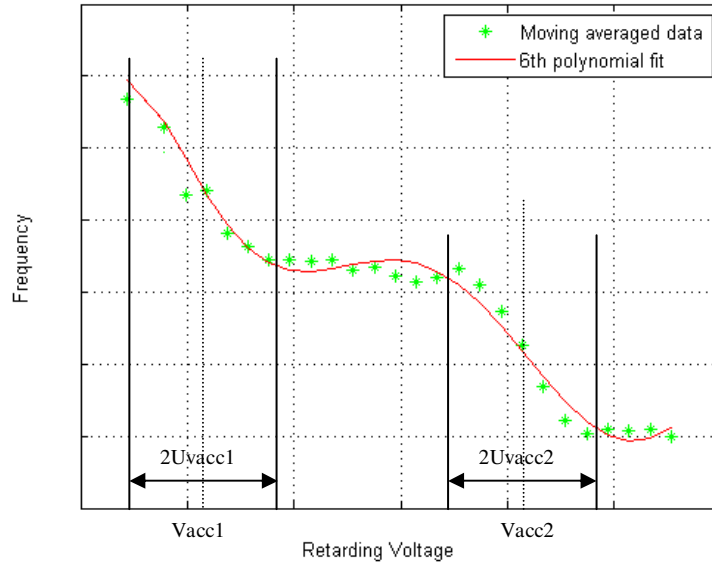


Figure 4.37 Determination of $U_{V_{acc}}$

Droplet Diameter

With relative uncertainties of charge q and specific charge $\frac{q}{m}$ both determined, the uncertainty in the droplet diameter d can be found by

$$\frac{U_d^2}{d^2} = \frac{1}{9} \left(\frac{U_q^2}{q^2} + \frac{U_{q/m}^2}{(q/m)^2} \right) \quad (4.4.14)$$

Here the uncertainty in the (published) liquid density is neglected relative to other terms.

$$\frac{U_\rho^2}{\rho^2} \ll \frac{U_q^2}{q^2}, \frac{U_{q/m}^2}{(q/m)^2}$$

Summary of Random Error Estimates

The results of the error estimates for the droplet charge, specific charge, and diameter are summarized in Table 4.5 below. These estimates have been used in the presentation and discussion of the results in Section 4.2. More detailed tables with values for the parameters used in the above equations are provided in Appendix C.

Table 4.5 Errors for droplet charge, specific charge and diameter

Case	Test	Date		$U_{q/m}$	U_q	U_d
1	1	9/26/07	Before	4.0×10^{-2}	5.2×10^{-15}	1.5×10^{-7}
			After	5.1×10^{-2}	4.1×10^{-15}	7.8×10^{-8}
2	1	4/5/11	Before	1.7×10^{-2}	9.4×10^{-15}	2.7×10^{-7}
			After	8.5	6.7×10^{-15}	3.7×10^{-7}
2	2	4/12/11	Before	1.9×10^{-2}	1.0×10^{-14}	3.0×10^{-7}
			After	4.6	5.9×10^{-15}	2.3×10^{-7}
2	3	5/13/11	Before	1.9×10^{-2}	8.3×10^{-15}	3.6×10^{-7}
			After	-	-	-
3	1	4/22/11	Before	1.2×10^{-2}	9.7×10^{-15}	2.7×10^{-7}
			After	-	-	-
4	1	5/3/11	Before	1.3×10^{-2}	8.2×10^{-15}	2.7×10^{-7}
			After	-	-	-
				1.1×10^{-2}	8.7×10^{-15}	2.1×10^{-7}

Some entries in Table 4.5 are empty that is because there were no second populations of droplets existed after electron bombardment for these tests (Test 3 of Case 2, Test 1 of Case 3 and Test 1 of Case 4). Test 1 of Case 5 (entry half-waves) is not included in the table because only half-waves were captured in the test so that droplet specific charge and diameter were not measured. It has been noticed that errors of two

specific charges q/m after the electron bombardment for Test 1, Test 2 of Case 2, respectively, are much larger than others. These errors of q/m are for the existed second population droplets after electron bombardment with smaller diameters, which have larger values of q/m . This is consistent with Taflin's findings [14] that ejected daughter drops carry larger charges compared to drops with same mass without fission.

Chapter 5 Conclusions and Recommendations

5.1 Conclusions

Droplet fission as a result of electron bombardment has been investigated as a means of controlling droplet size distribution.

The magnitude of the electron flux was chosen to be the primary control parameter for droplet fission. Because of the difficulty in estimating the actual electron emission current density (flux), as mentioned in Section 4.1, the current collected by the anode electrode I_{an} was used as the measure of the electron emission. The anode voltage V_{an} , used to control the electron drift velocity, was another important parameter for droplet size control, as it will largely determine whether an electron has sufficient kinetic energy to overcome the electric potential barrier of the passing droplets and can be captured.

Tests performed using various levels of electron emission I_{an} , and summarized in Table 4.4, have shown that the method of electron bombardment is a viable method for affecting the droplet size distribution. There are however some practical considerations that would limit its implementation in a production setting. Below is a summary of our findings and conclusions.

- 1) In all tests, two sets of data were used to indicate whether droplet fission had occurred or not. The first was the stopping potential curve. Specifically, comparison of the stopping potential curve with and without electron bombardment can reveal the

production of a second population (with a lower accelerating voltage) as a result of the electron bombardment. The second set of data is the droplet distribution data collected by the CDMS. This second set includes distribution histograms for the charge, time-of flight, specific charge, and (with a known accelerating voltage) the droplet size. Seven tests were performed including the one checking the affect of negative trigger setting to charge distribution. See Figure 4.35 for a summary of droplet diameters for six tests.

2) Results from two of the tests clearly showed a second, distinct, smaller diameter droplet population after electron bombardment in the CDMS histograms. These two tests were Case 2 (Test 1) and Case 2 (Test 2).

3) Results from three tests showed evidence of a narrowing of the droplet size distributions with a smaller average diameter after electron bombardment. For these four tests, the mean charge was smaller and the mean specific charges were larger after electron bombardment. These four tests were Case 1 (Test 1), Case 3 (Test 1) and Case 4 (Test 1).

4) Results from one test did not show evidence of either of the effects described in 2) and 3) above in the droplet distribution histograms. This test was Case 2 (Test 3).

5) The stopping potential curves for five tests, except Case 1 (Test 1), showed evidence of the introduction of a second “step” or plateau in the stopping potential curves when the droplets were subject to electron bombardment. While not as definitive as the CDMS data, this feature in the stopping potential curve is indicative of the presence of second droplet population. The stopping potential curve measurement with the cathode on for Case 1 (Test 1) was failed so was not included.

As a conclusion of all above, the proposed technique in this dissertation is approved could be used to produce a new droplet size distribution with a smaller mean droplet diameter. The size distribution was not excessively broadened as shown in Figure 4.12 (b1)-(b2) and Figure 4.16 (a1)-(a2).

There are at least two reasons that are possible explanations for a why second, smaller droplet population was not always detectable with the CDMS:

1) The charge of the smaller droplets was below the detection threshold of the CDMS (4.1×10^{-15} C). As discussed in Section 4.3, the CDMS data capture relies on the induced charge (voltage) on the sensor tube to trigger waveform acquisition. If the charge was so small that the wave “peak” was within the noise threshold, then waveform capture would not have occurred.

2) The smaller droplets, created after the fission process, were small enough that the deflection by the positively charged anode plate detected them away from the CDMS inlet aperture.

5.2 Recommendation for Future Work

While the tests performed did support the conclusion that electron bombardment can be used as a means of inducing droplet fission, the tests also revealed limitations in the CDMS instrument and overall process design that could be improved. The single most important improvement would be an increase in the attainable signal-to-noise ratio for the CDMS detector. This could be accomplished through a combination of filtering to lower ambient electrical noise in the amplifier circuit, and improvement of the sensor

design to increase sensitivity. Some approaches to improving the sensor sensitivity have been described in the literature and were discussed in Section 1.5. These strategies include using sensors with multiple stages and performing the analysis in the frequency domain.

In addition to more sensitive diagnostics, several improvements can also be suggested for the electron source and acceleration segment of the apparatus. A simple calculation using the Richardson-Dushman equation, such as the one provided in Section 2.2, can be used to provide an estimate of the electron flux to the droplets, but a higher fidelity calculation would include a detailed model of the surrounding (grounded) enclosure surfaces which can intercept electron flow and limit the flux reaching the passing droplets. A higher fidelity model would also account for the space charge of the passing droplets, which could affect the potential “seen” by the electrons and affect their drift energy. Such a model could be accomplished using commercially available, multi-physics modeling software such as COMSOL for example.

Another improvement that could be made to the electron source is the use of so-called “cold cathodes.” These types of cathodes rely on field emission rather than thermionic emission. Cold cathodes generally have longer life, less sensitivity to contamination, and could be arranged in a more uniformly distributed geometry to achieve better coverage of the passing spray.

Appendices

A.1 Operating and Calibrating Procedures for TCAC Control Program

The TCAC control VI is used to control two power supplies (Spellman SL10 High Voltage Powersupply and Glassman High Voltage (Series EH)) which provide the power to needle and retarding screen, respectively. The calibration of the voltage and current data (or telemetry) for both power supply units are accomplished using vi as well. Figure A.1 shows the front panel of TCAV vi control.

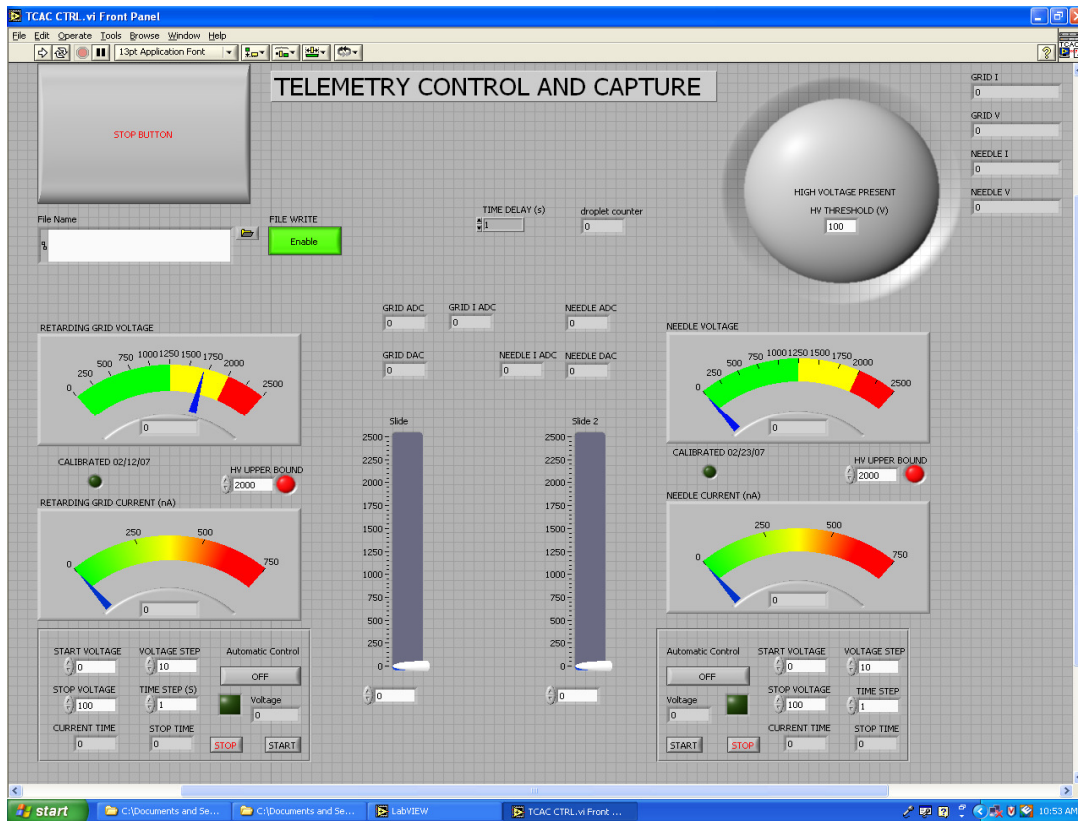


Figure A.1 Front panel of TCAC control

Note: Set the power supply control manual / auto selector switch on TCAC front panel to the “Auto” position before using TCAC control VI (See page 8 of Nathan Rosenblad’s TCAC report [30].)

Needle/Retarding Voltage Control

The front panel of TCAC control VI shows two mirrored control units for Needle and Retarding Voltage Control, respectively. Both give two ways to control the voltage.

Slide Control:

Two slider bars located in the middle of the control panel are slide control for two power supplies. Sliding the cursor to a target voltage or typing the value in the entry box will control the power supply output to the desired voltage.

Auto-sweep Control:

By clicking the button under “Automatic Control”, the auto-sweep control is turned on. VI will control the power supply unit to start at a value set by “Start Voltage” and stop at a value set by “Stop Voltage” with the voltage increment set by “Voltage Step” and the time delay set by “Time Step”. The numbers shown under the “Current Time” and “Stop Time” provide an estimate of the elapsed time and total time needed to finish the run.

Needle/Retarding Voltage Control Procedure:

Note: The Glassman supply is used to provide the power supply to needle, while the Retarding screen is supplied by Spellman. The control unit on the right half part of the control panel is for Needle control and named as “Needle XXX”, while the left half is for Retarding control and named as “Retarding Grid XXX”.

1. Click the “Arrow” icon to active the VI. A pop-up window will ask you to type in the file name and path you want to save the data to.
2. Use “Slide Control” to set the target value of needle or retarding screen voltage. The actual voltage and current are shown in the windows next to the slide bar.
3. If the retarding voltage sweep is required to find out the stopping potential curve, use “Auto-sweep Control” to control the retarding screen voltage.

Note: Do NOT set the Start / Stop Voltage of auto-sweep control to 2000 V. The high voltage bound control is set to 2000 V which limits the max output of the power supply. The voltage output will be 0 V when 2000 V is set as target voltage.

4. Click the large square “Stop Button” to safely stop the program with ZERO voltage output when the test is finished. Or sliding down the cursor in the slide bar to turn off the power then click the VI stop button (the small red stop icon next to the “arrow”) to stop the program.

Warning: A high voltage hazard could be created by only clicking the VI stop button to stop the program. It will NOT turn the power down. The high voltage is still supplied by power supply unit. To shut off the high voltage safely, a user should always turn the voltage down by click the “Stop Button”.

Calibration of Voltage / Current:

Two red HV test ports on TCAC front panel are used for voltage telemetry and control calibration by attaching a high voltage measuring Fluke volt meter to measure the actual voltage output versus the commanded v_i voltage input sent to the TCAC. The current calibration uses the normal HV ports connected to Keithley 6514 electrometer in series with a 100 M Ω resistor. The ADC and I ADC windows right above two slider bars (see Figure A.1) indicate the voltage and current calibration data, respectively. Along with the commanded voltages, one can find the calibration equations for voltage and current separately. The resulting calibration equations are entered into the TCAC v_i so that the voltage and current displayed are in the proper units.

A.2 Operating Procedure for CDMS Capture

The CDMS Capture vi is used to control the oscilloscope (TEK TDS3034) used to capture and record the droplet voltage histories during the droplet transition in detector tube. This vi was designed and built by Rosenblad [32]. Figure A.2 shows the front control panel of VI control.

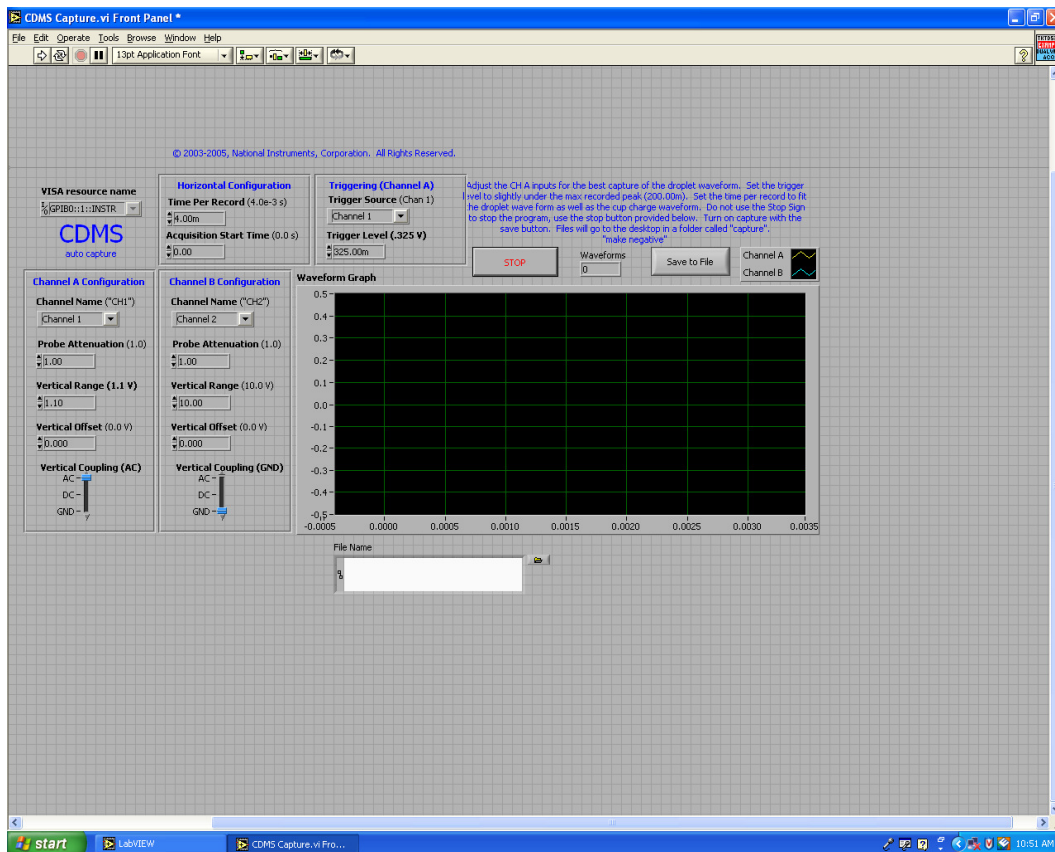


Figure A.2 Control panel of CDMS

Note: During the operation of CDMS capture, the oscilloscope is connected to a computer with a GPIB card and cable (6025E) and is completely controlled by vi. The only functional knob on oscilloscope is the one that moves the wave horizontally so that the waves captured by the vi are Completely displayed.

Operation Procedure

1. Click the “Arrow” icon to active the VI. This will NOT start the capture until the “Save to File” button is highlighted.
2. Change the “VISA resource name” to GPIB0::24::INSTR. This helps to find the oscilloscope and get the data from it.
3. If necessary, adjust the inputs for Channel A for the best capture of the droplet wave form.

Note: Channel B is not used in current test.

Note: Insure CDMS “tube” is connected to the oscilloscope through Channel 1.

4. Set the trigger level that slightly below the wave peak. To do this, observe the waves shown on oscilloscope without trigger setting to determine a proper trigger level.

Note: Negative trigger level should be set for negatively charged droplets while positive one should be set for positively charged droplets.

Note: Always put a unit after the value if the trigger level is at millivolt level otherwise the VI will take a default setting of “volt”.

5. Set the time per record to fit the droplet wave form. This will depend on the time-of-flight of the droplets.

Note: Always put a unit after the value if the time per record is at millisecond level otherwise the VI will take a default setting of “second”.

6. Make sure the oscilloscope is connected correctly and turned ON.
7. Click the “Save to File” button to start capturing the waves. The button will be highlighted by red color when it’s activated.

Note: All data files are saved automatically to the folder named “capture” on Desktop. One file is for one waveform. Operator can choose to save the data to other file location by typing the path in the blank box under the “Waveform Graph”.

8. The number of waveforms captured and recorded by the vi will be shown in the small window right above the window of “Waveform Graph”.

Note: An error message window will pop up when the waves are not captured continuously. The vi counts it as one waveform so that the number of waveform is added to the total as one but no data file is created.

9. Stop the program by clicking the “STOP” button that is on the left side of the “Save to File” button.

Note: Clicking the stop sign of the LabVIEW will NOT stop the program.

10. Always press the “Autoset” button on the oscilloscope to “wake-up” the oscilloscope from the control of VI.

B.1 MATLAB Code for Droplet Charge, Specific Charge and Size

Analysis

```
clear all;clc

%%%CDMS Variables%%%

g=945;      %gain of cdms amplifier, measured on 101209

R=1e6;      %resistance of resistor1 in cdms circuit in ohms

dt=4e-7;    %time step,s; frequency of data being captured

L=0.0348;   %Length of detector tube,m

tvalue=0;   %value of tof distinguish 2 groups of droplets,sec

Vacc1=-1508; %accelerating voltage 1,V

Vacc2=-1508; %accelerating voltage 2,V

r=976;      %Density of electrospray fluid,kg/m^3

%%%Data File input%%%

N=22;       %Lines wanna be skipped in data file

NT=2000;    %#of data points for each wave used to calc. off-axis value

Ndrop=0;    %# of good waves

fileName='capture_092607'; % name of the data folder

charge=1;   %Positive drop "0" or negative drop"1"

a=2066; b=2564; %Index of first & last file(092607,cath on)

cc=[2071;2078;2112;2168;2329;2415;2427;2476;2510;2541;2559]; %Index of bad data files(092607,cath
on)

%%% This section is to:

%%% 1. select good data files

%%% 2. calculate q for each good wave

%%% 3. Evaluate the affect of V off-axis value

for k=a:b
```

```

icounter=0;

fileNumber=k;

%% remove data files with index number stated in matrix "cc"

for i=1:length(cc); if fileNumber==cc(i); icounter=1; end; end;

if icounter==0;

    inf1=sprintf('/CDMS_07-09-26_%04d.lvm',fileNumber); %write data to a string "/CDMSCDMS_07-
09-25_xxxx.lvm"

    infile=sprintf([fileName,inf1]); %add file name after folder name

    [fid, message]=fopen(infile,'r');%open the file as read

    [to,v]=textread(infile,'%f%f','headerlines',N);

    fclose(fid); %close file

%% q calculation for each wave

[vmax,tpp]=max(v);%find positive peak voltage and corresponding t position;

[vmin,tnp]=min(v);%find negative peak voltage and corresponding t position;

if ((vmax>0.07)&&(vmin<-0.07)) %filter out files with only noises

    if charge==0;

        tt=0.5*(tnp-tpp);t1=round(tpp-tt);t2=round(tpp+tt);t3=round(tnp+tt);

    else

        tt=0.5*(tpp-tnp);t1=round(tnp-tt);t2=round(tnp+tt);t3=round(tpp+tt);

    end;

    if ((t1>0)&& (t3<10001)) %filter out incomplete waves

        Ndrop=Ndrop+1;

%% V off-axis value calculation:

    % by first NT data points (before 1st peak) for each wave

    %v_off1(k)=mean(v(1:NT)); sigma_v_off1(k)=std(v(1:NT));

    %k: the file # of waves, help to find corresponding waves

    %v_off(Ndrop)=mean(v(1:NT)); sigma_v_off(Ndrop)=std(v(1:NT));

    % by all data points for each wave

```

```

v_off(Ndrop)=mean(v); v_std(Ndrop)=std(v);

vl=v(t1:t2)-v_off(Ndrop); vr=v(t2:t3)-v_off(Ndrop); %consider V off-axis

%vl=v(t1:t2); vr=v(t2:t3); % not consider V off-axis

%%% plot out good waves

%y=v_off(Ndrop); figure(k),plot(to,v,to,y,'r');grid on;

%v1=v(t1:t3); figure(1),plot(v1);grid on; hold on; %all selected waves on one plot

tl=(1:length(vl))*dt; tr=(1:length(vr))*dt; %tl=tr

ql(Ndrop)=trapz(tl,vl/(g*R)); qr(Ndrop)=trapz(tr,vr/(g*R));

q(Ndrop)=-((abs(ql(Ndrop))+qr(Ndrop))/2);

t(Ndrop)=abs((tnp-tp))dt; %time interval between two peaks

vrr(Ndrop)=vmax;vll(Ndrop)=vmin; % (+-)peaks of each wave

%%%calc. q by moving g&R out of integral, results are same%%%

%vl(Ndrop)=trapz(tl,vl); vr(Ndrop)=trapz(tr,vr);

%ql(Ndrop)=vl(Ndrop)/(g*R); qr(Ndrop)=vr(Ndrop)/(g*R);

%q(Ndrop)=-((abs(ql(Ndrop))+qr(Ndrop))/2);

end;end;end;end;

q_avg=mean(q); q_std=std(q); t_avg=mean(t); t_std=std(t);

%v_off_avg=mean(v_off); v_off_std=std(v_off); %how off-axis values distribute

%====plot of Vpeak vs charge for all half waves =====

figure(1),plot(abs(ql),abs(vll),'*',qr,vrr,'s','MarkerSize',5);grid on;hold on; %Vpeak vs charge q.

qtotal=[abs(ql),qr];vtotal=[abs(vll),vrr];%figure(1),plot(qtotal,vtotal,'*',5);grid on;hold on;

c=polyfit(qtotal,vtotal,1); %linear fitting

vavg=polyval(c,qtotal);plot(qtotal,vavg,'g');grid on;hold off;

xlabel('Droplet Charge, C'),ylabel('V_peak, V');legend('negative','postive');

figure(2),plot(t,abs(ql),'*',t,qr,'s','MarkerSize',5);grid on; %tof vs charge q.

xlabel('Time of Flight, s'),ylabel('Droplet Charge, C');legend('negative','postive');

vtrig=0.085; %trigger level of o-scope for wave capture, V

```

```

qmin=(vtrig-c(2))/c(1)
v2=min(vtotal);qmin2=(v2-c(2))/c(1)

%%% q/m & diameter calculation for each droplet%%%
vp=8.8541878176e-12; %vacuum permittivity in F/m or C^2/J.m
sig = 0.028; %TBP surface tension [N/m]
G1=0;G2=0;
for i=1:Ndrop;
    if t(i)< tvalue;
        G1=G1+1;
        tt1(G1)=t(i);q1(G1)=q(i);
        qm1(G1)=(1/(2*Vacc1))*((L/tt1(G1))^2);
        D1(G1)=((6/(r*pi))*(1/qm1(G1))*q1(G1))^(1/3);
        %Qray(i)=-8*pi*(vp*sig)^0.5*D(i)^1.5; %Rayleigh Charge Limit [C]
    else
        G2=G2+1;
        tt2(G2)=t(i);q2(G2)=q(i);
        qm2(G2)=(1/(2*Vacc2))*((L/tt2(G2))^2);
        D2(G2)=((6/(r*pi))*(1/qm2(G2))*q2(G2))^(1/3);
    end;
end;
if G1==0;
    qm=qm2; D=D2;
else
    t1_avg=mean(tt1);t1_std=std(tt1);t2_avg=mean(tt2);t2_std=std(tt2);
    q1_avg=mean(q1);q1_std=std(q1);q2_avg=mean(q2);q2_std=std(q2);
    qm1_avg=mean(qm1);qm1_std=std(qm1);qm2_avg=mean(qm2);qm2_std=std(qm2);
    D1_avg=mean(D1);D1_std=std(D1);D2_avg=mean(D2);D2_std=std(D2);

```

```

qm=[qm1,qm2];D=[D1,D2];

end;

qm_avg=mean(qm); qm_std=std(qm); D_avg=mean(D); D_std=std(D);

%Qray_avg=mean(Qray);

%==== Guassian dist based on D_avg & D_std =====
%x=[0:1e-8:14e-6];f=(1/(D_std*(2*pi)^.5))*exp(-(x-D_avg)^2/(2*D_std^2));

%dmin=((6/(r*pi))*(1/qm_avg)*-qmin)^(1/3)
%dmin2=((6/(r*pi))*(1/qm_avg)*-qmin2)^(1/3)

for i=1:Ndrop;

    f1(i)=(1/(D_std*(2*pi)^.5))*exp(-(D(i)-D_avg)^2/(2*D_std^2));
%   f2(i)=(1/(D_std*(2*pi)^.5))*exp(-(D(i)-(D_avg-D_std))^2/(2*D_std^2));
%   f3(i)=dmin+0*i;
%   f4(i)=dmin2+0*i;

end;

%figure(2),plot(D,f1,'*',D,f2,'*r',f3,f1,'g',f4,f1,'b');grid on;

%legend('before e-bomb','after e-bomb','Min D with trigger level setting','Min D with actual Vmin');

%[f1max,d1]=max(f1);[f2max,d2]=max(f2); Ddiff=D(d2)-D(d1) %check if f2 shift to left with one std

x1=min(q):(max(q)-min(q))/100:max(q);

figure(3),hist(q,x1);xlabel('Droplet Charge, C'),ylabel('Count');%grid on;

xlim([-11e-14 0]);

title('Droplet Charge Distribution - Cathode Off (092607,333 Drops)');

x4=min(t):(max(t)-min(t))/100:max(t);

figure(4),hist(t,x4);xlabel('Time of Flight, s'),ylabel('Count');%grid on;

xlim([.4e-3 1.8e-3]);

x2=min(qm):(max(qm)-min(qm))/100:max(qm);

figure(5),hist(qm,x2);xlabel('Droplet Specific Charge, C/kg'),ylabel('Count');%grid on;

```

```
xlim([-2 -0.1]);  
title('Droplet specific charge distribution - Cathode Off (092607)');  
x3=min(D):(max(D)-min(D))/100:max(D);  
figure(6),hist(D,x3);xlabel('Droplet Diameter, m'),ylabel('Count');%grid on;  
xlim([1e-6 11e-6]);  
title('Droplet Size Distribution - Cathode Off (092607)');
```

B.2 MATLAB Code for Accelerating Potential Determination

```
clear all;clc

%%%%%%%%%%%%%%%%%%%%%%%%%%%%%%%%%%%%%%%%%%%%%%%%%%%%%%%%%%%%%%%%%%%%%%%%%
%%%Read data: time,RV,RI,NV,NI,#of droplets
filename='test_092607.lvm';
N=21; %Lines wanna be skipped in data file
[t,RV,RI,NV,NI,nod]=textread(filename,'%f%f%f%f%f%f','headerlines',N);

%%%%%%%%%%%%%%%%%%%%%%%%%%%%%%%%%%%%%%%%%%%%%%%%%%%%%%%%%%%%%%%%%%%%%%%%%
%%%Retarding Voltage vs. Time (Raw data plot)
figure(1),plot(t, RV);grid on;
xlabel('time (s)'),ylabel('Retarding Voltage (v)');
title('Retarding Voltage vs. time');

%%%%%%%%%%%%%%%%%%%%%%%%%%%%%%%%%%%%%%%%%%%%%%%%%%%%%%%%%%%%%%%%%%%%%%%%%
%%%Input File
Vo=0; %start voltage
Ve=1900; %stop voltage (abs)
dV=100; %voltage increment (abs)
dt=30; %time interval
%to1=5*60; %time staying at Vo: 5 mins=300 secs --- Case I
to2=dt; %time staying at Vo: 30 secs --- Case II
%c=.885; %adjustment for ignoring the transition points;
c=2.2; %or bigger if increment is higher than 100v
%c=.4; %adjustment for ignoring the transition points,dV=25v;

%====Run for Ramp-down "1" or Ramp-up "0"=====
w=1;

%=====
```

%%%%Main Program%%%

M=length(RV);

%a=(Ve-Vo)/dV+1; %number of sections that RV holding at specific values

a=(Ve-0)/dV+1; %number of sections that RV holding at specific values

%a1=Vo/dV; %number of RV sections skipped

%b=to1/dt; %for case I, b>1

b=to2/dt; %for case II, b=1

if w==1;

%%ramping down%%

%%Cut away unwanted data 0v points,only for long or unstable '0v' run%%

%for i=1:M; if abs(RV(i))>=Vo+dV/2; g=i-1;break;end;end; %last "0" before RV increasing

%stay at 0v

%==Case I

%p(1)=g-to1; m(1)=p(1)+dt; %p/m: start/end points of each section

%for i=2:b; m(i)=m(i-1)+dt; p(i)=p(i-1)+dt; end;

%==Case II

%p(1)=g-to2; m(1)=p(1)+dt;

%%MANUALLY PICKUP POINTS%%

%p(1)=1; %1st pt.;

%m(1)=64-N; %last 0v;(test 061107 100v 60s)

%m(1)=55-N; p(1)=m(1)-dt; %(test 061107 100v 30s)

%m(1)=307-N; p(1)=300-N; %(test 061107 100v 10s)

m(1)=8249-N; p(1)=m(1)-dt; %(test 092607 100v 30s,cath off)

%m(1)=66-N; p(1)=m(1)-dt; %(test 081310 100v 30s,b)

%m(1)=192-N; p(1)=m(1)-dt; %(test 081310 100v 60s,c)
%m(1)=67-N; p(1)=m(1)-dt; %(test 081310 50v 30s,d)
%m(1)=4486-N; p(1)=m(1)-dt; %(test 090810 100v 30s)
%m(1)=129-N; p(1)=m(1)-dt; %(test 092710 100v 30s)
%m(1)=2034-N; p(1)=m(1)-dt; %(test 092910 50v 30s)
%m(1)=5058-N; p(1)=m(1)-dt; %(test 092910 2nd 50v 30s)
%m(1)=61-N; p(1)=m(1)-dt; %(test 100410 1st 50v 30s)
%m(1)=2891-N; p(1)=m(1)-dt; %(test 100410 2nd 50v 30s)
%m(1)=13267-N; p(1)=m(1)-dt; %(test 100710 2nd 50v 30s)
%m(1)=7398-N; p(1)=m(1)-dt; m(a)=10279-N;%(test 100710 1st 25v 60s)
%m(1)=548-N; p(1)=233-N; %(test 101310 100v 600s)
%m(1)=978-N; p(1)=445-N; %(test 101510 50v 600s)
%m(1)=943-N; p(1)=643-N; %(test 101910 50v 600s)
%m(1)=114-N; p(1)=m(1)-N; %(test 113010 100v 30s)
%m(1)=1598-N; p(1)=m(1)-N; %(test 113010 100v 30s)
%m(1)=2618-N; p(1)=m(1)-dt; %(test 120910 100v 30s,cath off)
%m(1)=3656-N; p(1)=m(1)-dt; %(test 120910 100v 30s,cath on)
%m(1)=5614-N; p(1)=m(1)-dt; %(test 120910 25v 30s)
%m(1)=2903-N; p(1)=m(1)-dt; %(test 121310 100v 60s)
%m(1)=2935-N; p(1)=m(1)-dt; %(test 121310 100v 60s,cath on)
%m(1)=6818-N; p(1)=m(1)-dt; %(test 121310 100v 30s,cath off)
%m(1)=4593-N; p(1)=m(1)-dt; %(test 022411 100v 30s,cath on)
%m(1)=2659-N; p(1)=m(1)-dt; %(test 022411 100v 30s,cath off)
%m(1)=2081-N; p(1)=m(1)-dt; %(test 030311 100v 30s,cath off)
%m(1)=4816-N; p(1)=m(1)-dt; %(test 030311 100v 30s,cath on,case 1)
%m(1)=6905-N; p(1)=m(1)-dt; %(test 030311 100v 30s,cath on,case 2)
%m(1)=8181-N; p(1)=m(1)-dt; %(test 030311 100v 30s,cath on,case 3)
%m(1)=5458-N; p(1)=m(1)-dt; %(test 031611 100v 30s,cath off)

```

%m(1)=7928-N; p(1)=m(1)-dt; %(test 031611 100v 30s,cath on)
%m(1)=4318-N; p(1)=4309-N; %(test 040511 100v 30s,cath off)
%m(1)=10010-N; p(1)=10016-N; %(test 040511 100v 30s,cath on)
%m(1)=4671-N; p(1)=m(1)-dt; %(test 041211 100v 30s,cath off)
%m(1)=10309-N; p(1)=10234-N; %(test 041211 100v 90s,cath on)
%m(1)=7813-N; p(1)=m(1)-dt; %(test 042211 100v 30s,cath off)
%m(1)=10815-N; p(1)=10898-N; %(test 042211 100v 90s,cath on)
%m(1)=1788-N; p(1)=1762-N; %(test 050311 100v 60s,cath off)
%m(1)=6320-N; p(1)=m(1)-dt; %(test 050311 100v 90s,cath on)
%m(1)=1432-N; p(1)=m(1)-dt; %(test 051311 100v 60s,cath off)
%m(1)=9422-N; p(1)=9386-N; %(test 051311 100v 90s,cath on)

%%Remove transitional points.

x(1)=0; %start from 0V

%x(1)=510; %start from 500V, dV=25v

for i=2:a;

    x(i)=x(i-1)+(dV-c);

end;

%%Find start/end points for each RV section

for i=m(b):M; if abs(RV(i))>=x(2);p(b+1)=i;break;end;end; %find p(2)

%for i=m(b):M; if abs(RV(i))>=x(a1+2);p(b+1)=i;break;end;end; %find p(2),for RV section skip(Vo not
start from 0)

%for i=m(b):M; if abs(RV(i))>=x(1);p(b+1)=i;break;end;end; %find p(2),for dV=25

for j=2:a-1; %find p(3~a+1),m(2~a)

%for j=2:(a-a1)-1; %find p(3~a+1),m(2~a)

    for i=m(j+(b-1)-1):M; if abs(RV(i))>=x(j+1);p(j+b)=i;m(j+(b-1))=i-2;break;end;end;

    %for i=m(j+(b-1)-1):M; if abs(RV(i))>=x(j+a1+1);p(j+b)=i;m(j+(b-1))=i-2;break;end;end;

    %for i=m(j+(b-1)-1):M; if abs(RV(i))>=x(j);p(j+b)=i;m(j+(b-1))=i-2;break;end;end; %for dV=25

```

```

end;

for i=p(b+a-1):M;if abs(RV(i))<=x(a);m(a+b-1)=i-1;break;end;end; %find m(a),hide for dV=25

%for i=p(b+(a-1)-1):M;if abs(RV(i))<=x(a-1);m((a-1)+b-1)=i-1;break;end;end; %find m(a),hide for
dV=25

RV1=[RV(p(1):m(a+b-1))]; t1=[t(p(1):m(a+b-1))];

%RV1=[RV(p(1):m((a-1)+b-1))]; t1=[t(p(1):m((a-1)+b-1))];

%%%%%%%%

else

%%%%%%%%ramping up%%%%%%%%
%%%%%%%%MANUALLY PICKUP POINTS%%%%%%%%

%bad1=1949; %1st pt.; bad2=3105; %last -50V; bad3=3148; %start 0v; (test 030707 50v 30s)

%bad1=1188; %1st pt.; bad2=2314; %last -50v; bad3=2319; %1st 0V; bad4=2329;%last 0v; (test 061107
50v 30s)

%bad1=624;bad2=1184;%last -100v; bad3=1189;%1st 0v;bad4=1198;%(test061107 100v 30s)

%bad1=101;bad2=286; %(test061107 100v 10s)

bad1=8920;bad2=9490;%last -100v;

bad3=9534;%1st 0v;

bad4=9564;%(test092607 100v 30s,cath off)

%bad1=837;bad2=1617;%last -100v; bad3=1643;%1st 0v;bad4=1673;%(test081310 100v 30s)

%bad1=1783;bad2=3330;%last -100v; bad3=3335;%1st 0v;bad4=3395;%(test081310 100v 60s)

%bad1=1624;bad2=3116;%last -150v; bad3=3140;%1st 0v;bad4=3170;%(test081310 50v 30s)

%bad1=5300;bad2=6109;%last -100v; bad3=6114;%1st 0v;bad4=6144;%(test090810 100v 30s)

%bad1=909;bad2=1700;%1st pt.&last -100v; bad3=1706;%1st 0v;bad4=1736;%(test092710 100v 30s)

%bad1=3480;bad2=4921;%1st pt.&last -50v;bad3=4927;%1st 0v;bad4=4957;%(test092910 50v 30s)

%bad1=1416;bad2=2736;%1st pt.&last -50v;bad3=2752;%1st 0v;bad4=2782;%(test100410 50v 30s)

```

```

%bad1=14437;bad2=15577;% 1st pt.&last -525v;bad3=15581;% 1st -500v;bad4=15611;%(test100710 50v
30s)
%bad1=10258;bad2=13137;% 1st pt.&last -500v;bad3=13139;% 1st 0v;bad4=13191;%(test100710 25v 60s)
%bad1=783;bad2=1414;%last -100v; bad3=1418;% 1st 0v;bad4=1448;%(test113010 100v 30s)
%bad1=4646;bad2=5546;%last -100v; bad3=5551;% 1st 0v;bad4=5581;%(test120910 100v 30s)
%bad1=4721;bad2=6520;%last -100v; bad3=6581;% 1st 0v;bad4=6641;%(test121310 100v 60s)
%bad1=4819;bad2=6618;%last -100v; bad3=6624;% 1st 0v;bad4=6684;%(test013111 100v 60s,cath on)
%bad1=7485;bad2=8085;%last -100v; bad3=8089;% 1st 0v;bad4=8159;%(test013111 100v 30s,cath off)
%bad1=2729;bad2=3329;%last -100v; bad3=3410;% 1st 0v;bad4=3440;%(test030311 100v 30s,cath off)
%bad1=5463;bad2=6083;%last -100v; bad3=6090;% 1st 0v;bad4=6120;%(test030311 100v 30s,cath
on,case 1)
%bad1=6083;bad2=6744;%last -100v; bad3=6749;% 1st 0v;bad4=6809;%(test031611 100v 30s,cath off)
%bad1=8571;bad2=9201;%last -100v; bad3=9207;% 1st 0v;bad4=9237;%(test031611 100v 30s,cath on)
%bad1=4890;bad2=5489;%last -100v; bad3=5495;% 1st 0v;bad4=5525;%(test040511 100v 30s,cath off)
%bad1=5276;bad2=5906;%last -100v; bad3=5913;% 1st 0v;bad4=5943;%(test041211 100v 30s,cath off)
%bad1=8434;bad2=9033;%last -100v;bad3=9080;% 1st 0v;bad4=9110;%(test042211 100v 30s,cath off)
%bad1=2969;bad2=4169;%last -100v; bad3=4174;% 1st 0v;bad4=4234;%(test050311 100v 60s,cath off)
%bad1=2682;bad2=3881;%last -100v; bad3=3886;% 1st 0v;bad4=3946;%(test051311 100v 60s,cath off)

```

```

%% %% Cut away unwanted data points %% %%

```

```

p(1)=bad1-N;

```

```

%% Find values close to RV that's held for secs

```

```

x1(1)=abs(RV(p(1)));%initial value of separation points = start V

```

```

%x1(1)=1657; %dV=25

```

```

for i=2:a;

```

```

    x1(i)=x1(i-1)-(dV-c);

```

```

end;

```

```

%% Find start/end (p/m) points for each RV section

```

```

for j=2:a-1;

    for i=p(j-1):M;if abs(RV(i))<=x1(j);p(j)=i;m(j-1)=i-2;break;end;end;

    %for i=p(j-1):M;if abs(RV(i))<=x1(j-1);p(j)=i;m(j-1)=i-2;break;end;end;%dV=25

end

m(a-1)=bad2-N;

%stay at 0v

p(a)=bad3-N; m(a)=bad4-N;

%p(a)=bad3-N; m(a)=p(a)+dt;%==Case II

%==Case I; (5mins)

%for i=1:b-1; p(a+i)=p(a+i-1)+dt; m(a+i)=m(a+i-1)+dt;end;

%time/voltage history without unwanted ponits, for figure3

RV1=[RV(p(1):m(a-1));RV(p(a):m(a+b-1))];

t1=[t(p(1):m(a-1));t(p(a):m(a+b-1))];

%%%%

end;

%%Frequency Calc. %%%

%for j=1:a-1 %only for 100v 10s 061107 ramp-up case

for j=1:a+b-1

    %for j=1:(a-a1)+b-1

        nnod(j)=nod(m(j))-nod(p(j));

        ts(j)=t(m(j))-t(p(j));

        tavg(j)=t(p(j))+0.5*ts(j);

        f(j)=nnod(j)/ts(j);

        RVs(j)=abs(RV(p(j)));

    end

```

```

%==frequent average of 0v in 5 mins=====

if w==1;

    favg=mean(f(1:b));

    f1=[favg,f(b+1:b+a-1)]; RVs1=RVs(b:b+a-1);%including avg point

    %f1=[favg,f(b+1:b+(a-1)-1)]; RVs1=RVs(b:b+(a-1)-1);%including avg point

    %f1=[f(b+1:b+a-1)]; RVs1=RVs(b+1:b+a-1);%not including avg point

else

    favg=mean(f(a:a+b-1));

    %favg=mean(f((a-1):(a-1)+b-1));

    %favg=mean(f(a:a-1)); %%only for 100v 10s 061107 case

    f1=[f(1:a-1),favg]; RVs1=RVs(1:a);%including avg point

    %f1=[f(1:(a-1)-1),favg]; RVs1=RVs(1:(a-1));%including avg point

    %f1=[f(1:a-1)]; RVs1=RVs(1:a-1);%not including avg point

end

figure(2),[AX,H1,H2] = plotyy(t1,RV1,tavg,f,'plot');grid on;

set(get(AX(1),'Ylabel'),'String','Retarding Potential (v)');

set(get(AX(2),'Ylabel'),'String','Frequency');

xlabel('Time/Average Time (s)');set(H1,'LineStyle','-');set(H2,'LineStyle','*');

if w==1;title('Retarding Potential/Frequency vs. Time - Ramping down');

else title('Retarding Potential/Frequency vs. Time - Ramping up'); end;

%%Moving Average and Polynomial Cruve fit%%
%%pre-processing: normalizing date.

%%Normalization is a process of scaling the numbers in a data set to

%%improve the accuracy of the subsequent numeric computations.

%%A way to normalize cdate is to center it at zero mean and scale it to

%%unit standard deviation: sdate = (cdate - mean(cdate))./std(cdate)

```

```

figure(3),subplot(2,1,1); plot(RVs1,f1,'g*'), grid on;
xlabel('Retarding Voltage(abs)'),ylabel('Frequency');
legend('raw experimental data');
if w==1;title('Raw Stopping Potential Data - Cath Off (4/22/2011)');
else; title('Raw Stopping Potential Data - Ramping up'); end;
f11 = reshape(smooth(f1),1,a); %moving average at 5
%ff11 = smooth(f1,0.1,'rloess'); %moving average at 5

p1=polyfit(RVs1,f11,6); %last number: polynomial of degree
ff11=polyval(p1,RVs1);
figure(3),subplot(2,1,2);plot(RVs1,f11,'g*',RVs1,ff11,'r'), grid on;
xlabel('Retarding Voltage(abs)'),ylabel('Frequency');
legend('Moving averaged data','6th polynomial fit');
if w==1;title('Moving Averaged Stopping Potential Data - Cath Off (4/22/2011)');
else; title('Raw Stopping Potential Data - Ramping up'); end;

q=polyder(p1);
y=RVs1;
%df=q(1)*y.^4+q(2)*y.^3+q(3)*y.^2+q(4)*y+q(5); %for polyfit '5';
df=q(1)*y.^5+q(2)*y.^4+q(3)*y.^3+q(4)*y.^2+q(5)*y+q(6); %for polyfit '6';
%df=q(1)*y.^6+q(2)*y.^5+q(3)*y.^4+q(4)*y.^3+q(5)*y.^2+q(6)*y+q(7); %for polyfit '7';
%df=q(1)*y.^7+q(2)*y.^6+q(3)*y.^5+q(4)*y.^4+q(5)*y.^3+q(6)*y.^2+q(7)*y+q(8); %for polyfit '8';
figure(4),%subplot(2,2,4);
plot(RVs1,df,'r');grid on;legend('First derivative to 6th polynomial fit');
xlabel('Retarding Voltage(abs)'),ylabel('df/dV');title('frequency derivative');

%Find out the max slope point;
if w==1;[min_d,vd]=min(df(1:17));V_stop_down = RVs1(vd)

```

```
else;[min_u,vu]=min(df(1:16));V_stop_up = RVs1(vu)
end;
```

C.1 Uncertainties of droplet specific charge measurements

Case	Test	Date		Uncertainty for Specific Charge Measurement					
				Vacc	Uvacc	$[Uvacc/Vacc]^2$	q/m	Uq/m	$[Uq/m/(q/m)]^2$
1	1	9/26/07	Before	-1300	100	0.0059	-0.526	0.040403	0.0059
			After	-1508	100	0.0044	-0.767	0.050877	0.0044
2	1	4/5/11	Before	-1700	150	0.0078	-0.197	0.017399	0.0078
			After	-400	250	0.3906	-13.56	8.474729	0.3906
				-1850	150	0.0066	-0.123	0.009993	0.0066
2	2	4/12/11	Before	-1820	200	0.0121	-0.169	0.01859	0.0121
			After	-500	250	0.25	-9.147	4.5735	0.25
				-2000	200	0.01	-0.131	0.0131	0.01
2	3	5/13/11	Before	-1622	200	0.0152	-0.154	0.018986	0.0152
			After	-450	400	-	-	-	-
				-1900	400	0.0443	-0.131	0.027572	0.0443
3	1	4/22/11	Before	-1723	150	0.0076	-0.135	0.011769	0.0076
			After	-450	300	-	-	-	-
				-2100	100	0.0023	-0.129	0.006187	0.0023
4	1	5/3/11	Before	-1700	150	0.0078	-0.143	0.012629	0.0078
			After	-500	450	-	-	-	-
				-2050	150	0.0054	-0.151	0.011096	0.0054

C.2 Uncertainties of droplet charge measurements

Case	Test	Date		Uncertainty for Charge Measurement								
				G	U_G	$[U_G/G]^2$	R	U_R	$[U_R/R]^2$	$V=V_p/2$	U_V	$[U_V/V]^2$
1	1	9/26/07	Before	945	47.08	0.002482043	1.00E+06	10000	0.0001	0.0968	0.01	0.010672085
			After	945	47.08	0.002482043	1.00E+06	10000	0.0001	0.044	0.0096	0.047603306
2	1	4/5/11	Before	945	47.08	0.002482043	1.00E+06	10000	0.0001	0.1034	0.0147	0.020211269
			After	945	47.08	0.002482043	1.00E+06	10000	0.0001	0.0704	0.0159	0.051009249
				945	47.08	0.002482043	1.00E+06	10000	0.0001	0.0704	0.0159	0.051009249
2	2	4/12/11	Before	945	47.08	0.002482043	1.00E+06	10000	0.0001	0.0638	0.017	0.070999695
			After	945	47.08	0.002482043	1.00E+06	10000	0.0001	0.0528	0.017	0.103664486
				945	47.08	0.002482043	1.00E+06	10000	0.0001	0.0528	0.017	0.103664486
2	3	5/13/11	Before	945	47.08	0.002482043	1.00E+06	10000	0.0001	0.11	0.0126	0.013120661
			After	945	47.08	0.002482043	1.00E+06	10000	0.0001	0.0638	0.0145	0.051652893
				945	47.08	0.002482043	1.00E+06	10000	0.0001	0.0638	0.0145	0.051652893
3	1	4/22/11	Before	945	47.08	0.002482043	1.00E+06	10000	0.0001	0.0946	0.0154	0.026500811
			After	945	47.08	0.002482043	1.00E+06	10000	0.0001	0.0627	0.015	0.057233122
				945	47.08	0.002482043	1.00E+06	10000	0.0001	0.0627	0.015	0.057233122
4	1	5/3/11	Before	945	47.08	0.002482043	1.00E+06	10000	0.0001	0.1078	0.0126	0.013661663
			After	945	47.08	0.002482043	1.00E+06	10000	0.0001	0.0627	0.0142	0.051291052
				945	47.08	0.002482043	1.00E+06	10000	0.0001	0.0627	0.0142	0.051291052

(Continued)

Case	Test	Date		Uncertainty for Charge Measurement (Continued)							
				C	U_C	$[U_C/C]^2$	TOF	$\beta=2*TOF$	U_q	q	$[U_q/q]^2$
1	1	9/26/07	Before	5.12E-11	5.9E-12	0.013254	0.978	1.956	5.22E-15	-4.80E-14	6.26E-56
			After	2.33E-11	5.22E-12	0.050185	0.7724	1.5448	4.1E-15	-1.55E-14	4.03E-57
2	1	4/5/11	Before	5.47E-11	8.26E-12	0.022793	1.6	3.2	9.34E-15	-6.06E-14	3.2E-55
			After	3.72E-11	8.62E-12	0.053591	0.7498	1.4996	6.68E-15	-8.58E-15	3.28E-57
				3.72E-11	8.62E-12	0.053591	1.7	3.4	1.01E-14	-6.16E-14	3.83E-55
2	2	4/12/11	Before	3.38E-11	9.16E-12	0.073582	1.5	3	1E-14	-4.76E-14	2.28E-55
			After	2.79E-11	9.11E-12	0.106247	0.5193	1.0386	5.87E-15	-6.86E-15	1.62E-57
				2.79E-11	9.11E-12	0.106247	1.5	3	9.98E-15	-4.80E-14	2.29E-55
2	3	5/13/11	Before	5.82E-11	7.29E-12	0.015703	1.6	3.2	8.25E-15	-5.20E-14	1.84E-55
			After	3.38E-11	7.86E-12	0.054235	-	-	-	-	-
				3.38E-11	7.86E-12	0.054235	1.6	3.2	8.89E-15	-5.14E-14	2.09E-55
3	1	4/22/11	Before	5.01E-11	8.54E-12	0.029083	1.6	3.2	9.66E-15	-5.86E-14	3.2E-55
			After	3.32E-11	8.11E-12	0.059815	-	-	-	-	-
				3.32E-11	8.11E-12	0.059815	1.6	3.2	9.18E-15	-4.68E-14	1.84E-55
4	1	5/3/11	Before	5.7E-11	7.27E-12	0.016244	1.6	3.2	8.22E-15	-5.85E-14	2.32E-55
			After	3.32E-11	7.7E-12	0.053873	-	-	-	-	-
				3.32E-11	7.7E-12	0.053873	1.6	3.2	8.71E-15	-4.81E-14	1.76E-55
5	1	6/7/11	Before	-	-	-	-	-	-	-	
			After	-	-	-	-	-	-	-	-

C.3 Uncertainties of droplet size measurements

Case	Test	Date		Uncertainty for Droplet Diameter measurement				
				$[Uq/q]^2$	$[Uq/m/(q/m)]^2$	d	Ud	$[Ud/d]^2$
1	1	9/26/07	Before	6.28E-56	0.0059	5.74E-06	1.46956E-07	0.000656
			After	4.04E-57	0.0044	3.54E-06	7.82591E-08	0.000489
2	1	4/5/11	Before	3.21E-55	0.0078	9.30E-06	2.73914E-07	0.000867
			After	3.29E-57	0.3906	1.80E-06	3.74863E-07	0.0434
				3.84E-55	0.0066	9.79E-06	2.65225E-07	0.000733
2	2	4/12/11	Before	2.28E-55	0.0121	8.29E-06	3.04077E-07	0.001344
			After	1.62E-57	0.25	1.40E-06	2.3325E-07	0.027778
				2.29E-55	0.01	8.85E-06	2.9504E-07	0.001111
2	3	5/13/11	Before	1.85E-55	0.0152	8.67E-06	3.56307E-07	0.001689
			After	-	-	-	-	-
				2.1E-55	0.0443	9.11E-06	6.3906E-07	0.004922
3	1	4/22/11	Before	3.21E-55	0.0076	9.45E-06	2.74558E-07	0.000844
			After	-	-	-	-	-
				1.85E-55	0.0023	9.10E-06	1.4552E-07	0.000256
4	1	5/3/11	Before	2.32E-55	0.0078	9.22E-06	2.71547E-07	0.000867
			After	-	-	-	-	-
				1.76E-55	0.0054	8.51E-06	2.08496E-07	0.0006

References Cited

- [1] Therrien, J., Dindar, A., and Smith D., “AFM Studies of Nanoparticle Deposition via Electrospray Ionization”, *Microscopy Research and Technique*, 70, 2007, pp. 530-533.
- [2] Lenggoro, I.W., Okuyama, K., De la Mora, J.F., and Tohge, N., “Preparation of ZnS Nanoparticles by Electrospray Pyrolysis,” *J. Aerosol Sci.*, Vol. 31, No. 1, 2000, pp. 121-136.
- [3] Pfeifer, R. J., and Hendricks, C. D., “Parametric Studies of Electrohydrodynamic Spraying,” *AIAA Journal*, Vol. 6, No. 3, 1968, pp. 496-502.
- [4] Gamero-Castaño, M., and Hruby, V., “Electrospray as a Source of Nanoparticles for Efficient Colloid Thrusters”, *J. of Propulsion and Power*, Vol. 17, No. 5, 2001, pp. 977-987.
- [5] Chen, D., Pui, D.Y.H., and Kaufman, S.L., “Electrospray of Conducting Liquids for Monodisperse Aerosol Generation in the 4nm to 1.8 μm Diameter Range,” *J. Aerosol Sci.*, Vol. 26, No. 6, 1995, pp. 963-977.
- [6] Taylor, G., “Disintegration of Water Drops in an Electric Field,” *Proceedings of the Royal Society of London. Series A, Mathematical and Physical Sciences*, Vol. 280, No. 1382, 1964, pp. 383-397.
- [7] De la Mora, J.F., “The Effect of Charge Emission from Electrified Liquid Cones,” *J. Fluid Mech.*, Vol. 243, 1992, pp. 561-574.

- [8] De la Mora, J.F., and Loscertales, I.G., "The Current Emitted by Highly Conducting Taylor Cones," *J. Fluid Mech.*, Vol. 260, 1994, pp. 155-184.
- [9] De Juan, L., and De la Mora, J.F., "Charge and Size Distributions of Electrospray Drops," *J. of Colloid and Interface Science* 186, 1997, pp. 280-293.
- [10] Tang, K., and Gomez, A., "Monodisperse Electrosprays of Low Electric Conductivity Liquids in the Cone-Jet Mode," *J. of Colloid and Interface Science* 184, 1996, pp. 500-511.
- [11] Doyle, A., Moffett, D.R., and Vonnegut, B., "Behavior of Evaporating Electrically Charged Droplets," *J. of Colloid Science*, Vol. 19, 1964, pp. 136-143.
- [12] Abbas, M.A., and Latham, J., "The Instability of Evaporating Charged Drops," *J. Fluid Mech.*, Vol. 30, Part 4, 1967, pp. 663-670.
- [13] Schweizer, J.W., and Hanson, D.N., "Stability Limit of Charged Drops," *J. of Colloid and Interface Science*, Vol. 35, No. 3, March 1971, pp. 417-423.
- [14] Taflin, D.C., Ward, T.L., and Davis, E.J., "Electrified Droplet Fission and the Rayleigh Limit", *Langmuir*, Vol. 5, 1989, pp. 376-384.
- [15] Gomez, A., and Tang, K., "Charge and Fission of Droplets in Electrostatic Sprays," *Phys. of Fluids*, Vol. 6, No. 1, 1994, pp. 404 – 414.
- [16] Shelton, H., Hendricks, Jr., C. D., and Wuerker, R. F., "Electrostatic Acceleration of Microparticles to Hypervelocities," *J. of Applied Physics*, Vol. 31, No. 7, 1960, pp. 1243-1246.

- [17] Fuerstenau, S.D., and Benner, W.H., "Molecular Weight Determination of Megadalton DNA Electrospray Ions Using Charge Detection Time-of-Flight Mass Spectrometry," *Rapid Communications in Mass Spectrometry*, Vol. 9, 1995, pp. 1528-1538.
- [18] Hendricks, C.D., "Charged Droplet Experiments," *J. of Colloid Science*, Vol. 17, 1962, pp. 249-259.
- [19] Hogan, J.J., and Hendricks, C.D., "Investigation of the Charge-to-Mass Ratio of Electrically Sprayed Liquid Particles," *AIAA Journal*, Vol. 3, No. 2, 1965, pp. 296-301.
- [20] Keaton, P. W. *et al.*, "A Hypervelocity – Microparticle – Impacts Laboratory with 100-km/s Projectiles," *International Journal of Impact Engineering*, Vol. 10, 1990, pp. 295-308.
- [21] Blandino, J., Shi, X., Rosenblad, N., Flaherty, W., Gamero-Castaño, M., "Charge Detection Mass Spectrometer with Integrated Retarding Potential Analyzer for Study of Colloid Thruster Plumes", *AIAA-2007-5296*, 43rd AIAA/ASME/SAE/ASEE Joint Propulsion Conference & Exhibit, Cincinnati, OH, July 8-11, 2007
- [22] Gamero-Castaño, M. and Hruby, V., "Electric Measurements of Charged Sprays Emitted by Cone-Jets", *J. Fluid Mech.*, Vol. 459, 2002, pp. 245-276.
- [23] Gamero-Castaño, M., "Induction Charge Detector with Multiple Sensing Stages", *Review of Scientific Instruments* 78, 2007, 043301.

- [24] Kemp, R.F. and Sellen, J.M., “Plasma Potential Measurements by Electron Emissive Probes”, *The Review of Scientific Instruments*, 1966, Vol. 37, No. 4, pp. 455-461.
- [25] Smith, L.P., Thermionic Emission, McGraw-Hill Handbook of Physics, 1958, Chapter 6.
- [26] Lieberman M.A. and Lichtenberg A.J., “Principles of Plasma Discharges and Materials Processing”, 1994.
- [27] Hershkowitz N., “Plasmas Diagnostic”, *Discharge Parameters and Chemistry*, Vol. 1, Chapter 3, 1989, pp. 113-183.
- [28] Allen J. E., “Probe theory – The Orbital Motion Approach”, *Physica Scripta*, Vol. 45, 1992, pp 497-503
- [29] Shukla P K and Mamun A A, “Introduction to Dusty Plasma Physics”, 2002.
- [30] Rosenblad N., Independent Study Report, Prepared for Prof. Blandino, “Telemetry Control and Capture (T.C.A.C.)”, 2007.
- [31] Weinheimer, A. J., “The Charge Induced on a Conducting Cylinder by a Point Charge and Its Application to the Measurement of Charge on Precipitation,” *J. of Atmospheric and Oceanic Technology*, Vol. 5, 1988, pp. 298-304.
- [32] Rosenblad N., Independent Study Report, Prepared for Prof. Blandino, “ISP0106: Instrumentation Design for Analysis of Spacecraft Thruster Plumes”, 2007.
- [33] Material Safety Data Sheet, “MSDS, Covalent Associates, Inc.”
- [34] Material Safety Data Sheet, “MSDS, Sigma-Aldrich”.

- [35] Coleman, H.W., and Glenn Steele, W., “Experimentation and Uncertainty Analysis for Engineers”, 2nd edition, 1999.
- [36] Eikens, D.I., and Carr, P.W., “Application of the Equation of Error Propagation to Obtaining Nonstochastic Estimates for the Reproducibility of Chromatographic Peak Moments”, *Anal. Chem.*, 1989, 61, Page 1058-1062.

Bibliography

Electrospray

Taylor, G., "Disintegration of Water Drops in an Electric Field," *Proceedings of the Royal Society of London. Series A, Mathematical and Physical Sciences*, Vol. 280, No. 1382, 1964, pp. 383-397.

De la Mora, J.F., "The Effect of Charge Emission from Electrified Liquid Cones," *J. Fluid Mech.*, Vol. 243, 1992, pp. 561-574.

Inculet I., and Adamiak K., "Charge Limits in Corona Charging of Distorted Liquid Droplets," *IEEE Transactions on Industry Applications*, Vol. 29, No. 6, 1993, pp. 1058-1061.

Inculet, I.I., and Adamiak, K., "Charge Limits in Corona Charging of Distorted Liquid Droplets," *IEEE Transactions on Industry Applications*, Vol. 29, No. 6, 1993, pp. 1058-1061.

De la Mora, J.F., and Loscertales, I.G., "The Current Emitted by Highly Conducting Taylor Cones," *J. Fluid Mech.*, Vol. 260, 1994, pp. 155-184.

Tang, K., and Gomez, A., "On the Structure of an Electrostatic Spray of Monodisperse Droplets," *Physics of Fluids*, Vol. 6, No. 7, 1994, pp. 2317-2332.

Chen, D., Pui, D.Y.H., and Kaufman, S.L., "Electrospray of Conducting Liquids for Monodisperse Aerosol Generation in the 4nm to 1.8 μm Diameter Range," *J. Aerosol Sci.*, Vol. 26, No. 6, 1995, pp. 963-977.

Tang, K., and Gomez, A., “Monodisperse Electrospays of Low Electric Conductivity Liquids in the Cone-Jet Mode,” *J. of Colloid and Interface Science* 184, 1996, pp. 500-511.

De Juan, L., and De la Mora, J.F., “Charge and Size Distributions of Electrospay Drops,” *J. of Colloid and Interface Science* 186, 1997, pp. 280-293.

Orme, M., Courter, J., Liu, Q., Huang, C., and Smith, R., “Electrostatic Charging and Deflection of Nonconventional Droplet Streams Formed from Capillary Stream Breakup,” *Physics of Fluids*, Vol. 12, No. 9, 2000, pp. 2224-2235.

Gamero-Castaño, M., “Electric-Field-Induced Ion Evaporation from Dielectric Liquid”, *Physical Review Letters*, Vol. 89, No. 14, 2002, 147602.

Thermionic Emission

Jones, H. A., “A Temperature Scale for Tungsten”, *Physical Review*, 1926, Vol. 28, No. pp. 202-207.

Smith, L.P., Thermionic Emission, McGraw-Hill Handbook of Physics, 1958, Chapter 6.

Kemp, R.F. and Sellen, J.M., “Plasma Potential Measurements by Electron Emissive Probes”, *The Review of Scientific Instruments*, 1966, Vol. 37, No. 4, pp. 455-461.

Droplet Fission

Doyle, A., Moffett, D.R., and Vonnegut, B., "Behavior of Evaporating Electrically Charged Droplets," *J. of Colloid Science*, Vol. 19, 1964, pp. 136-143.

Abbas, M.A., and Latham, J., "The Instability of Evaporating Charged Drops," *J. Fluid Mech.*, Vol. 30, Part 4, 1967, pp. 663-670.

Schweizer, J.W., and Hanson, D.N., "Stability Limit of Charged Drops," *J. of Colloid and Interface Science*, Vol. 35, No. 3, March 1971, pp. 417-423.

Taflin, D.C., Ward, T.L., and Davis, E.J., "Electrified Droplet Fission and the Rayleigh Limit", *Langmuir*, Vol. 5, 1989, pp. 376-384.

Gomez, A., and Tang, K., "Charge and Fission of Droplets in Electrostatic Sprays," *Phys. of Fluids*, Vol. 6, No. 1, 1994, pp. 404 – 414.

Labowsky, M., Fenn, J.B., and De la Mora, J.F., "A continuum Model for Ion Evaporation from a Drop: Effect of Curvature and Charge on Ion Solvation Energy," *Analytica Chimica Acta 406*, 2000, pp. 105-118.

Inductive Charge Detectors

Shelton, H., Hendricks, Jr., C. D., and Wuerker, R. F., "Electrostatic Acceleration of Microparticles to Hypervelocities," *J. of Applied Physics*, Vol. 31, No. 7, 1960, pp. 1243-1246.

Hendricks, C.D., "Charged Droplet Experiments," *J. of Colloid Science*, Vol. 17, 1962, pp. 249-259.

Hogan, J.J., and Hendricks, C.D., "Investigation of the Charge-to-Mass Ratio of Electrically Sprayed Liquid Particles," *AIAA Journal*, Vol. 3, No. 2, 1965, pp. 296-301.

Pfeifer, R. J., and Hendricks, C. D., "Parametric Studies of Electrohydrodynamic Spraying," *AIAA Journal*, Vol. 6, No. 3, 1968, pp. 496-502.

Weinheimer, A. J., "The Charge Induced on a Conducting Cylinder by a Point Charge and Its Application to the Measurement of Charge on Precipitation," *J. of Atmospheric and Oceanic Technology*, Vol. 5, 1988, pp. 298-304.

Keaton, P. W. *et al.*, "A Hypervelocity – Microparticle – Impacts Laboratory with 100-km/s Projectiles," *International Journal of Impact Engineering*, Vol. 10, 1990, pp. 295-308.

Fuerstenau, S.D., and Benner, W.H., "Molecular Weight Determination of Megadalton DNA Electrospray Ions Using Charge Detection Time-of-Flight Mass Spectrometry," *Rapid Communications in Mass Spectrometry*, Vol. 9, 1995, pp. 1528-1538.

Gamero-Castaño, M. and Hruby, V., "Electric Measurements of Charged Sprays Emitted by Cone-Jets", *J. Fluid Mech.*, Vol. 459, 2002, pp. 245-276.

Gamero-Castaño, M., "Induction Charge Detector with Multiple Sensing Stages", *Review of Scientific Instruments* 78, 2007, 043301.

Electrospray Applications

Okuda, H., and Kelly, A.J., “Electrostatic Atomization – Experiment, Theory and Industrial Applications,” *Physics of Plasmas*, Vol. 3, No. 5, 1996, pp. 2191-2196.

Lenggoro, I.W., Okuyama, K., De la Mora, J.F., and Tohge, N., “Preparation of ZnS Nanoparticles by Electrospray Pyrolysis,” *J. Aerosol Sci.*, Vol. 31, No. 1, 2000, pp. 121-136.

Gamero-Castaño, M., and Hruby, V., “Electrospray as a Source of Nanoparticles for Efficient Colloid Thrusters”, *J. of Propulsion and Power*, Vol. 17, No. 5, 2001, pp. 977-987.

Therrien, J., Dindar, A., and Smith D., “AFM Studies of Nanoparticle Deposition via Electrospray Ionization”, *Microscopy Research and Technique*, 70, 2007, pp. 530-533.

Instrument Design and Documentation

Rosenblad N., Independent Study Report, Prepared for Prof. Blandino, “ISP0106: Instrumentation Design for Analysis of Spacecraft Thruster Plumes”, 2007

Rosenblad N., Independent Study Report, Prepared for Prof. Blandino, “Telemetry Control and Capture (T.C.A.C.)”, 2007

Droplet Charging

Hershkowitz N., “Plasms Diagnoststic”, *Discharge Parameters and Chemistry*, Vol. 1, Chapter 3, 1989, pp. 113-183.

Allen J. E., “Probe theory – The Orbital Motion Approach”, *Physica Scripta*, Vol. 45, 1992, pp 497-503

Shukla P K and Mamun A A, “Introduction to Dusty Plasma Physics”, 2002

Lieberman M.A. and Lichtenberg A.J., “Principles of Plasma Discharges and Materials Processing”, 1994

Uncertainty Analysis

Coleman, H.W., and Glenn Steele, W., “Experimentation and Uncertainty Analysis for Engineers”, 2nd edition, 1999.

Eikens, D.I., and Carr, P.W., “Application of the Equation of Erro Propagation to Obtaining Nonstochastic Estimates for the Reproducibility of Chromatographic Peak Moments”, *Anal. Chem*, 1989, 61, Page 1058-1062.